Reynolds number effects on the aerodynamics of compact axial compressors

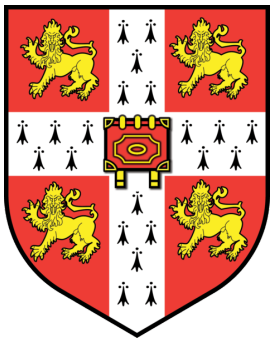

Konstantinos Pantelidis

Whittle Laboratory
Department of Engineering
University of Cambridge

This dissertation is submitted for the degree of *Doctor of Philosophy*

Trinity College July 2018

Declaration

The work presented in this dissertation was conducted at the Whittle Laboratory, Cambridge University Engineering Department, between October 2013 and September 2017. I hereby declare that except where specific reference is made to the work of others, the contents of this dissertation are original and have not been submitted in whole or in part for consideration for any other degree or qualification in this, or any other university. This dissertation is my own work and contains nothing which is the outcome of work done in collaboration with others, except as specified in the text and Acknowledgements. This dissertation contains fewer than 65,000 words including appendices, bibliography, footnotes, tables and equations and has fewer than 150 figures.

Konstantinos Pantelidis

July 2018

Acknowledgements

I would like to express my deep gratitude to Dr. Cesare A. Hall, who supervised and supported the work associated with this dissertation.

The support from the technical staff at the Whittle Laboratory, in particular from Stefan Waterson and John Saunders, during the build of the rig, was of invaluable help.

I would also like to thank Dyson Ltd. for funding the project and their technical support. I am in particular thankful for the support by Dr. Mark Johnson from the high speed research group.

For the long and always very enlightening discussions, not only at work, I would like to thank my fellow colleagues Dr. Andrea Maffioli, Dr. Fiona Hughes, Dr. Kiran Auchoybur, Dr James Taylor, Dr Svilen Savov, Dr. Nishad Sohoni, Dr Tashiv Ramsander and many others with whom I build up close friendships over the years.

Abstract

An axial compressor for a domestic appliance can be designed to be smaller than an equivalent centrifugal compressor. However, the performance of such a compact axial compression system is limited by increased viscous losses and reduced flow turning at low Reynolds numbers (Re).

In domestic appliance compressors, Re is typically in the range 10^4 - 10^5. Although the aerodynamics of isolated aerofoils operating at these Re have been studied extensively, the flow fields within low Re axial compressors have not been investigated in detail. This dissertation aims to develop an improved understanding of loss variation at low Re and to explore how the losses can be reduced through design changes.

Experiments on a 5 times scaled-up single stage axial compressor have been conducted across a range of Re of 10^4 - 10^5. The flow field has been characterised using detailed area traverses with a miniaturised five-hole probe at the rotor inlet, rotor exit and stator exit and a miniature hot-wire at the rotor exit. The probe was specifically designed and calibrated for the scale of the experiments and methods to improve the accuracy of the measurements have been applied including a probe geometry correction. The traverse experiments were performed at the design operating condition ($\phi = 0.55$ and $Re = 6 \times 10^4$) and at a condition close to stall for a datum stage design, a stage with an improved stator design and two stators with compound lean.

It was found that losses in the rotor were greater than the stator losses across the whole range of Re. As expected, the loss decreased with increasing Re for both the stator and rotor. The losses were also increased by three-dimensional flow, with typical loss coefficients at the hub and tip of the blade rows in the range of $20 - 30\%$.

A major contributor to the rotor loss was an unexpected hub separation that increased in size as Re was reduced. At higher Re, the major loss sources were the rotor tip leakage, the stator wake and the stator hub separation. The results indicate that an improved stator design that accounts for the actual, measured, rotor exit flow field at low Re could reduce the Re at which blade row losses start to rise dramatically as well as reduce the loss across all Re.

The improved stator design was better matched to the radial distribution of rotor exit flow angle, which led to a decrease in stator loss across all Re. For all stator designs, however, the measured stage stall margin was identical at all Re. This, along with the increase in velocity deficit in the rotor tip region at off-design indicates that stall occurred in the rotor and was neither Re nor stator design dependent.

The introduction of compound lean to the the stator design had the expected result of decreasing the endwall corner separation loss and increasing midspan losses. The experiments have shown that there was a loss increase in both the midspan and casing region much greater than the corresponding decrease in the stator hub. Also the mass flow redistribution in the experiments was larger that the redistribution predicted by the CFD.

Three-dimensional RANS computations at low Re of the same designs as experimentally studied were also conducted in order to investigate the predictive accuracy of industry standard CFD. The simulation results predicted the overall loss distribution but overestimated the end-wall losses and failed to capture the drop in stage performance at low Re. The differences with the experiments were caused by the inherent limitations of a fully turbulent solver that cannot reproduce transitional flow-features. Similarly to the experiments, there was no stall margin dependency on Re in the simulations.

This thesis has shown that with axial compressors designed specifically for low Re, the Re at which the losses start increasing exponentially can be shifted from 10×10^4 to 4×10^4. The loss increase is predominantly caused by the rotor hub corner separation.

Contents

Nomenclature **xiii**

List of Figures **xvii**

1 Introduction **1**

1.1 Background and motivation 1

1.2 What is known so far 2

1.3 Specific speed 3

1.4 Objectives 4

1.5 Overview of the thesis 5

2 Literature Review **7**

2.1 Low Reynolds number flow features 8

2.1.1 Loss mechanism 8

2.1.2 Aerofoil design 10

2.1.3 Low Reynolds number 2D flow control 11

2.1.4 Low Reynolds 3D losses 15

2.2 High Reynolds number flow 16

2.2.1 Tip leakage flow 16

2.2.2 End-wall flow 19

2.2.3 3D design 22

2.3 Summary 25

3 Methods **27**
3.1 Rig and stage designing 27
3.1.1 Rotor and stator assembly 32
3.1.2 Rotor finite element analysis (FEA) 34
3.1.3 Inlet 34
3.1.4 Instrumentation 37
3.1.5 Traverse 37
3.2 Experimental procedure 39
3.2.1 5-hole probe traverses 40
3.2.2 Hot-wire traverses 44
3.2.3 Error analysis 47
3.3 Computational methods 48
3.3.1 Computational solver set-up 48
3.3.2 Computational investigation parameters 50
3.3.3 Convergence 51
3.4 Post-processing 52
3.5 Summary 53

4 Low Reynolds Number Axial Compressor Flow Field **55**
4.1 Comparison to design intent 55
4.2 Rotor flow features 59
4.3 Rotor and stator loss breakdown 62
4.3.1 Rotor loss analysis 62
4.3.2 Stator loss analysis 64
4.4 Rotor post stall performance 65
4.5 CFD capabilities and limitations 68
4.6 Summary 70

5 Reynolds Number Effects on Axial Compressor Flow Field **71**
5.1 Rotor and stator flow features 71
5.1.1 Rotor flow features 73
5.2 Rotor and stator loss breakdown 74
5.2.1 Rotor loss analysis 75

5.2.2 Stator loss analysis 77
5.3 Loss across Reynolds number 78
5.4 Rotor post stall performance 80
5.5 CFD limitations 82
5.6 Summary 84

6 Effect of Design Changes on Stator Flow Field 85
6.1 Leading edge re-cambering 85
6.1.1 CFD study of stator designs 87
6.1.2 Experimental study of stator design 92
6.2 The effect of compound lean 97
6.2.1 Compound lean parametric studies using CFD 99
6.2.2 Stator compound lean effect on experimental performance . . 104
6.3 Summary 110

7 Conclusions 113
7.1 Major findings 113
7.1.1 Low Reynolds number axial compressor flow field 113
7.1.2 Reynolds number effects 114
7.1.3 Effect of design changes on performance 114
7.1.4 CFD capabilities and limitations 115
7.2 Recommendations for future work 115
7.2.1 Rotor pitch to chord ratio 116
7.2.2 Rotor compound lean 116
7.2.3 Rotor exit endwall velocity triangle design 116
7.2.4 Blade suction side surface treatment 117
7.2.5 Tip gap investigation 117

Bibliography 121

Appendix A Simplified factor of safety calculation 127

Appendix B Loss breakdown calculation 128

Nomenclature

Roman Symbols

$\dot{m}$	Mass flow rate
A	Cross sectional area
c	Axial chord
c_t	True chord
C_L	Lift coefficient
C_{P_o}	Stagnation pressure coefficient
C_P	Static pressure coefficient
c_p	Specific heat capacity
h	Span
N_s	Specific speed
P	Static pressure
P_0	Stagnation pressure
R	Specific gas constant
Re	Reynolds number based on true chord
s	Specific entropy

T	Static temperature
T_0	Stagnation temperature
U	Blade velocity
V	Flow velocity
W	Relative velocity
w	Mass flow weight
y^+	Wall distance
Y_p	Pressure loss coefficient

Greek Symbols

α	Absolute flow angle
β	Relative flow angle
χ	Blade angle
δ	Deviation angle
η	Efficiency
ι	Incidence angle
ν	Kinematic viscosity
ω	Rotational speed
ϕ	Flow coefficient
ψ	Stage loading coefficient
ρ	Density
σ	Solidity $\frac{c_t}{h}$

Abbreviations

APG	Adverse pressure gradient
BL	Boundary layer
CAD	Computer assisted design
CFD	Computational fluid dynamics
FEA	Finite element analysis
HTR	Hub to tip ratio
LE	Leading edge
LSB	Laminar separation bubble
PS	Pressure side
SS	Suction side
TE	Trailing edge

Subscripts

$1, 2, 3$	Rotor inlet, rotor exit/ stator inlet, stator outlet
θ	Tangential
c	Casing
cn	Centre
D	Design
d	Duct
dn	Down
h	Hub
lf	Left
m	Midspan

NS	Near Stall
PC	Partially converged
r	Rotor
rt	Right
s	Stator
stg	Stage
up	Up

List of Figures

1.1 Two different compressor styles used in air handling devices, Dyson Ltd [14] 1
1.2 Effect of Re on aerodynamic loss for a 2D aerofoil 3
1.3 Cordier diagram showing empirical relationship between specific speed (N_s) and specific diameter (D_s) for pumps and fans, Lewis [28] 4

2.1 Section view of a two-dimensional short laminar separation bubble, not to scale, Roberts [38] 8
2.2 Stream-wise velocity profiles over the upper surface of a generic airfoil with varying Reynolds numbers, at a fixed angle of attack of 4°, Shyy et al. [41] 9
2.3 Stream-wise pressure profiles of a generic airfoil, Shyy et al. [41] . . . 10
2.4 Pressure rise coefficient distribution across a $C4$ blade and a front thickened shape-class designed cross section with parabolic leading edge, Maffioli et al. [30] 11
2.5 Traditional aerofoil experimental pressure distribution at a range of Re , incidence at -4° and 20° camber, Rhoden [36] 12
2.6 Shape-class aerofoil MISES pressure distribution at $Re = 3.5 \times 10^4$, incidence at -3° and 20° camber, from internal report 13
2.7 Shape-class aerofoil MISES pressure distribution at $Re = 9 \times 10^4$, incidence at -3° and 20° camber, from internal report 13
2.8 Performance comparison between conventional and reversed (sharp LE) for a range of Re cases, Roberts [37] 14

2.9 Schematic of surface pressure distribution with enlargement of spike, Goodhand and Miller [21] 14
2.10 Influence of the turbulence level on the flow loss of a compressor cascade, Roberts [37] 15
2.11 Total tip loss development showing different contributions, Bindon [2] 17
2.12 Flow over the tip gap of a thin unshrouded blade, Denton [9] 17
2.13 Influence of clearance gap ($\%$ of chord) on calculated total pressure loss, Gbadebo et al. [19] 18
2.14 Vortex core breakdown leading to recirculation when decreasing flow coefficient from 0.38 (left) to 0.37 (right), Furukawa et al. [15] 19
2.15 Time-dependent development of blade tip vortex, Mailach et al. [31] . 20
2.16 Stator end-wall separation 20
2.17 The effect of small geometry changes on hub loss, Goodhand and Miller [22] 21
2.18 End-wall surface height contours, for the optimised end-wall, Reutter et al. [35] 21
2.19 Definitions of sweep and lean, Denton and Xu [10] 23
2.20 Comparison of measured 2D and 3D blade row exit conditions at a near-stall operating point, Gallimore et al. [16] 24

3.1 Rotor and Stator blade sections of the test compressor stage 31
3.2 Pressure loss and deviation angle variation with incidence angle for a front loaded low Re section, Maffioli et al. [30] 32
3.3 Rotor and stator CAD designs 33
3.4 Rotor FEA boundary conditions (left) and mesh (right) applied to AL7075 35
3.5 Rotor FEA analysis 36
3.6 Experimental rig set-up 36
3.7 Slider used for radial traverse 38
3.8 Rotary table used for circumferential traverse 38
3.9 Rig schematic (not to scale) showing traverse locations 39
3.10 Measured static pressure rise characteristic at Re_D, showing ϕ_D and ϕ_{NS} 41
3.11 Traversing of a five-hole probe in a gradient field, Hoenen et al. [27] . 42
3.12 Probe hole allocation 42

3.13 5-hole Probe calibration map at a speed of $30\ \mathrm{m/s}$ 43
3.14 Rotor exit and stator exit traverse mesh 44
3.15 Hot-wire raw (left) and ensemble averaged (right) midspan meridional velocity across 2 pitches 45
3.16 Hot-wire calibration curve 46
3.17 Hot-wire response curve to yaw angle 46
3.18 Hot-wire probe support with 9 yaw angle locations 47
3.19 DSA3217 measured pressure versus FCO332 measured pressure . . . 48
3.20 CFD domain 49
3.21 Blade-to-blade mesh at midspan 49
3.22 Rotor blade surface and tip gap mesh 50
3.23 Convergence plots of a converged simulation 52

4.1 Spanwise, pitch-averaged, distribution of non-dimensional axial velocity, angular momentum and static pressure at Re_D and ϕ_D 56
4.2 Measured spanwise incidence and deviation distributions for the rotor and stator at $Design$ (D) and $Near\ Stall$ (NS) for Re_D 57
4.3 Measured total to total efficiency characteristic at Re_D 59
4.4 Computed, steady RANS, $\frac{V}{V_x}$ streamlines for the rotor tip leakage vortex, Re_D 60
4.5 Absolute flow angle contours at the rotor exit at $Design$ and $Near\ Stall$ (hot-wire) 61
4.6 Non-dimensionalised meridional velocity contours at the rotor exit at $Design$ and $Near\ Stall$ (hot-wire) 61
4.7 Design Re stage loss breakdown at $Design$ and $Near\ Stall$ flow coefficients 62
4.8 Rotor stagnation pressure loss distribution at Re_D for ϕ_D, ϕ_{NS} and from Maffioli et al. [30] 63
4.9 Measured stagnation pressure deficit across the stator at Re_D at $Design$ and $Near\ Stall$ 65
4.10 Flow angle and velocity contours at the rotor exit at $Post\ Stall$ (hot-wire) 65

4.11 Spanwise distribution of non-dimensionalised meridional velocity and deviation at the rotor exit for $Design$, $Near\ Stall$ and $Post\ Stall$ (hot-wire) 66
4.12 Pitchwise meridional velocity at rotor exit, hub region (hot-wire) . . . 67
4.13 Pitchwise meridional velocity at rotor exit, midspan region (hot-wire) 67
4.14 Spanwise, pitch-averaged, distribution of non-dimensional axial velocity, angular momentum and static pressure at Re_D and ϕ_D 68
4.15 Computed rotor exit non-dimensional meridional velocity at Re_D . . 69
4.16 Computed stator exit stagnation pressure at Re_D 69

5.1 Measured spanwise distribution of incidence and deviation at ϕ_D . . . 72
5.2 Hot-wire absolute flow angle measurements at rotor exit (hot-wire) . . 73
5.3 Hot-wire meridional velocity measurements at rotor exit (hot-wire) . . 74
5.4 Stage loss breakdown across Re 75
5.5 Spanwise meridional velocity at the rotor exit (hot-wire) 76
5.6 Pitchwise meridional velocity at the rotor exit (hot-wire) 76
5.7 Pitchwise meridional velocity at the rotor exit (hot-wire) 77
5.8 Measured stagnation pressure deficit across the stator at 2 different Re 78
5.9 Measured and computed variation of blade row stagnation pressure loss with Re 79
5.10 Stage loss breakdown across Re 79
5.11 Y_p distribution at ϕ_D for 3 different Re 80
5.12 Contours at the rotor exit at $Re = 2 \times 10^4$ and $Post\ Stall$ (hot-wire) . 81
5.13 Spanwise meridional velocity at the rotor exit (hot-wire) 81
5.14 Pitchwise meridional velocity at the rotor exit (hot-wire) 82
5.15 Measured (solid) and Computed (dashed) spanwise rotor exit axial velocity distribution at ϕ_D for Re_D and $Re = 2 \times 10^4$ 83
5.16 Computed rotor exit non-dimensional meridional velocity at $Re = 2 \times 10^4$ 83

6.1 Stator leading edge re-cambering 86
6.2 Effect of stator design on stage stagnation pressure rise 87
6.3 The effect of stator design on rotor and stage efficiency 88
6.4 The effect of stator design on rotor and stator loss 88

6.5 The effect of stator design on stator incidence and deviation angles at $Design$ and $Near\ Stall$ 89
6.6 The predicted effect of stator leading edge re-cambering design on stator loss 90
6.7 The effect of stator design on stator mid-span surface pressure distribution 91
6.8 CAD section design of the 3D printed stator B 91
6.9 The effect of stator design on measured incidence and deviation . . . 92
6.10 The effect of stator design on stator measured stagnation pressure deficit at $Design$ and $Near\ Stall$ 93
6.11 Stage loss breakdown for stator A and stator B at Re_D 94
6.12 The effect of stator design on stator measured stagnation pressure deficit across a range of Re 95
6.13 The effect of stator design on rotor and stator measured loss across a range of Re 96
6.14 Stage loss breakdown across Re, using stator B 96
6.15 Unintended LE and TE compound lean caused by LER 97
6.16 Stator lean distributions 98
6.17 Lean extent definition 98
6.18 Stator compound lean magnitude effect on rotor and stage efficiency . 100
6.19 Stator compound lean magnitude effect on stator stagnation pressure loss, change from stator B at $Design$ 100
6.20 Stator compound lean spanwise extent effect on rotor and stage efficiency 101
6.21 Stator compound lean spanwise extent effect on stator stagnation pressure loss change from case B at $Design$ 102
6.22 CAD section design of the 3D printed stators, C(left) and D(right) . . 102
6.23 Computed spanwise incidence and deviation distributions for the rotor and stator at Re_D 103
6.24 Computed spanwise, pitch-averaged, distribution of non-dimensional axial velocity, angular momentum and static pressure at $Near\ Stall$ for Re_D 104
6.25 Stagnation pressure loss contours at $Re = 6 \times 10^4$ 105
6.26 Stator loss breakdown for stators B, C and D at $Near\ Stall$ 105

6.27 Measured spanwise incidence and deviation distributions for the rotor and stator at $Near\ Stall$ for Re_D 106
6.28 Spanwise, pitch-averaged, distribution of non-dimensional axial velocity, angular momentum and static pressure at $Near\ Stall$ for Re_D . . 107
6.29 Stagnation pressure loss contours at $Re = 2 \times 10^4$ 108
6.30 Stator loss breakdown for three stators at $Near\ Stall$ for $Re = 2 \times 10^4$ 108
6.31 Measured spanwise incidence and deviation distributions for the rotor and stator at $Near\ Stall$ for $Re = 2 \times 10^4$ 109
6.32 Spanwise, pitch-averaged, distribution of non-dimensional Axial velocity, angular momentum and static pressure at $Re = 2 \times 10^4$ and $Near\ Stall$ 110

7.1 Tip clearance effect on rotor and stator efficiency at $Design$ and $Near\ Stall$ 118
7.2 Tip clearance effect on rotor pressure loss at $Design$ and $Near\ Stall$ 119
7.3 Tip clearance effect on stator incidence and deviation at $Design$ . . . 120
7.4 Tip clearance effect on ϕ range 120

Chapter 1

Introduction

1.1 Background and motivation

Compressor design is being pushed to the limits. More compact and lightweight compressors, that are required by industry, lead to decreasing operating Reynolds numbers. Reynolds numbers in the order of 10^4 typically lead to centrifugal designs. The main challenges behind low Reynolds number axial compressors are: generating high efficiencies when dealing with transitional flow as well as 3D flow structures; and secondly achieving a large operating range.

Dyson axial compressor

Dyson centrifugal compressor

Figure 1.1: Two different compressor styles used in air handling devices, Dyson Ltd [14]

There is an increasing number of applications where low Reynolds numbers are of prime interest. These include and are not limited to:

- Domestic air handling devices, compressors, (e.g. vacuum cleaners, hand dryers, hair dryers)
- Micro air vehicles (MAV), aerofoils, Lian and Shyy [29]
- High altitude unmanned aerial vehicles, compressors and turbines, Weinberg and Wyzykowski [52]

Figure 1.1(left) illustrates the most recent axial compressor currently in use by industry; whereas, figure 1.1(right) illustrates a traditional centrifugal compressor used in industry. The fact that low Reynold number axial compressors are currently being used in industry, advocates for a better understanding of their flow physics.

There is little axial compressor literature in this area of low Reynolds numbers, as discussed in chapter 2, with one of the most relevant publications being by Choi et al. [5]. The main aspect of this piece of research was to establish the effect a Reynolds number decrease, from $Re = 10^5$ to $Re = 10^4$, has on rotor 2D and 3D losses. The main conclusions were an increased end-wall secondary flow loss that covered a significant region of the span and a decreased tip flow loss due to the lower velocity mixing. One of the issues with this research was the fact that the flow solver used was not validated by experiments in the low Reynolds number regime. Also transition was not incorporated in the simulations, therefore the flow effects resulting from that could not be investigated.

1.2 What is known so far

It is known that the 2D losses increase with decreasing Re, see figure 1.2a. The primary cause for these losses is the transition of flow from laminar to turbulent and the subsequent turbulent separation, see figure 1.2b. Maffioli et al. [30] found that a forward loaded and forward maximum thickness blade can decrease the 2D losses.

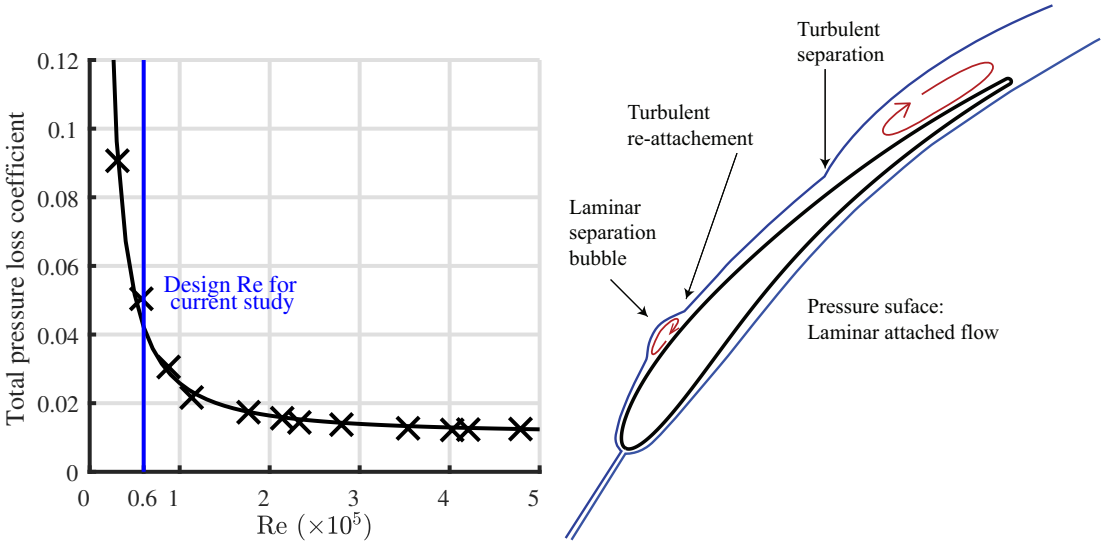

(a) Variation of loss coefficient with Re, from Rhoden [36]

(b) Schematic of low Re aerofoil showing key flow features, Shyy et al. [41]

Figure 1.2: Effect of Re on aerodynamic loss for a 2D aerofoil

1.3 Specific speed

Until recently domestic air handling devices have used centrifugal compressors. The specific speed (N_s), using equation 1.1 with ϕ and ψ values from section 3.1, of the compressor being investigated is 1.5. Figure 1.3 illustrates the recommended type of compressor for a given N_s.

$$Ns = \phi^{\frac{1}{2}}\psi^{-\frac{3}{4}} \tag{1.1}$$

Lewis [28] said "it is in reality a mean experience curve fitted through a scatter plot and only serves as an indication of the suitable machine type to select for a given application". Even though a centrifugal compressor is recommended at this N_s, the border of the axial compressor range lies close to $N_s = 1.5$, hence an axial compressor could be suitable as well. The main benefits of using an axial compressor would be:

- A lower tip radius, thus the device housing the compressor could be decreased in size.

- Fully axial flow would allow the use of the compressor in a variety of devices.
- Higher achievable peak efficiency.

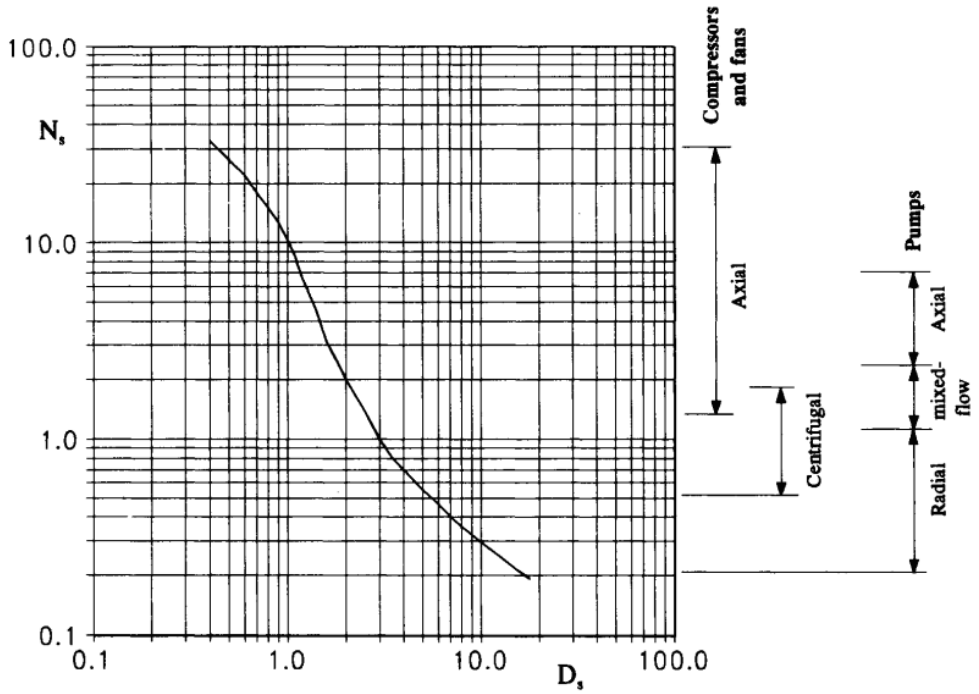

Figure 1.3: Cordier diagram showing empirical relationship between specific speed (N_s) and specific diameter (D_s) for pumps and fans, Lewis [28]

1.4 Objectives

The overall aim of this research is to improve our understanding of Reynolds number dependent flow features within axial compressors. The thesis objectives contributing to this aim are as follows:

1. To establish an experimental method for measuring the 3D flow field within a low Reynolds number axial compressor. (Chapter 3)
2. To understand the flow field of a low Reynolds number axial compressor stage, both at design and near stall operating conditions, and to quantify the loss sources within the stage at these conditions. (Chapter 4)

3. To understand how variations in Reynolds number affect the key flow features and the loss breakdown. (Chapter 5)

4. To explore the impact of 3D design when applied to a low Reynolds number compressor stator. (Chapter 6)

5. To determine the capabilities and limitations of industry standard fully turbulent RANS for the design and analysis of low Reynolds number axial compressor stages. (reviewed in chapters 4 to 6)

1.5 Overview of the thesis

An in depth review in the literature on 2D losses and high Reynolds number compressor 3D losses was undertaken and the main findings are discussed in Chapter 2. It was established that the area of low Re axial compressors has not been fully explored in either the experimental or the computational regime.

The experimental and computational methodology is described in chapter 3. In this chapter the design and manufacture of the experimental rig is discussed, along with the instrumentation used to record and log measurements during the experiments.

With the aid of rotor exit hot-wire traverses and 5-hole probe rotor inlet, rotor exit and stator exit traverses the flow field was investigated. The flow field and the blade row loss breakdown at the design and off-design flow coefficients, across a range of Reynolds numbers is discussed in chapters 4 and 5.

Chapter 6 considers the effect of decreasing the incidence angle at the stator endwall in order to decrease the stator corner separation. Additionally, the chapter explores what compound lean does to the flow of the stator at low Re comparing to what is already known from 3D design literature at high Re.

Finally the main conclusions along with recommendations for future research are summarized in Chapter 7.

Chapter 2

Literature Review

The target of this thesis is to build a better understanding of the flow field in a low Reynolds number axial compressor stage. This chapter aims to discover the gaps in the known literature and explore what is known so far about the flow field high Reynolds number axial compressors. There are two main areas that are investigated.

The first section of this chapter will review the literature on the 2D flow field of low Re aerofoils and cascades along with the losses associated with that flow. Finding out what the instigators for these losses are and various methods that can be used to control these flow features and decrease the losses associated with them.

Secondly, the 3D flow field associated with high Re axial compressors will be reviewed. In addition, the loss mechanisms and the methods used for tackling against them will be identified. It will then be possible to attempt and use some of them to manipulate any low Re flow features, that get identified in the following chapters.

Compressor loss is split into three major categories, Denton [9].

1. 2D loss, profile loss, discussed in section 2.1

2. Tip leakage loss, discussed in section 2.2

3. End-wall loss, discussed in section 2.2

2.1 Low Reynolds number flow features

In this section the 2D flow features that contribute to the loss of an aerofoil or a cascade are investigated along with various attempts at controlling them.

2.1.1 Loss mechanism

At these low Re the effect of flow transition comes into play. A laminar boundary layer (BL) on the rotor suction side (SS) separates, transitions to turbulent and finally reattaches, forming a laminar separation bubble (LSB), see figure 2.1. As discussed in Shyy et al. [41], the laminar flow outside the bubble forms a free-shear layer that encapsulates the bubble. The turbulent flow allows high momentum flow from the free-stream to travel closer to the surface thus allowing the separated flow to reattach. This is an unavoidable side-effect of operating in this low Re regime. The width and thickness of the LSB is increased by an increase in incidence or a decrease of flow speed, Gaster [17].

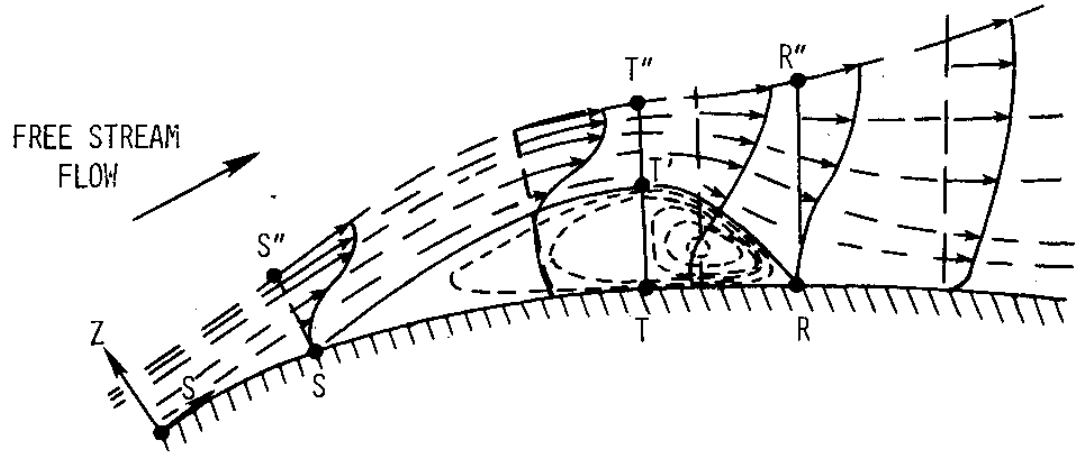

Figure 2.1: Section view of a two-dimensional short laminar separation bubble, not to scale, Roberts [38]

A separation on a velocity or pressure distribution corresponds to a flattened region, as the edge velocity and surface pressure do not change significantly in a separated

region, see figures 2.2 and 2.3. The loss associated with an LSB is split into 3 main areas:

- For large bubbles the effective blade surface changed causing a blockage effect.
- The recirculation within the bubble causes mixing loss.
- The pressure recovery deficit after the bubble increases the momentum thickness, thus increasing loss.

The size and location of this bubble varies with Reynolds number, see figures 2.2. At high Reynolds numbers, $Re = 10^6$, the bubble is very short and relatively close to the leading edge, at 25% chord. As the Reynolds number decreases, 4×10^4, the position of the laminar separation stays fixed and the transition point moves further downstream, at 30% up to 65% chord. When the Reynolds number reaches a certain value, 2×10^4, the bubble extends further than the trailing edge and the flow never reattaches. This bubble incurs greater profile losses in compressors that were not captured by Choi et al. [5]; therefore, experimental validation is of great significance.

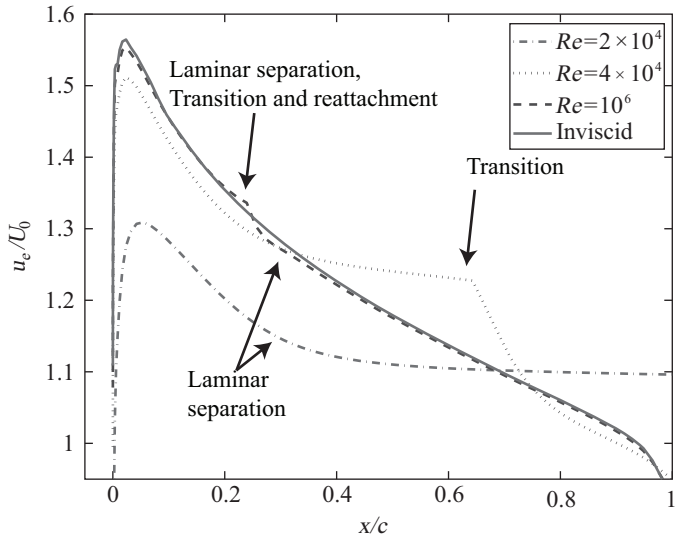

Figure 2.2: Stream-wise velocity profiles over the upper surface of a generic airfoil with varying Reynolds numbers, at a fixed angle of attack of $4°$, Shyy et al. [41]

As the size of the LSB increases the pressure distribution is affected, see figure 2.3. The blade surface pressure remains constant throughout the width of the bubble, this

corresponds to the flat region of the pressure distribution in figure 2.3. At the position of transition and reattachment the pressure starts to rise once again. The pressure deficit due to the separation is not fully recovered after reattachment, thus the overall pressure rise across the chord is decreased, Tani [46].

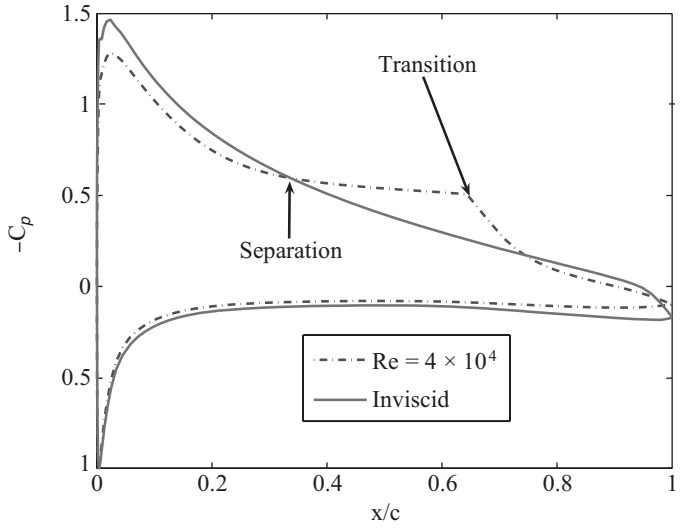

Figure 2.3: Stream-wise pressure profiles of a generic airfoil, Shyy et al. [41]

The loss associated with the LSB is not present in industrial jet engines. Length scales are large, thus $Re > 10^5$. The flow is fully turbulent, therefore the 2D profile losses are low and independent of Re. That is why Maffioli et al. [30] has adapted a different process in blade design optimisation at this low Re regime.

2.1.2 Aerofoil design

A new aerofoil design procedure, using shape-class to define the cross-section, was introduced by Maffioli et al. [30] to account for the presence of the LSB in low Re flow. The thickness distribution was investigated with greater emphasis given on the maximum thickness location. Figure 2.4 shows the pressure distribution of the optimal shape-class distribution with a maximum thickness location of 20%. The pressure gradient is more uniform on the suction side resulting in a "fuller" distribution with an increase of 1.5% in efficiency. The laminar separation occurs earlier in the shape-class design and transitions earlier, due to the front loaded design. This decreases the

loading at the aft part of the blade and prevents the turbulent flow from separating early on, decreasing the deviation and loss. Further more the effect of the incidence angle, turning and other parameters were investigated to optimise for pressure loss, deviation and range.

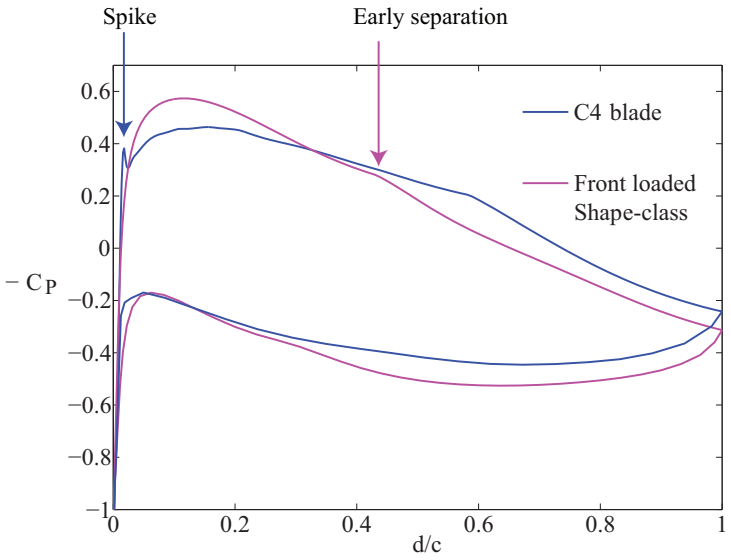

Figure 2.4: Pressure rise coefficient distribution across a $C4$ blade and a front thickened shape-class designed cross section with parabolic leading edge, Maffioli et al. [30]

The effect of Re on the pressure distribution in a cascade was experimentally investigated by Rhoden [36]. The location of the laminar separation was constant across Re, whereas the location of the turbulent transition and reattachment moved further downstream at lower Re, see figure 2.5. At the lowest Re there was no reattachment. MISES was used to investigate two different Re using the optimised shape-class design, see figures 2.6 and 2.7. The major difference is the location of the laminar separation is 20% of the chord earlier thus at even the lowest Re there is turbulent reattachment. Hence, the aerofoil performance is higher.

2.1.3 Low Reynolds number 2D flow control

In the low Re regime several different methods have been investigated into the effect of the laminar flow transition. The size and location of the bubble could be altered to de-

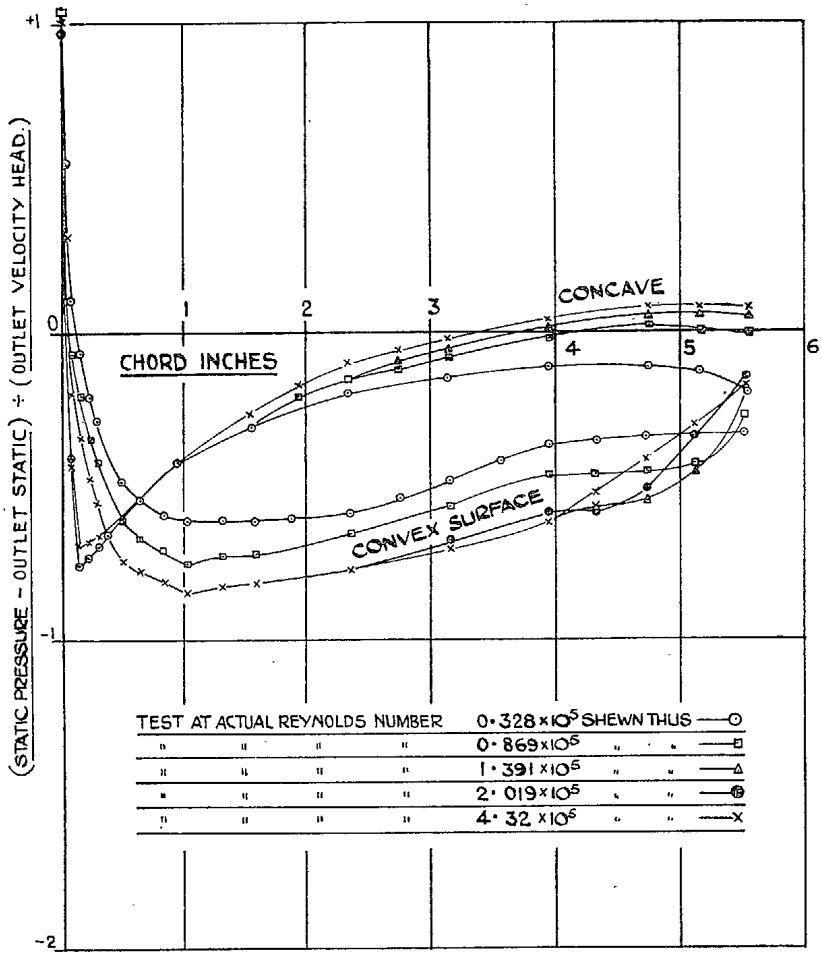

Figure 2.5: Traditional aerofoil experimental pressure distribution at a range of Re , incidence at $-4°$ and $20°$ camber, Rhoden [36]

crease the losses associated by transition. Some research has already been undertaken in aerofoils and cascades on the following features, Roberts [37]:

- Leading edge (LE) profiles.
- Tripwires and roughness elements.
- High free-stream turbulence.
- Maximum blade thickness location.

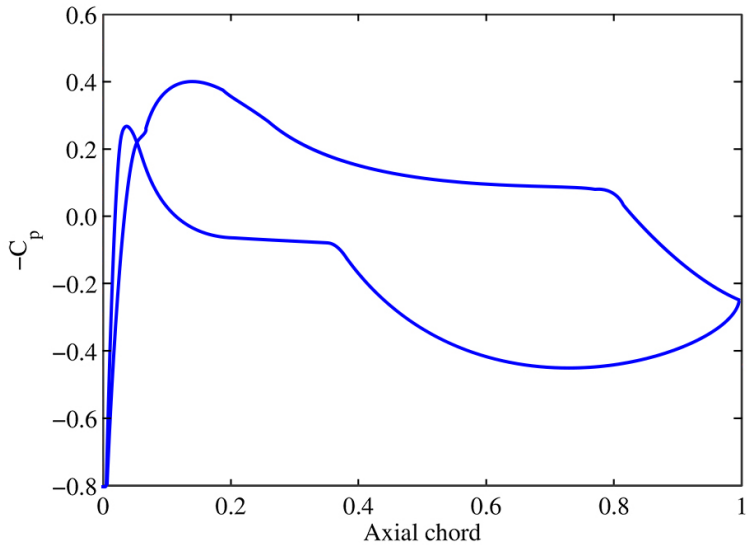

Figure 2.6: Shape-class aerofoil MISES pressure distribution at $Re = 3.5 \times 10^4$, incidence at $-3°$ and $20°$ camber, from internal report

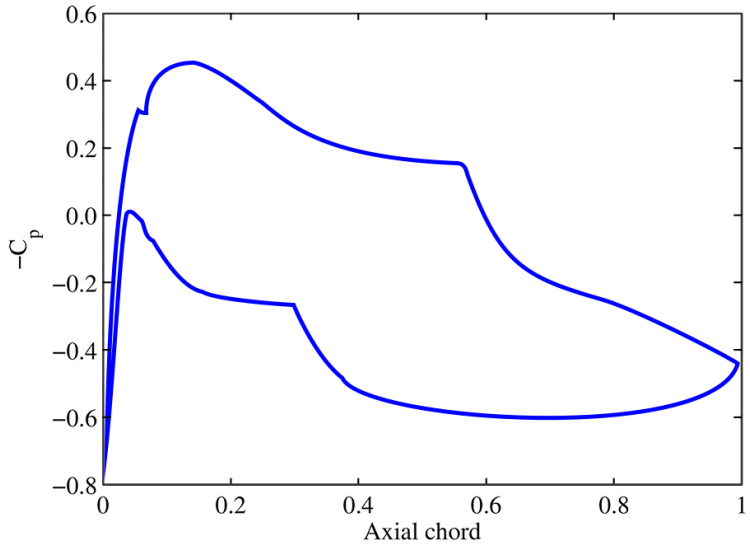

Figure 2.7: Shape-class aerofoil MISES pressure distribution at $Re = 9 \times 10^4$, incidence at $-3°$ and $20°$ camber, from internal report

Different LE shapes have different effects to the flow of a low Re aerofoil. A sharp LE acts as a tripping agent causing the transition to occur early on the SS. For Re less than a critical value the loss of a sharp LE is lower than that of a conventional LE, see figure 2.8. However, there is a trade-off between loss and range. The sharp LE decreases the loss and the range at the same time, Roberts [37]. On the other hand Goodhand and Miller [21] showed at high Re that a parabolic LE could decrease losses associated with pressure spikes, see figure 2.9. The spike caused a premature transition to turbulent flow, which in turn raised profile loss. The spike was more profound in elliptical LEs.

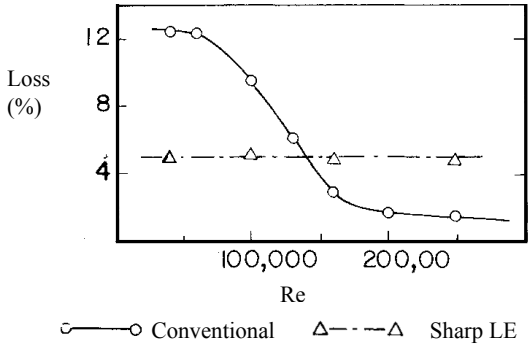

Figure 2.8: Performance comparison between conventional and reversed (sharp LE) for a range of Re cases, Roberts [37]

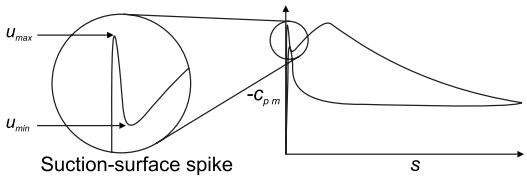

Figure 2.9: Schematic of surface pressure distribution with enlargement of spike, Goodhand and Miller [21]

Since a sharp LE is not recommended due to the low operating range, a tripwire or roughness elements could be used to trip the flow and force transition earlier. Similarly to the sharp LE Roberts [37], managed to increase the performance at Re lower than a critical value. Goodhand and Miller [21] showed that, at high Re, LE surface roughness

increased the loss, especially near the hub, which was expected from Roberts [37]. Therefore, a tripwire or a LE surface roughness could be investigated.

Lian and Shyy [29] and Roberts [37] investigated the effect of free stream turbulence (FST). Both suggest a decrease in loss due to FST. As FST was increased from zero, the transition bubble shrunk and the loss decreased to a maximum of 30%, Roberts [37]. It was also noticed that after a value of 2.5% of FST the loss started increasing reaching the 0% FST loss level, see figure 2.10. At that point the turbulence generator loss increased more rapidly than the transition loss decreased. This means, if generating the turbulence is necessary, there is a limited benefit. On the other hand, actual "air handling devises" have ducts and struts along the path of the inlet flow that create their own free stream turbulence. Hence, if the turbulence level is known, its value could be used during the design process.

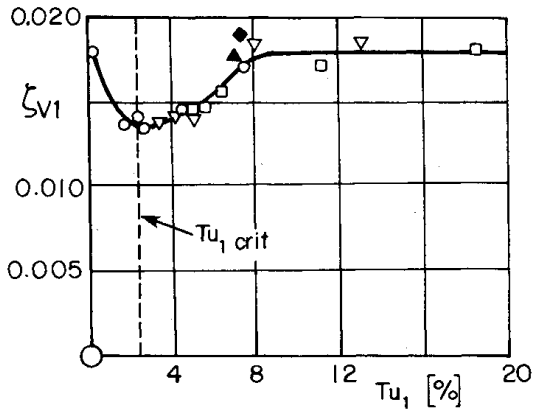

Figure 2.10: Influence of the turbulence level on the flow loss of a compressor cascade, Roberts [37]

Lian and Shyy [29] investigated MAV wings and the effect of transition in their performance. The investigation was missing the effect of 3D flow effects, which would be very beneficial for this research.

Roberts [37] has suggested various methods of increasing the 2D performance of compressors cascades at low Re, it was missing investigation on 3D axial compressor geometries designed explicitly for low Re flows. Even though there is limited relevance with this research both provide methods that can be tried in 3D axial compressors.

2.1.4 Low Reynolds 3D losses

The 3D flow losses in high Re compressors have been much more extensively researched and understood; than losses at Re of the order of 10^4.

Choi et al. [5] used a numerical approach to compare the effect Re, a range of 2×10^4 - 2×10^5, has on the three main flow loss factors. The simulations were on a "rotor only" compressor. Both the profile loss and end-wall loss had increased by 50% and 20%, respectively; whereas the tip flow loss decreased by 30%. The end-wall loss and profile loss increase was caused by the end-wall separation extending to a larger portion of the span. On the other hand, the tip region loss decreased due to a weaker tip-to-core mixing. Also, the pressure rise across the rotor decreased due to the large separation. This research lacked experimental validation at these low Re and a laminar transition model to account for the effect of the transition bubble.

2.2 High Reynolds number flow

A better look at the cause of the losses and methods to decrease them can be obtained from high Re compressor loss literature.

2.2.1 Tip leakage flow

Bindon [2] has shown that blade tip loss can be split into 3 main components, see figure 2.11:

- End-wall loss, assumed equal end-wall gap-less loss
- Internal gap shear loss
- Mixing loss

The internal gap shear loss depends on the type of flow over the tip gap of the blade. The thickness of the blade with respect to the width of the gap is responsible for the type of gap. Figure 2.12, demonstrates the two different types of flow over the tip gap. A compressor blade is thinner than a turbine blade; therefore, the flow demonstrated

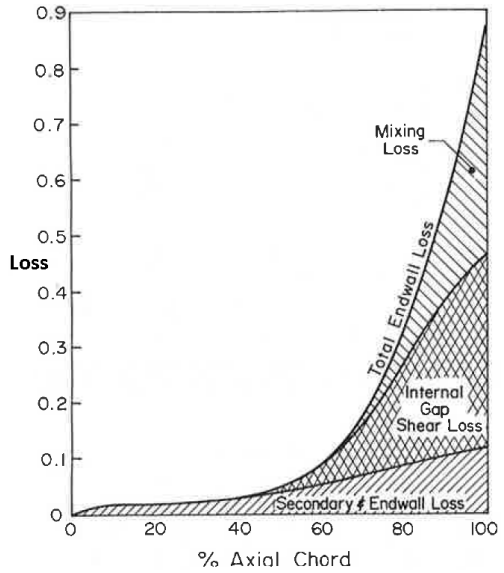

Figure 2.11: Total tip loss development showing different contributions, Bindon [2]

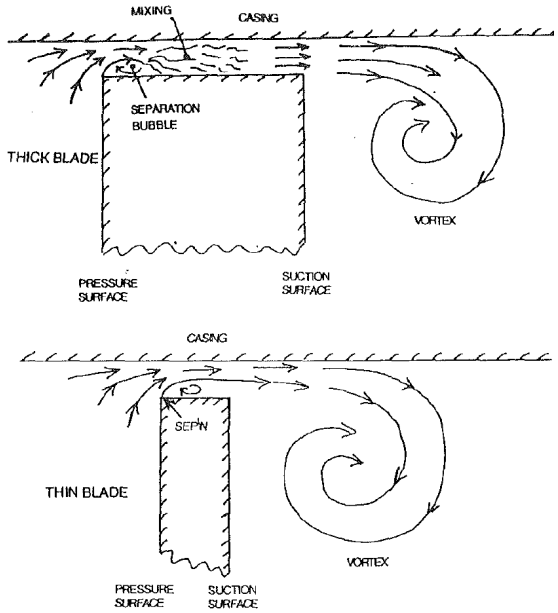

Figure 2.12: Flow over the tip gap of a thin unshrouded blade, Denton [9]

in figure 2.12-lower would be more representative. Since there is no reattachment and mixing within the gap, the internal gap shear loss for a compressor is negligible.

The main contribution to compressor tip leakage loss is therefore due to the flow mixing, created by the tip gap vortex. The vortex is a by-product of the rotor pressure side (PS) flow leaking into the SS. The intense difference in flow direction causes the large shearing, Storer and Cumpsty [44], and the difference between the two flow velocities encourages recirculation, which in turn generate mixing loss, Denton [9]. The vortex can be affected by many factors, which include the width of the tip gap, the flow coefficient, the casing boundary layer thickness and Re, Mailach et al. [31]. The mixing of the flow caused due to the vortex leg is another loss factor in the tip region which was not quantified byBindon [2] .

A study on the tip clearance flow at various gap widths was carried out by Gbadebo et al. [19], see figure 2.13. In the region of $0\% <$ clearance $< 0.24\%$ the loss was at a maximum, this coincided with an increase in the number of saddle singularities, Gbadebo et al. [18]. The saddle points are the points where the streamlines crossed during simulations. At clearance $> 0.24\%$ where the clearance was of the order of the inlet boundary layer displacement thickness and the leakage flow velocity was significantly lower, the loss started to decrease. A minimum was reached at clearance $= 1\%$; when the clearance was more than 2 times the inlet boundary layer displacement thickness the loss started to increase again. A benefit from clearance width management could only be achieved once it is of the order of the inlet boundary layer displacement thickness.

The effect of operating point flow coefficient on tip flow structure was investigated by Furukawa et al. [15]. It was found that there was no significant change in the structure of the vortex "at any flow rate not lower than the peak pressure rise operating condition". Vortex core breakdown occurred within the rotor at a flow coefficient near stall, see figure 2.14. This breakdown caused a recirculation region to form, which in turn increased the tip leakage loss. At even lower flow coefficients the breakdown flow increased in size until it started interacting with the SS boundary layer. The interaction gave rise to a three dimensional blade separation, which differed from the traditional 2D blade separation, Furukawa et al. [15].

Taghavi-Zenou et al. [45] also found that at near stall flow coefficients the vortex structure interacts with the adjacent blade. In addition to that it was noticed that

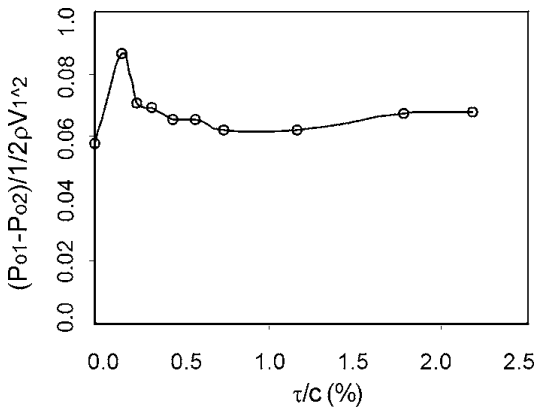

Figure 2.13: Influence of clearance gap (% of chord) on calculated total pressure loss, Gbadebo et al. [19]

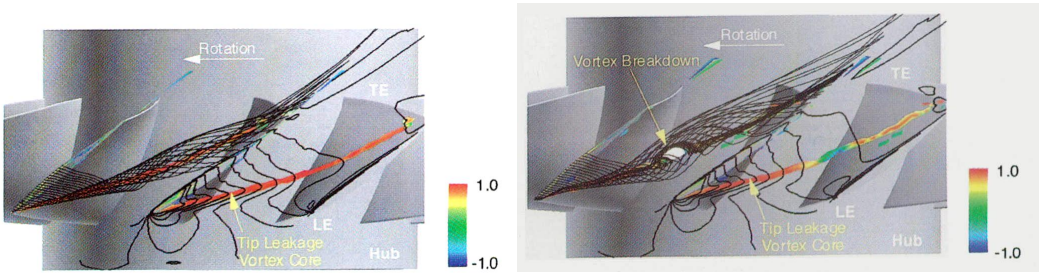

Figure 2.14: Vortex core breakdown leading to recirculation when decreasing flow coefficient from 0.38 (left) to 0.37 (right), Furukawa et al. [15]

the tip leakage vortex frequency changed from close to the blade passing frequency (BPF) to half. The frequency change was also noticed by Mailach et al. [31] where the vortex of one blade interacted with the tip gap of the adjacent one. Figure 2.15 shows the effect of this interaction, the vortex passes through two blade passages. The second passage has a smaller vortex with a higher mean through-flow. These rotating instabilities "can be responsible for the intensification of clearance noise and the excitation of large amplitude blade vibrations", which can be detrimental for a small scale domestic compressor. Therefore unsteady CFD simulations and experimental high frequency pressure readings would be encouraged to attempt and capture these rotating instabilities.

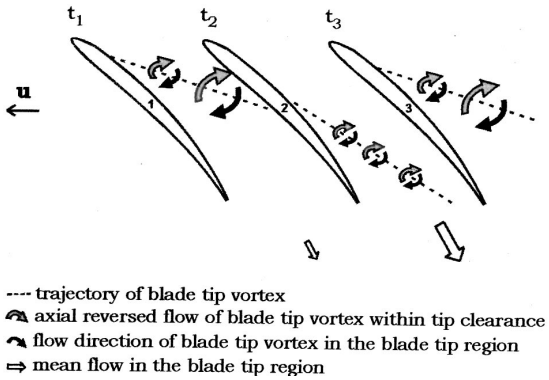

Figure 2.15: Time-dependent development of blade tip vortex, Mailach et al. [31]

2.2.2 End-wall flow

The end-wall losses arise by the formation of 3D structures of separated flow which cause large blockage effects to the flow and high entropy generation, Yu et al. [54]. One of the main types of separation, the ring-like vortex separation, is demonstrated in figure 2.16.

There are several aspects of the stator that affect the end-wall separation. The type of LE and its roughness along with the presence and size of fillet are some of these. It was concluded by Goodhand and Miller [22] that the fillet radius did not have as much of an effect as the presence of a fillet. Also the major loss impact was contributed to by the roughness of the LE and the type of LE; elliptical was better than circular. The reason behind this was that both increased the pressure spike, which in turn increased loss. Figure 2.17 quantifies the loss with respect to a baseline geometry, Goodhand and Miller [22].

There have been attempts to decrease or eliminate the end-wall secondary flow separation on the compressor SS. Some of these are:

- End-wall contouring, Reutter et al. [35], Varpe and Pradeep [50]
- End-wall boundary layer suction Gbadebo et al. [20]
- 3D blade design, see subsection 2.2.3

End-wall contouring was investigated in cascades with and without tip gaps. For a compressor cascade with a tip gap, hub contouring caused most of the benefit to occur

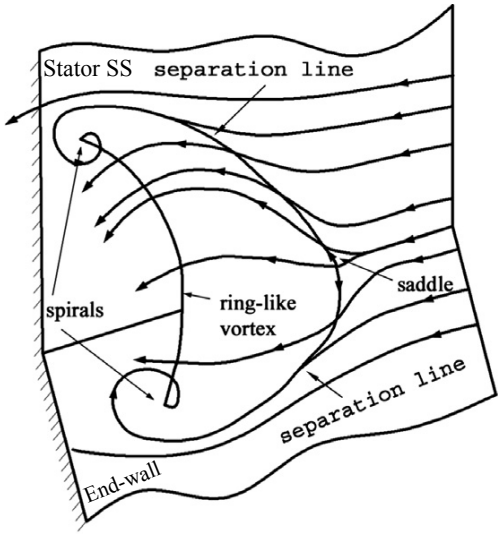

(a) Flow topology of the corner separation with a ring-like vortex on the SS, Yu et al. [54]

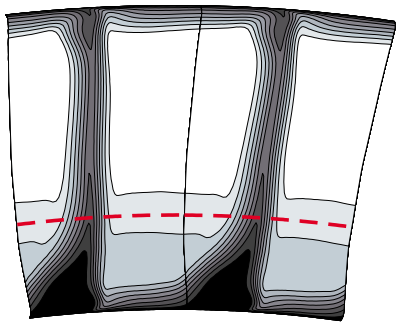

(b) Stagnation pressure loss coefficient, downstream of a stator, Goodhand and Miller [22]

Figure 2.16: Stator end-wall separation

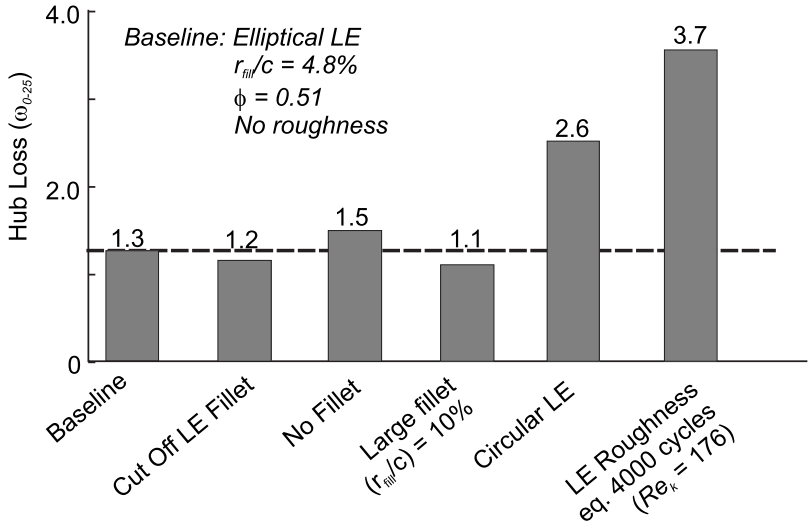

Figure 2.17: The effect of small geometry changes on hub loss, Goodhand and Miller [22]

in the region above 20% span. The vortices on the end-wall appeared to extend their influence near the tip region, thus counteracted the effect of the tip leakage vortex,

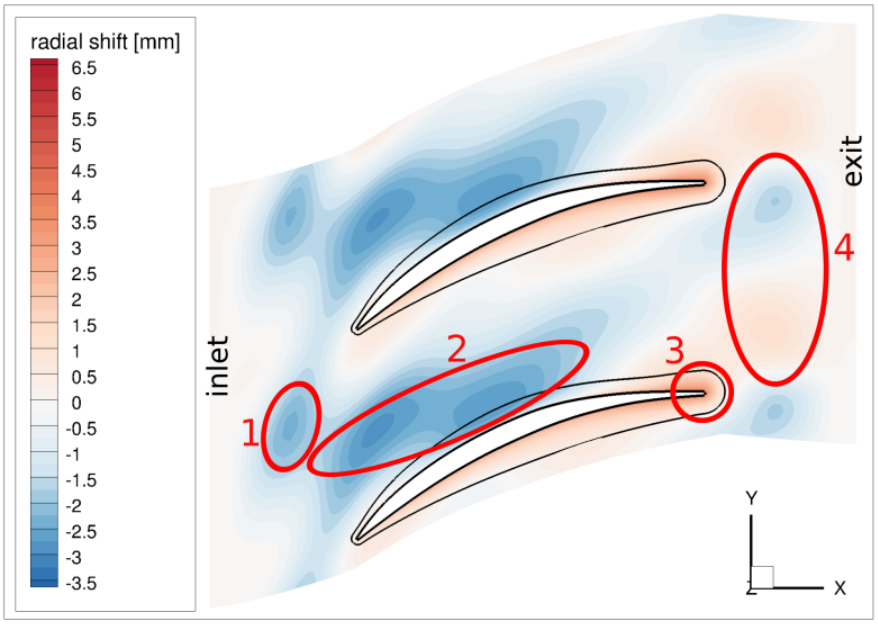

Figure 2.18: End-wall surface height contours, for the optimised end-wall, Reutter et al. [35]

Varpe and Pradeep [50]. For a cascade without a tip clearance it was found that a valley on the end-wall SS, see figure 2.18 No.1 and 2, acts as an edge that creates and guides a vortex along the SS. This vortex separates the main flow vortex from interacting with the PS and decreases the loss on the compressor, Reutter et al. [35]. There are significant differences between the two optimised end-walls discussed. They seem to be case specific but do have some similarities; which are the trough at the SS and the peak at the TE, see figure 2.18 No. 2 and 3. These have not been tested on an axial compressor yet, hence might not perform as desired for a more realistic case. As the stator hub separation is an issue for the research at hand, trying a valley along the forward region of the SS could improve the performance of the stator.

2.2.3 3D design

In recent years a better understanding has been established for the three-dimensional flow and the effect 3D design has on span-wise flow variations and secondary flow. The main 3D design methods and a detailed explanation of the effects can be found in

Denton and Xu [10].

- **Blade sweep** is the axial shifting of either the blade tip region, the blade hub region or both, see figure 2.19(left). This is to either increase or decrease the loading at various parts of the blade. A forward LE sweep reduces the loading near the LE, whereas a forward TE sweep increases the loading near the TE. A backward sweep has the opposite effect. Forward sweep is usually used to decrease end-wall effects.

- **Blade lean or Dihedral** is the tangential shifting of the blade, see figure 2.19(right). By shifting the blade in an almost frozen pressure field, the loading at the tip or hub regions can be increased or decreased. By doing so blade lean can be used to control end-wall loss and tip leakage loss.

- **Leading edge re-cambering (LER)** is the blade inlet metal angle change to account for the increased flow angle angle at the end-wall region. This is caused by the interaction of the blade row with the endwalls and the viscous force exerted to the flow by the endwalls. Thus, by changing the inlet blade metal angle to fit the flow angle better, a reduction in the SS deceleration can be achieved along with a BL that stays attached longer, Gallimore et al. [16]. After incorporating LER to the blade, there are many different methods of stacking the blade. Some of these are LE, TE and centroid stacking. Each of these creates a different 3D blade geometries. Choosing between these different stacking lines will incur unintended lean or sweep on the blade and the designer needs to be aware of it. Hence, LER is not independent from seep and lean.

- **Endwall velocity triangle design** by Auchoybur and Miller [1] can be used to change exit flow of the rotor endwalls to better accommodate the stator endwall inlet and decrease the loss associated with the endwall corner separation.

As Sasaki and Breugelmans [39] concluded, the forward swept blades formed an oppositely sensed vortex that counteracts the passage vortex. This vortex supplied the SS end-wall corner with high-energy flow that would delay the onset of corner separation.

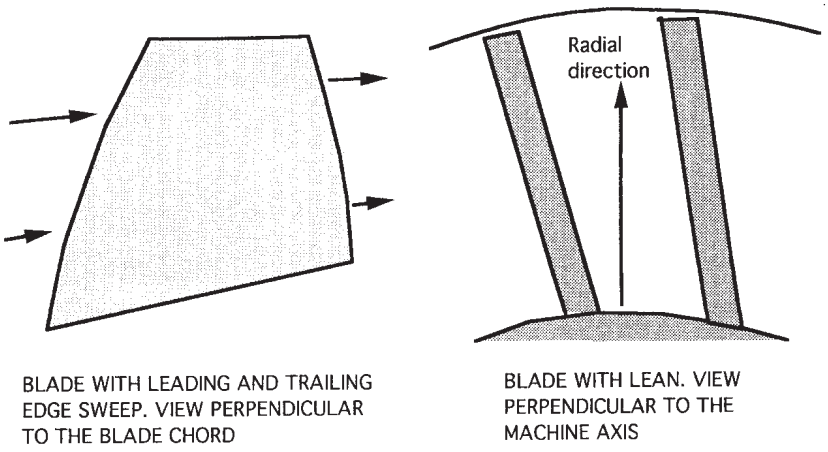

Figure 2.19: Definitions of sweep and lean, Denton and Xu [10]

Compound lean, lean at both tip and hub, decreases the loading at the least efficient parts of the blade. The loading is mainly in the midspan, thus the end-wall and tip losses are reduced. Another reason behind the preferred compound lean is the migration of low energy end-wall flow to the midspan, thus the mixing losses are not concentrated near the end-walls and an overall lower loss is achieved. Unloading the tip with lean has proven to decrease the tip gap loss for compressors, Bolger [3]. Even though, the end-wall loss was decreased, the midspan loss increased. Overall the range of incidence angles was greater with lean rather than sweep.

Both methods are mainly used for stall margin improvement rather than loss reduction. For the compressor investigated in this dissertation compound lean was investigated in attempting to decrease the tip and end-wall loss.

Gallimore et al. [16] implemented LER and positive dihedral to both the stator and rotor. The stator loss decreased for all operating points whereas the rotor performed worse when throttled. Experiments showed that the stator end-wall separation decreased significantly whereas the rotor tip loss increased at a near-stall operation point, see figure 2.20. Ramakrishna and Govardhan [34] showed that stagnation pressure loss across a rotor decreases once forward swept. The greater decrease was noticed at off design flow coefficients - at these cases the pressure coefficient near the tip was higher than that of the unswept rotor.

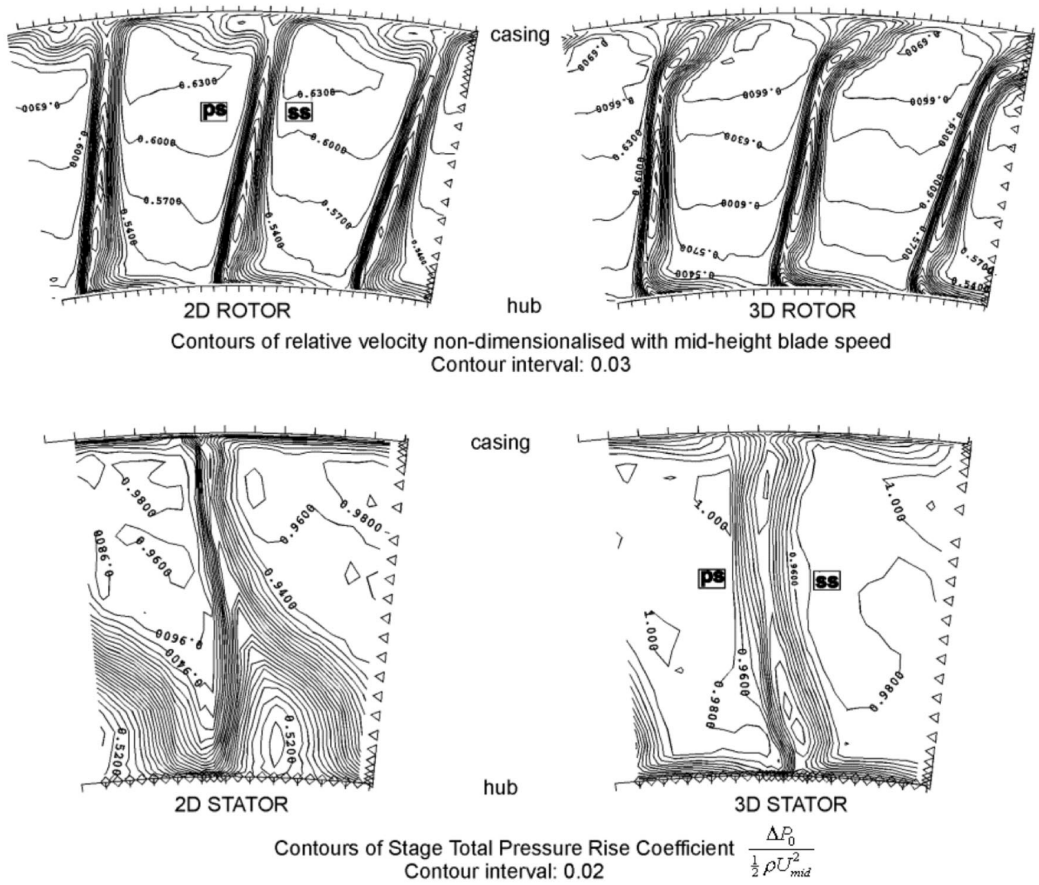

Figure 2.20: Comparison of measured 2D and 3D blade row exit conditions at a near-stall operating point, Gallimore et al. [16]

2.3 Summary

In this chapter it was shown that the scale of the experimental rig with respect to the size and positioning of the data acquisition instrumentation is important. For fast, high accuracy and high resolution data the use of miniature probes with short narrow connecting tubes, as discussed by Grimshaw and Taylor [23], is essential.

The review of the low Re literature in this chapter has revealed that the main 2D loss contribution arises from the laminar separation bubble. The main LSB loss factors are the mixing of the flow within, the pressure recovery deficit after and the blockage effect of the LSB. A decrease in the loss can be achieved by decreasing the size of the bubble. A parabolic LE and a forward maximum thickness blade have been shown

to be beneficial and are, therefore, implemented on the geometry researched in this project.

The literature on low Re 3D flow field is limited, therefore a better understanding of the flow field and its dependency on ϕ and Re is investigated in chapters 4 and 5. From the understanding of high Re 3D flow and design methodology in the literature along with the knowledge accumulated in this dissertation a study of the effect of stator endwall leading edge re-cambering and stator compound lean was carried in chapter 6. In addition, there is no literature available on how industry standard CFD performs in low Re axial compressors. In each of the following chapters the capabilities and limitations are assessed.

Chapter 3

Methods

Predominantly the results discussed in the following chapters are based on experiments conducted on a newly designed low Re, compact axial compressor rig. The design procedure and experimental methodology are described in this chapter. A partial CFD study was carried using Turbostream [4] on the Wilkes high performance GPU cluster based in the University of Cambridge. Both the experiments and simulations were based in the Whittle Lab, Cambridge.

3.1 Rig and stage designing

When designing a rig many aspects need to be taken into account.

- For high spatial resolution the size of the measuring instrumentation cannot be large compared to the working section.
- The time taken for data acquisition should be minimised without compromising the accuracy of the measurement.
- Tip gap sizes
- Flow inlet conditions

For the Reynold numbers involved with this research and the application mentioned in chapter 1 to allow for high resolution data small instrumentation has to be used.

There is an array of hot-wires and multi-hole probe designs that are available for use. There are hot-wires that can resolve from one to three directions of flow velocity and multi-hole probes ranging from one to 7 hole probes to analyse the flow direction.

For the scale of the working station and available hot-wires from Dantec-Dynamics [7], the smallest single wire probe was chosen (55P11). Bigger probes would interfere with the flow and not provide high enough spatial resolution.

Higher number of hole probes provide a higher number of redundancy to resolve the flow but decrease the spatial resolution. Also, smaller hole sizes cause an increase in the settling time between measurements, thus increasing the time needed for an experimental run. Grimshaw and Taylor [23] developed a technique to decrease the settling time while keeping the size of a 5-hole probe minimalistic. In addition Vinnemeier et al. [51] developed a method to correct for the increased size of the probe head with respect to the flow features and Hoenen et al. [27] shows how it can be used to get a more accurate flow profile.

When designing a stage for a particular application various stage parameters need to be take into account.

- Flow coefficient
- Stage loading coefficient
- Pitch to chord ratio
- Aspect ratio
- Distance between the blade rows

To and Miller [48] studied the effect of aspect ratio on 3D losses for conventional axial compressors. They showed that in stages with aspect ratio of $1.1 - 1.6$, similar to this research, 2D profile loss is slightly higher than endwall loss with minimum efficiency drop.

Extensive research was carried by Smith [42] and Van Zante et al. [49] on wake recovery with blade row axial gap. A big gap with lower blade row interaction will be less efficient but less loud compared to a small gap. An optimum at one blade axial chord was found where there is also enough space for instrumentation in the blade row axial gap.

A small scale axial compressor was designed and manufactured to investigate the effect low Re has on the flow field. For high Re axial compressors maximum efficiency can be achieved at $\psi = 0.5 - 0.6$ whereas for lower Re the higher efficiencies can be achieved at $\psi = 0.3 - 0.35$, as per Dickens and Day [11] and Maffioli et al. [30]. A lower stage loading, for a zero swirl inlet, means that there is less turning of the flow by the blade thus decreasing the pressure rise. Also Maffioli et al. [30] investigated pitch to chord ratios at low Re and found that a compromise between high wetted area loss and high separation loss gives an optimum pitch to chord ratio of 1.2.

From Maffioli et al. [30], at low Re, the deviation angle is more uniform for incidence angles between -10° and 10° at ψ greater than 0.35, compared to ψ less than 0.35 where the deviation increases to more than 15° at high incidences. In addition, flow coefficients lower than 0.5 achieved earlier separation and reattachment, whereas the highest efficiencies were reached at flow coefficients higher than 0.6. The choice of $\phi = 0.55$ and $\psi = 0.40$, see table 3.1, were selected to maximise efficiency and promote early separation and turbulent reattachment. Since, turbulent boundary layers have more momentum that laminar, they can cope with the suction-side adverse pressure gradient and stay attached along a longer part of the surface. A total to total efficiency of a 2D cross section of 93% was estimated using MISES[53], by Maffioli et al. [30].

The loading factor and flow coefficient were calculated using the following:

$$
\begin{aligned}
U_{mid} &= \frac{2\pi\omega r_{mid}}{60} \\
\psi &= \frac{\Delta h}{U_{mid}^2} = \frac{\overline{V_{\theta 2}} - \overline{V_{\theta 1}}}{U_{mid}} \\
\phi &= \frac{\overline{V_{x_1}}}{U_{mid}}
\end{aligned}
$$

The applications considered in this research have a compressor diameter of the order of $28mm$. To facilitate accurate high resolution experimental measurements, the compressor was scaled-up for the rig design, by a factor of 5, the final design parameters being shown in Table 3.1.

Table 3.1: Table with stage design parameters

	Symbol	Value
Design flow coefficient	ϕ_D	0.55
Design Loading factor	ψ_D	0.40
Reaction	Λ	0.79
Rotor chord-wise Reynolds number	Re_D	6×10^4
Absolute inlet Mach number	M	0.09
Hub to tip ratio	HTR	0.65
Tip Radius	r_t	$67mm$
Rotor axial chord	c_r	$9.3mm$
Specific speed	N_s	1.5
location of maximum thickness		$0.2c_r$

While Re, using equation 3.1, was matched in the scaled design, the Mach number in the experiment is lower than at full scale, which was $M \simeq 0.7$. The Mach number is lower than 0.3 and as a result the flow could be treated as incompressible, allowing the use of incompressible analysis. Following Maffioli et al. [30], pitch to chord ratios, 1.2 at midspan, and subsequently blade numbers, 19 rotors and 17 stators, were chosen as a compromise between high wetted area friction loss versus and a better guided passage flow.

$$Re = \frac{(c_t V_1)_{mid}}{\nu} \tag{3.1}$$

The rotor and stator blade sections are shown in figure 3.1. Following Maffioli et al. [30], the sections are forward loaded with maximum thickness at 20% chord, to reduce 2D profile losses at low Re. Table 3.2 shows the design metal angles, the pitch to chord ratio and the true chord for the sections of the rotor and stator shown in figure 3.1. The

rotor midspan section was the closest equivalent to the section discussed in Maffioli et al. [30] and where the data were compared with. Since the 3D flow features at these low Re were not known, no 3D design geometry features were initially used for the design of the rotor and stator.

Table 3.2: Table with blade section parameters

	% **span**	χ_{inlet}	χ_{exit}	$\frac{s}{c}$	c_t (mm)
Rotor casing	100	65.5°	43.5°	0.87	16.5
Rotor mid	50	62.1°	33.1°	1.2	15.0
Rotor hub	0	57.8°	23.8°	1.5	14.25
Stator casing	100	39.1°	0°	1.2	18.8
Stator mid	50	41.4°	0°	0.97	19.6
Stator hub	0	38.0°	0°	0.73	20.8

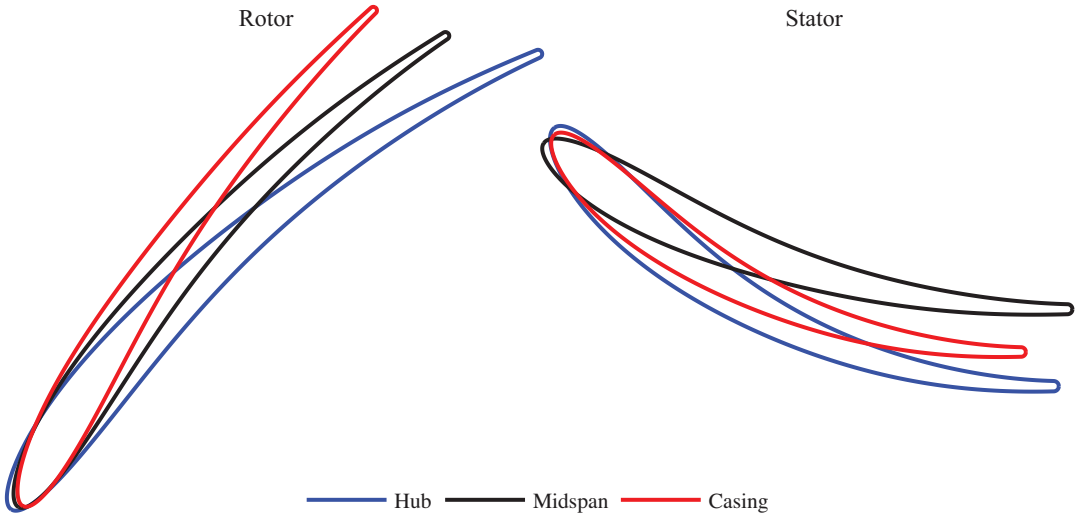

Figure 3.1: Rotor and Stator blade sections of the test compressor stage

A parabolic leading edge was chosen as per Goodhand and Miller [21], to prevent any spikes, see figure 2.4, that can lead to separation with no reattachment on the suction

side, which would increase losses. In addition, a negative incidence (inlet flow angle lower than the metal angle) for both the rotor and stator was applied at the design point to decrease pressure loss at off-design conditions, see figure 3.2. Both rotor and stator sections were centroid-stacked, which provides more structural strength for these small scale blades.

To minimise the blade rows there are no inlet guide vanes, therefore a zero inlet swirl was chosen and implemented in the rig. In an effort to achieve a high total to static efficiency the stage exit tangential velocity had to be minimised therefore at the exit a zero swirl angle was implemented in the design.

A free vortex design was used to specify the spanwise variation of blade angles such that $r\Delta V_t$ and V_x are constant. The free vortex design was chosen to provide a uniform axial velocity along the span.

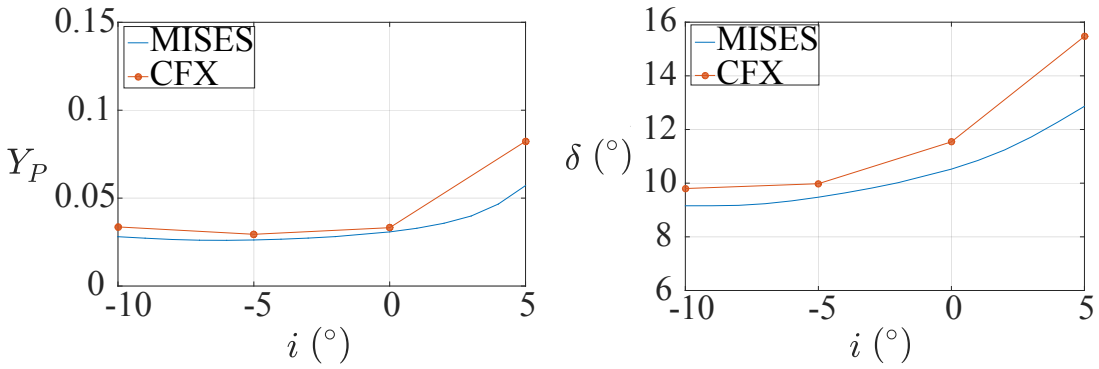

Figure 3.2: Pressure loss and deviation angle variation with incidence angle for a front loaded low Re section, Maffioli et al. [30]

3.1.1 Rotor and stator assembly

The rotor and stator blade numbers are 19 and 17 respectively, as shown in figure 3.3. Prime numbers were chosen to eliminate any acoustic resonance between the rotor wake passing frequency and the stator.

The minimum hub diameter of the full scale compressor stage is limited by the outer diameter of the digital motor driving the rotor. It is housed in the hub of the compressor. Therefore the hub to tip ration and tip diameter were chosen accordingly to provide the

required mass flow at the design speed. The rig tip diameter was chosen as $134mm$, a 5 times scale-up of a $26.8mm$ diameter full scale compressor, and the hub diameter was $85.6mm$. Therefore the hub to tip ratio was 0.65.

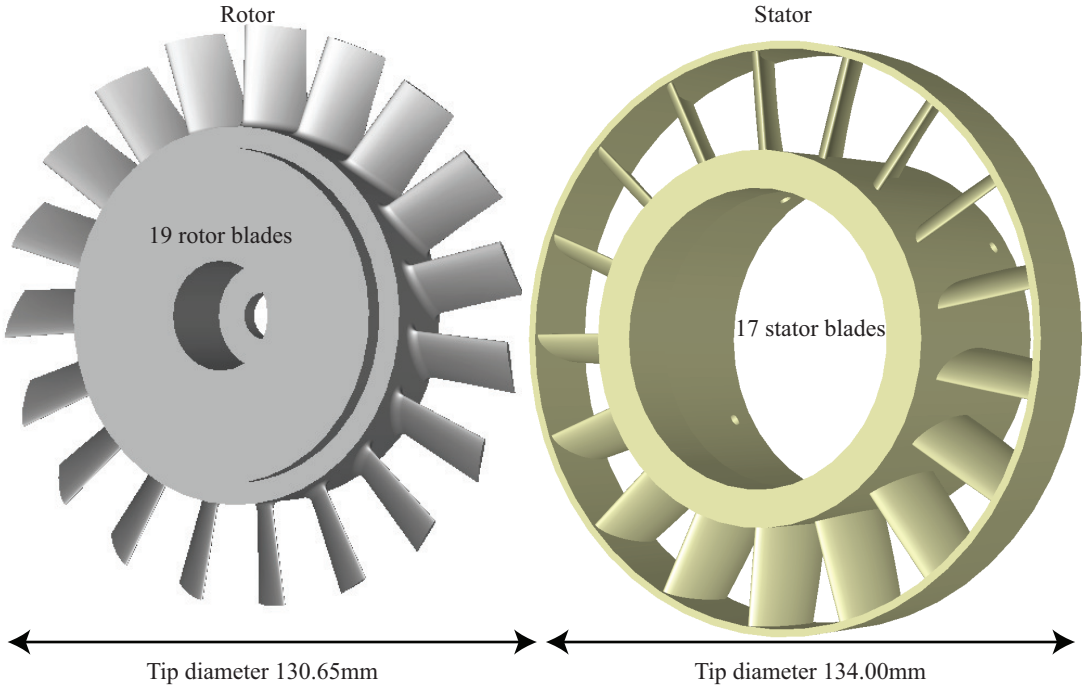

Figure 3.3: Rotor and stator CAD designs

The axial distance between the rotor and stator was chosen to be equal to one axial rotor hub chord, common practice for single stage axial compressors. It's a compromise between a large inefficient gap with low flow interaction (quiet) and a small more efficient gap with high flow interaction (loud). Also, a smaller gap would make it harder to access and traverse the rotor wake. Extensive research was carried by Smith [42] and Van Zante et al. [49] on wake recovery with blade row axial gap, which showed potential efficiency and range benefits for shorter gaps.

The rotor tip gap width was chosen as 2.5% of the rotor span. The smallest tip gap that can be accurately manufactured and aligned for the full scale rotor is $0.1mm$. Therefore keeping the same scale as the rig, this corresponds to approximately 2.5% of the rotor span or 4% of the rotor tip true chord. This is a large tip gap compared to the commercial high Re compressor tip gaps. This corresponds to increased tip vortex

mixing losses and decreased flow coefficient range, as discussed by Zhang et al. [55] and Hewkin Smith et al. [26].

3.1.2 Rotor finite element analysis (FEA)

A finite element analysis analysis at the motor's highest rotational speed, $24000rpm$, was carried out on the rotor. The aluminium alloy AL7075 was chosen to machine the rotor from. Its high tensile strength, 5.70×10^8, and yield strength, 5.05×10^8, along with its machinability made it a good candidate. SolidWorks simulations, was used to conduct an FEA analysis of a rotor section with a cylindrical symmetry constraint and a rotation speed of $24000rpm$, the maximum achievable rotational speed of the rig. A $2mm$ radius fillet was set at the root of the rotor, scaled from the true size compressor application. Figure 3.4 shows the boundary conditions and mesh used for the FEA.
The solution to the FEA is shown in figure 3.5(left) (residual absolute displacement) and figure 3.5(right) (factor of safety). The maximum displacement was found to be located at the tip region of the rotor. The magnitude was of the order of $1.4 \times 10^{-5}m$ and the tip clearance absolute value was $4.5 \times 10^{-4}m$, there is more than an order of magnitude difference thus the displacement would neither affect the flow nor cause rubbing.
Under this loading, the regions with the highest stresses are the blade root leading edge and the root of the blisk. Nevertheless, the minimum factor of safety is above 10, thus the rotor is safe from yielding at all operating speeds. A simplified hand calculation was carried, using the centrifugal load of the blade, to find the stress acting on the root of the blade. This was expected to be a highly loaded part of the blisk. The factor of safety was calculated at 26, using equation A.1 in Appendix A, further supporting the conclusion that the rotor will not fail.
The stator does not experience any rotational loads, therefore the yield strength of the material used was not as important. The Whittle lab 3D printer was used to manufacture the stator introduced in this chapter and all the subsequent chapters, The material used was an ABS representative by Stratasys.

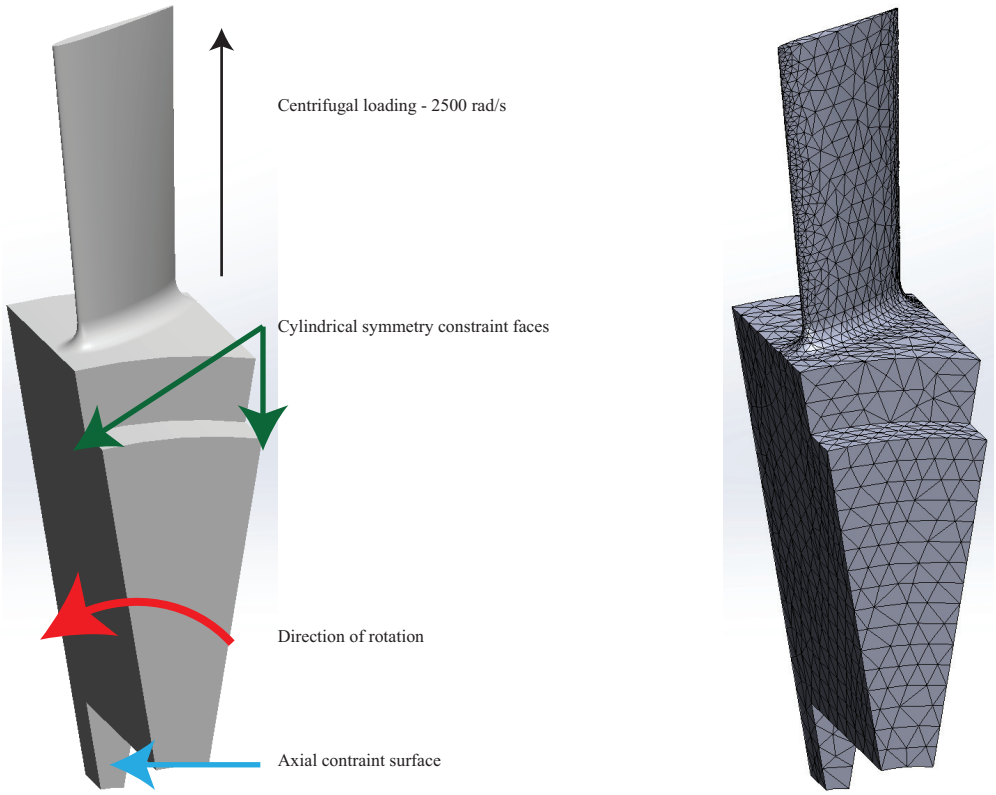

Figure 3.4: Rotor FEA boundary conditions (left) and mesh (right) applied to AL7075

3.1.3 Inlet

The axial length of the inlet duct was designed to be one casing circumference long with an elliptical bell-mouth. This length was chosen as a compromise between a long inlet with high boundary layer blockages and a short intake that affects the rotor inlet flow. A $10mm$ pitch and $50mm$ width honeycomb was used between the bell-mouth and the duct. This eliminated any non axial flow that formed in the bell mouth. The bell-mouth has a $1 : 1.5$ elliptic shape. The duct radius is equal to the ellipse minor axis, which is common for low speed compressors, see figure 3.6a.

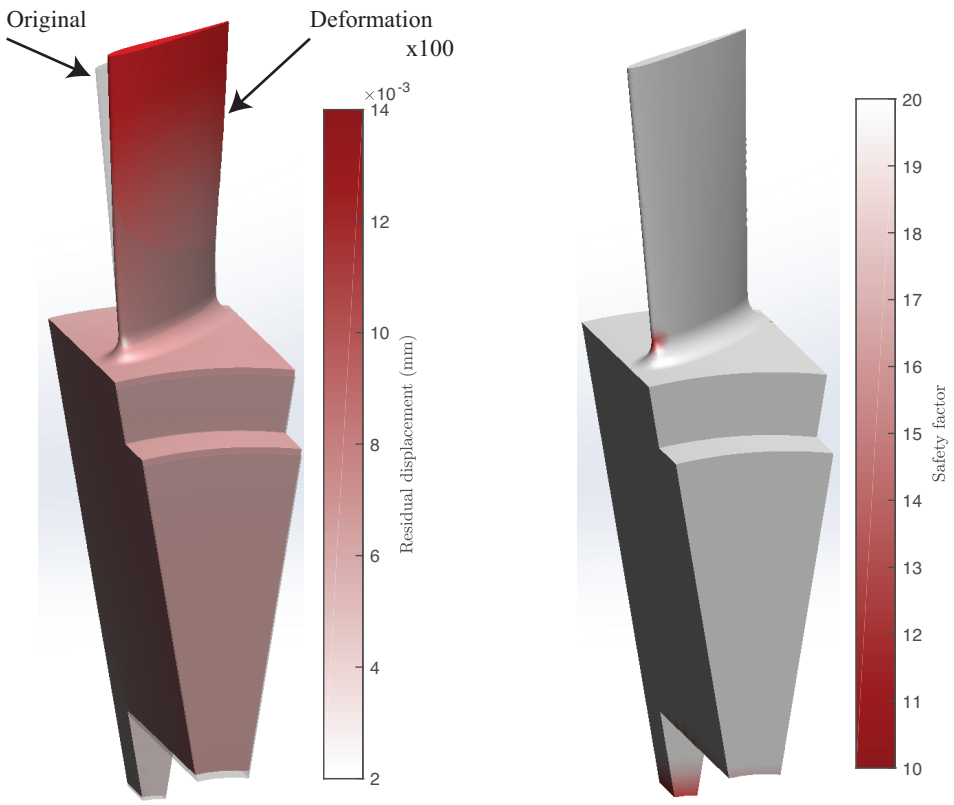

Figure 3.5: Rotor FEA analysis

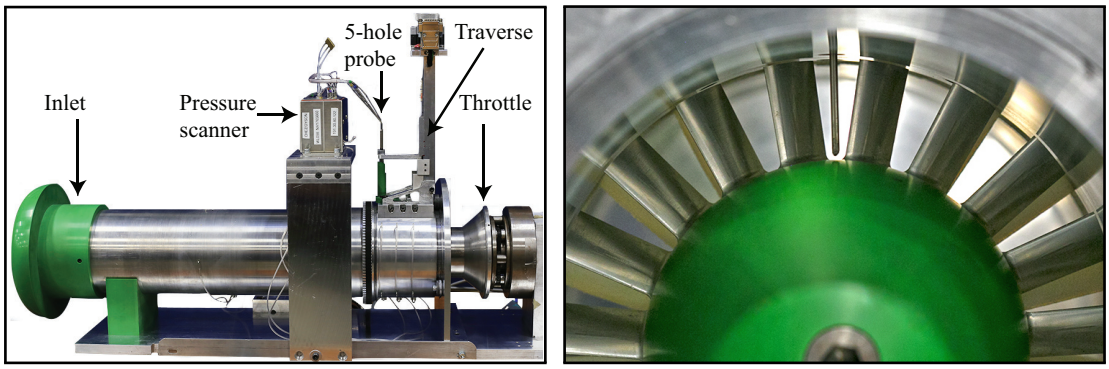

(a) Test rig illustrating the proximity of the pressure scanner to the 5-hole probe

(b) The 5-hole probe positioned at rotor inlet (station 1)

Figure 3.6: Experimental rig set-up

3.1.4 Instrumentation

The main instrumentation used for the data logging are as follows:

- NIDAQ PCIE-6323 and BNC-2110, by National Instruments, for data acquisition and analogue to digital conversion.
- DSA3217, by Scanivalve, for pressure analogue to digital processing, with an accuracy of 0.20% on the full range of $2500Pa$, as stated by the manufacturer calibration.
- FCO332, by Furness Controls, $150Pa$ range with an accuracy of 0.25% on the reading.
- Miniature $1mm$ head diameter 5-hole probe, made in-house, for pressure and angle profiling, Grimshaw and Taylor [23].
- Dantec Miniature straight wire probe (55P11) with a straight Support (55H20), for unsteady rotor exit traverses, Dantec-Dynamics [7].
- StreamLine signal amplifying system (90CN10/C10), for hot-wire probe signal amplification.

3.1.5 Traverse

A rotary table, see figure 3.8, was used to rotate the casing and is responsible for the circumferential traversing of the 5-hole probe and the hot-wire. A motorised slider, see figure 3.7, was used for the radial traversing of the probes. Both were controlled remotely via the data-logger software. The casing is supported by 3 PTFE cylinders acting as bearings, 2 of which are visible in figure 3.8 and allowed to rotate freely .

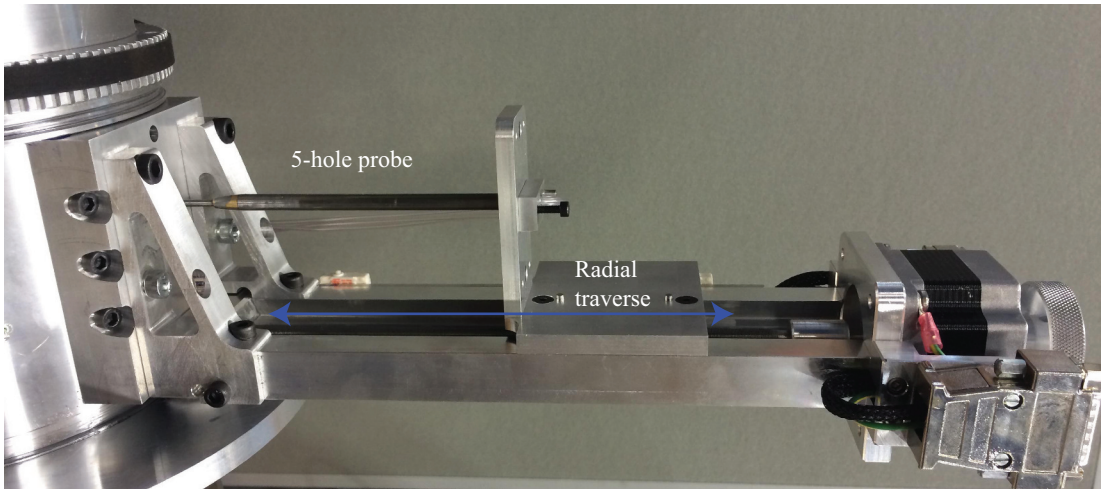

Figure 3.7: Slider used for radial traverse

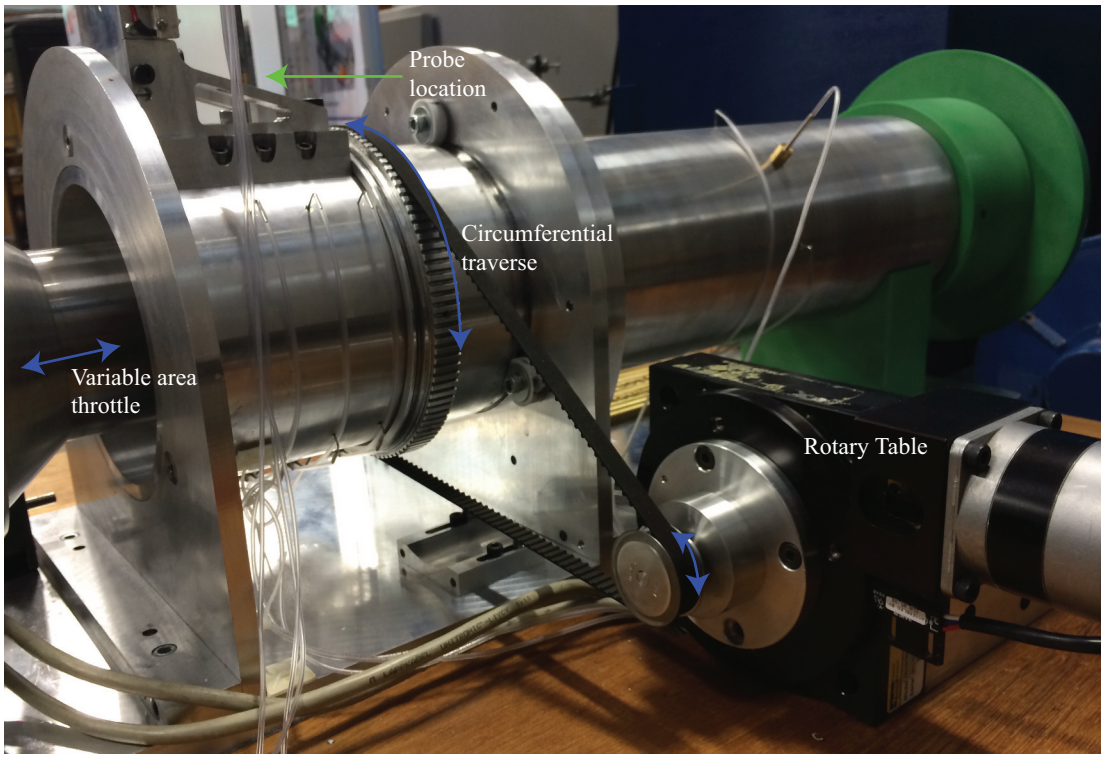

Figure 3.8: Rotary table used for circumferential traverse

3.2 Experimental procedure

The flow coefficient was controlled using a variable area motorised throttle, figure 3.6a, at the stage exit and the operating Re of the rig was adjusted through setting the rotational speed. The rotational speed was remotely set from the data logger onto the motor power supply. Since the flow conditions vary with ambient conditions, the flow coefficient thus the flow speed was not calibrated against a throttle position. Instead an inlet 5-hole probe radial traverse was conducted to calculate the operating point after altering the location of the throttle.

For $Design$ and $Near\ stall$ flow coefficients, the traverse was repeated after a change in the throttle position, until the flow coefficient calculated was within 2 significant figures of the desired value. Area traverses using a 5-hole probe were performed at three stations, labelled 1 to 3 in figure 3.9.

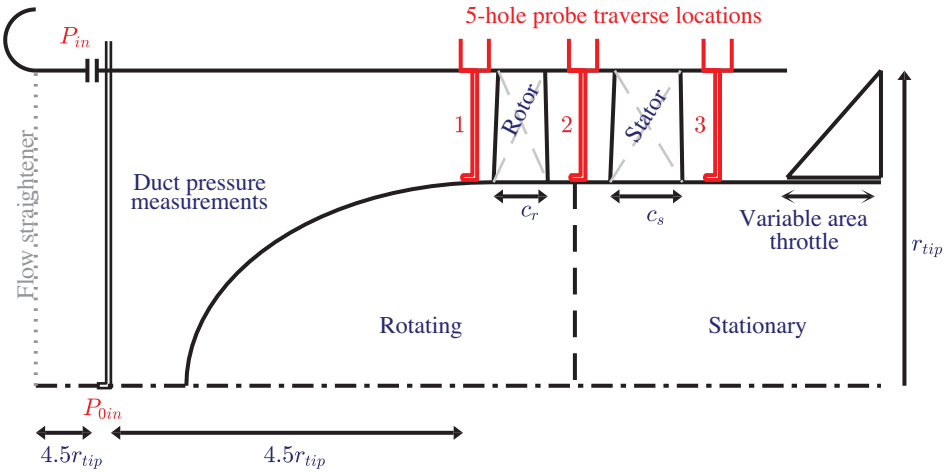

Figure 3.9: Rig schematic (not to scale) showing traverse locations

To find out the operating range of the rig at $Re_D = 60,000$ a simple test was carried out. The complete range of the throttle was split into 1000 linearly spaced steps. The midspan and mid-passage stator exit static pressure was recorded using the 5-hole probe along with the duct static and stagnation pressure. The static pressure rise was calculated using equation 3.2 and plotted on figure 3.10. The flow coefficient plotted in figure 3.10 was calculated using equation 3.3. This neglects any blockage effects due to the duct boundary layers for simplicity, thus the calculated flow coefficient is

higher than the true one. For all other flow coefficient calculations to follow, the rotor inlet traverse is always used to calculate the flow coefficient for a more accurate value.

$$\begin{aligned} \rho &= \frac{P_a}{RT_a} \\ C_p &= \frac{P_3 - P_{0_d}}{\frac{1}{2}\rho {U_{mid}}^2} \end{aligned} \tag{3.2}$$

$$\begin{aligned} A_d &= \pi {r_c}^2 \\ A_1 &= A_d - \pi r_h^2 \\ V_{x_d} &= \frac{2\sqrt{P_{0_d} - P_d}}{\rho} \\ V_{x1} &= V_{x_d}\frac{A_d}{A_1} \\ \phi &= \frac{V_{x_1}}{U_m} \end{aligned} \tag{3.3}$$

Two regions of stall can be observed after the maximum pressure rise peak. Following Day [8] “Stall 1” is expected to be a part span (tip) stall cell and “Stall 2” a full span stall. However, the post-stall behaviour was not in the scope of this research. In the following sections detailed traverse results are presented at the $Design$ and the $Near\ Stall$ flow coefficient, which is the last continuously stable operating point.

3.2.1 5-hole probe traverses

The flow at the rotor inlet, exit and stator exit was measured using a miniature 5-hole probe, see figure 3.6b, with an outer diameter of 4.4% of blade span. The probe was in the presence of large pressure gradients, for example see figure 3.11. Due to the probe relative size to the flow gradient a probe geometry correction calculation was adapted to account for the relative location of the probe bores, both in the circumferential and radial direction. The method used is introduced by Vinnemeier et al. [51] and used by Hoenen et al. [27].

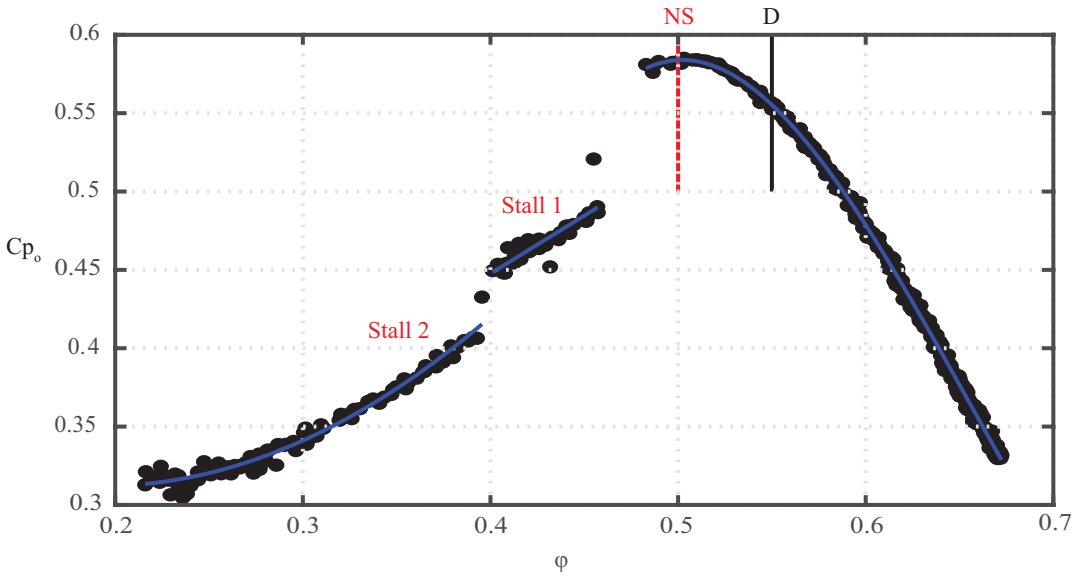

Figure 3.10: Measured static pressure rise characteristic at Re_D, showing ϕ_D and ϕ_{NS}

The traditional method of calculating the flow parameters at position "n", all five hole pressures would be used to calculate them. Since the flow gradient is comparable to the probe size, it would be more appropriate to use hole 4 pressure from position "n-1" and hole 2 pressure from position "n+1". Therefore using the knowledge of the probe hole locations with respect to the flow, the correct pressure can be interpolated from the traverse map. This process is used both in the circumferential and radial direction. For the outermost points of the traverse map as in figure 3.11(left), since there is no recording of hole 4 pressure at location "n-2" then the pressure at location "n-1" was used. This was deemed acceptable as the gradients at the chosen outliers were low.
The miniature 5-hole probe was connected to the 16-channel pressure scanner that was mounted in close proximity with $300mm$ of $0.4mm$ inner diameter tubes, following Grimshaw and Taylor [23] and as shown in figure 3.6a. Due to the narrow hypodermic tubes used in the probe head, $0.185mm$ inner diameter, the friction forces are high and the velocity of the signal is low. Therefore short and small diameter tubes were used to allow for a smaller settling volume downstream of the probe head. This decreases settling time, as it takes less time for the pressure transducer to equalise between readings. By taking a continuous reading of the pressure from the centre hole of the 5-hole probe for 10 seconds, the settling time was chosen at $1.3s$ where the pressure was

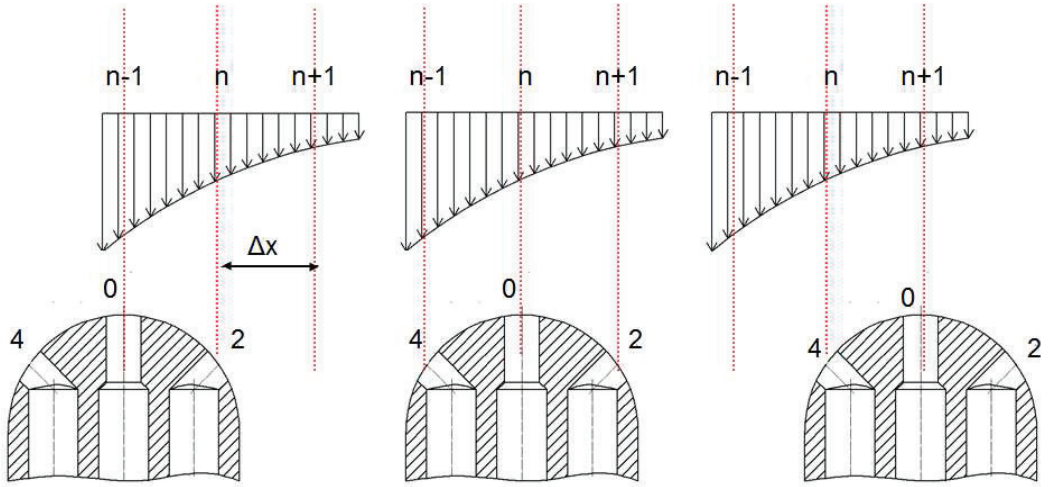

Figure 3.11: Traversing of a five-hole probe in a gradient field, Hoenen et al. [27]

within 0.5% from the pressure at the 10^{th} second.

The probe was calibrated following Dominy and Hodson [13] to give a calibration map with a wide range, pitch ($\pm 25°$) and yaw ($\pm 35°$) with a resolution of $1°$. The coefficients for total pressure, static pressure, yaw and pitch are given in Equations 3.4 to 3.7.

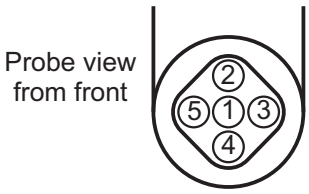

Figure 3.12: Probe hole allocation

The probe hole orientation is depicted in figure 3.12. The probe was calibrated using the Whittle Laboratory high speed calibration tunnel at a range of flow speeds, from $10\ \mathrm{m/s}$ to $60\ \mathrm{m/s}$. Figure 3.13 shows the calibration map at a speed of $30\ \mathrm{m/s}$. A line of best fit (spline) interpolation was used to extract the corresponding maps.

$$C_{P_0} = \frac{P_0 - P_{cn}}{P_{cn} - \frac{1}{4}(P_{up} + P_{dn} + P_{lf} + P_{rt})} \tag{3.4}$$

$$C_P = \frac{P_0 - P}{P_{cn} - \frac{1}{4}(P_{up} + P_{dn} + P_{lf} + P_{rt})} \tag{3.5}$$

$$C_{yaw} = \frac{P_{rt} - P_{lf}}{P_{cn} - \frac{1}{4}(P_{up} + P_{dn} + P_{lf} + P_{rt})} \tag{3.6}$$

$$C_{pitch} = \frac{P_{up} - P_{dn}}{P_{cn} - \frac{1}{4}(P_{up} + P_{dn} + P_{lf} + P_{rt})} \tag{3.7}$$

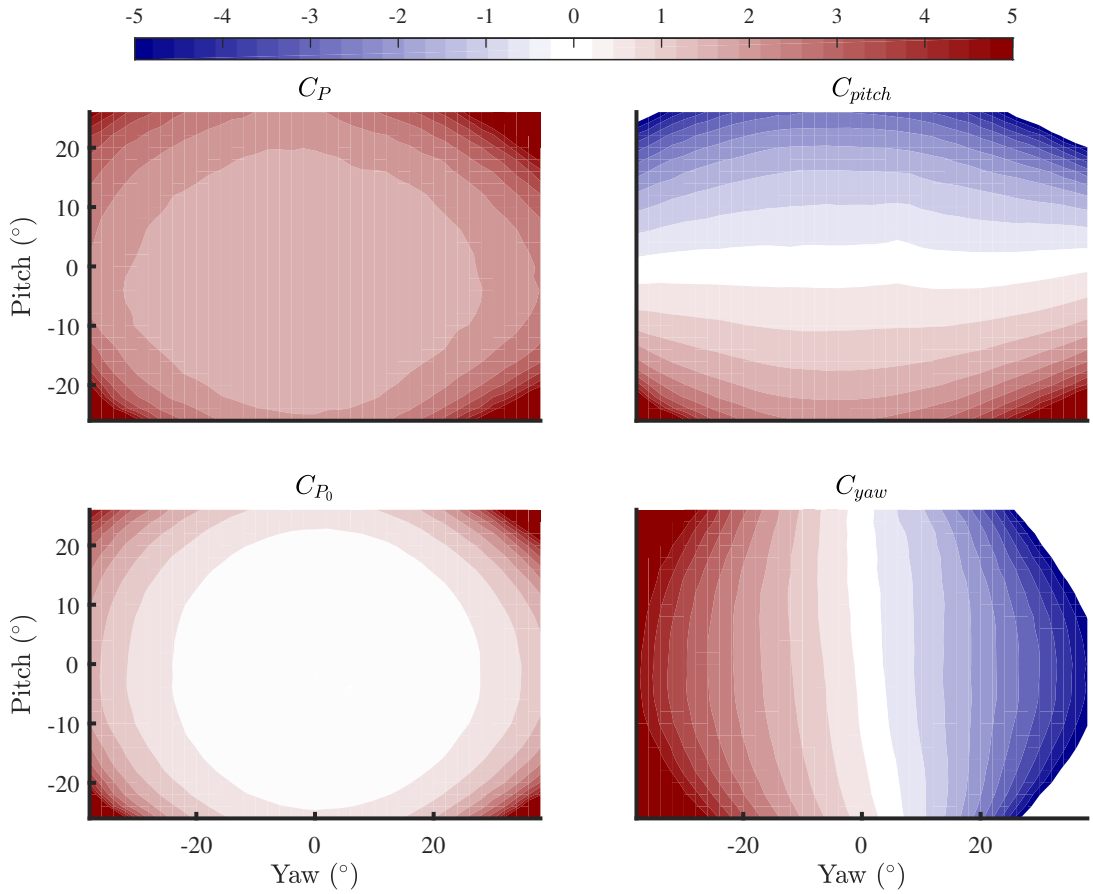

Figure 3.13: 5-hole Probe calibration map at a speed of 30 m/s

The probe was mounted at an angle of 0°, 40° and 15° at stations 1, 2 and 3, respectively. This was done to position the probe closer to the expected mean flow angle, to

stay within the previously stated calibration. A feeler gauge was used to set the probe head $0.05mm$ from the hub, allowing a significant portion of the hub boundary layer flow to be captured.

At all three traverse stations there were 32 radial points with endwall clustering. At the rotor exit and stator exit, there were 16 and 32 circumferential points covering one stator pitch, with the wake centralised. Figure 3.14 shows the rotor exit and stator exit traverse mesh. The 512 rotor exit points were not clustered in the pitchwise direction, whereas the 1024 points covering the stator exit were pitchwise clustered in the expected wake region, at least 8 pitchwise points in the wake. This was achieved by initially traversing with a coarser traverse mesh to locate the wake, and then using a finer mesh, with clustering at the wake location, for the final traverse.

Since the 5-hole probe is a steady measurement device, the rotating wake of the rotor cannot be captured. The 5-hole probe measures the time averaged pressure at the rotor exit. The stator static pressure field propagates upstream of the stator into the rotor exit traverse region. Therefore, a coarse area traverse at the rotor exit can capture it and a pitchwise average can the be taken to calculate the rotor performance.

On the other hand at the exit of the stator the fine mesh is needed to capture the blade wake. The fast settling time of the probe allows a full traverse of one point on the characteristic in approximately 1 hour.

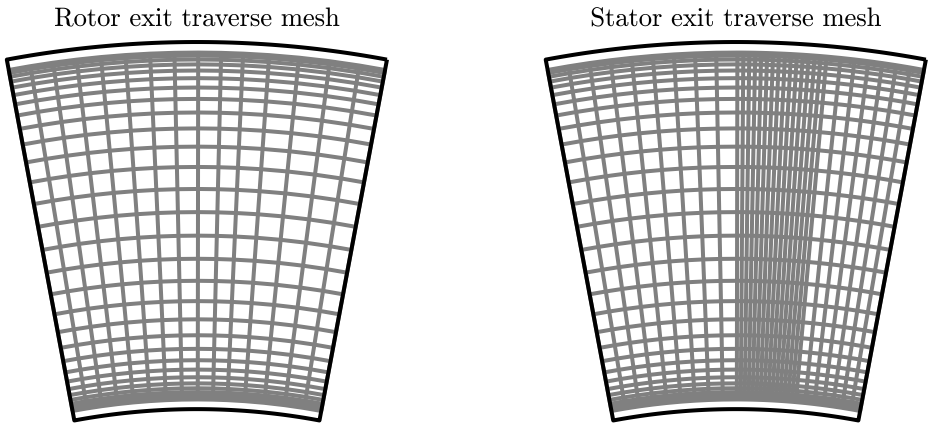

Figure 3.14: Rotor exit and stator exit traverse mesh

3.2.2 Hot-wire traverses

A Dantec Miniature straight wire probe (55P11) with a straight Support (55H20) connected to the StreamLine signal amplifying system (90CN10/C10) was used to traverse the rotor exit plane. The hot-wire sensor was calibrated in-situ using a 4^{th}-order polynomial to correlate the measured hot-wire voltage to the velocity measured by the 5-hole probe, see figure 3.16. The hot-wire was sampled at a frequency of $200kHz$ for 4 seconds, this corresponds to approximately 280 readings per rotor pitch at $Re = 60,000$. For each hot-wire traverse, the method of least squares was used on the ensemble averages, see figure **??**. A once per revolution signal was used to trigger the sampling and locate each blade passing for the ensemble averaging process.

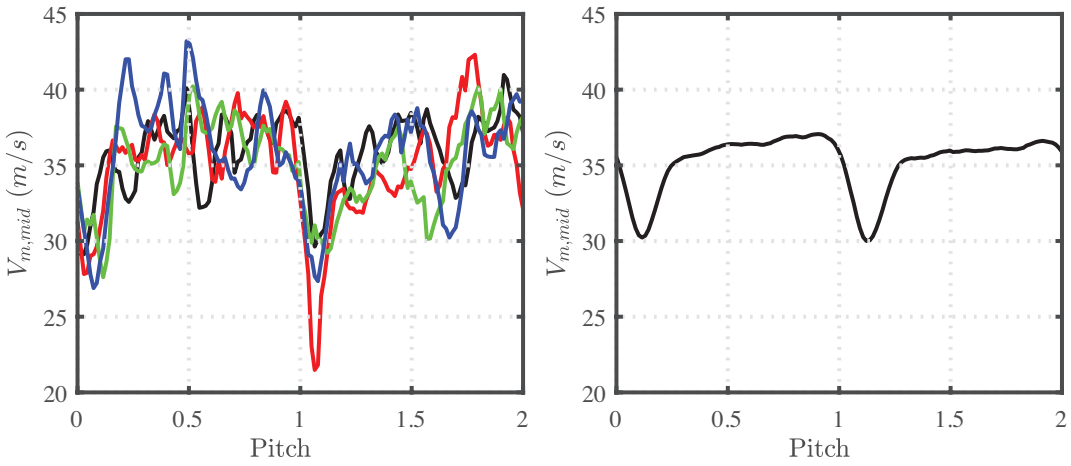

Figure 3.15: Hot-wire raw (left) and ensemble averaged (right) midspan meridional velocity across 2 pitches

A single straight wire probe has a typical response to yaw angle as depicted in figure 3.17. Hence, by rotating the probe at known yaw angles and recording the velocity the response of the probe can be recorded. Then by interpolating through the curve for the maximum velocity, the flow meridional velocity and yaw angle can be calculated.
From the design of the stage it was known that the mean flow angle at the exit of the rotor would average at about $40°$. The bracket in charge of holding the probe was therefore fitted with 9 linearly spaced probe angle locations from $-6°$ to $90°$, as in figure 3.18.

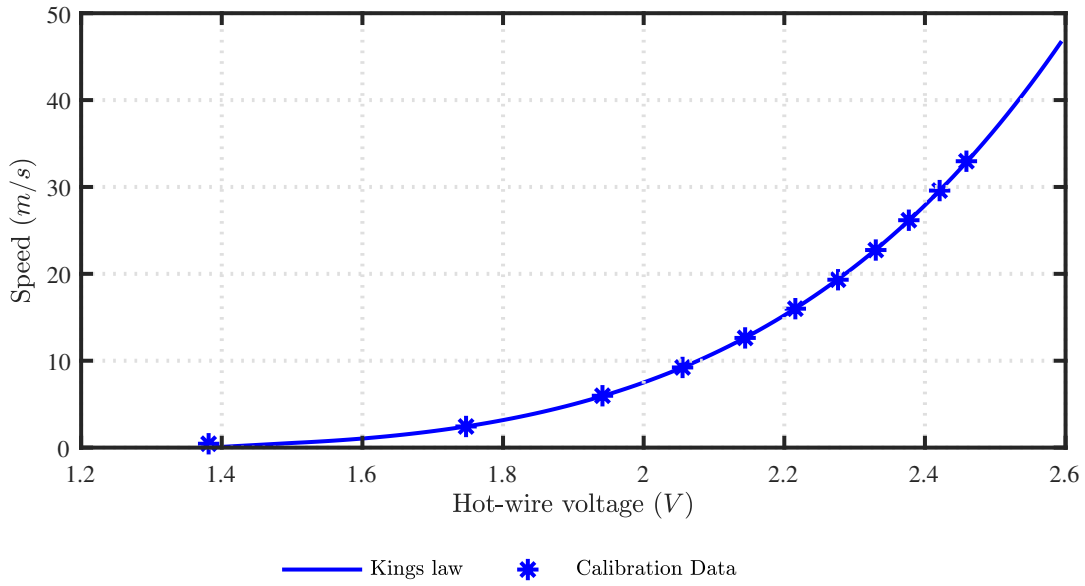

Figure 3.16: Hot-wire calibration curve

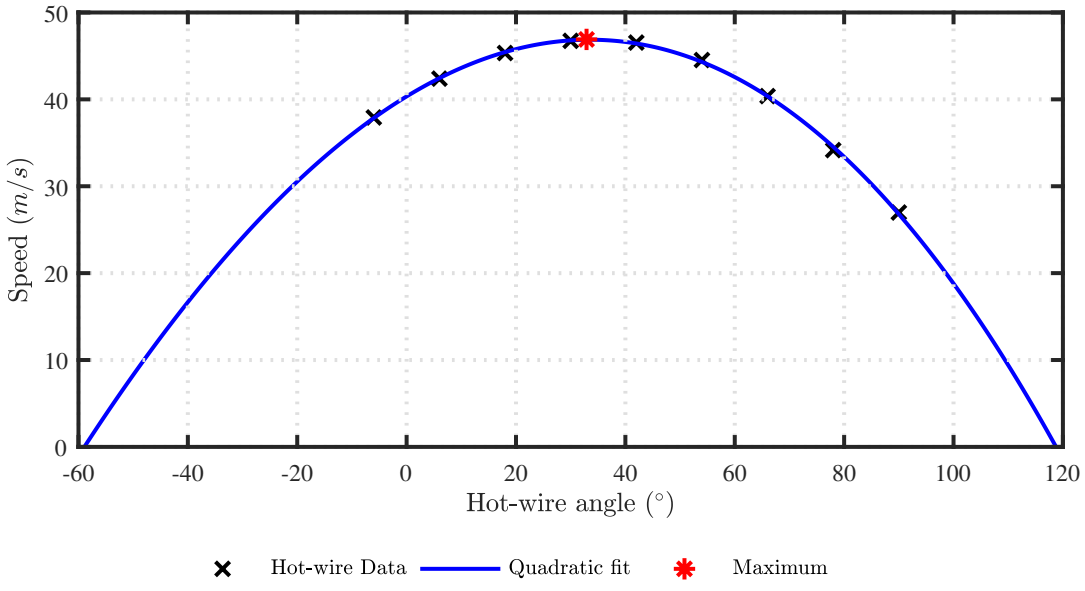

Figure 3.17: Hot-wire response curve to yaw angle

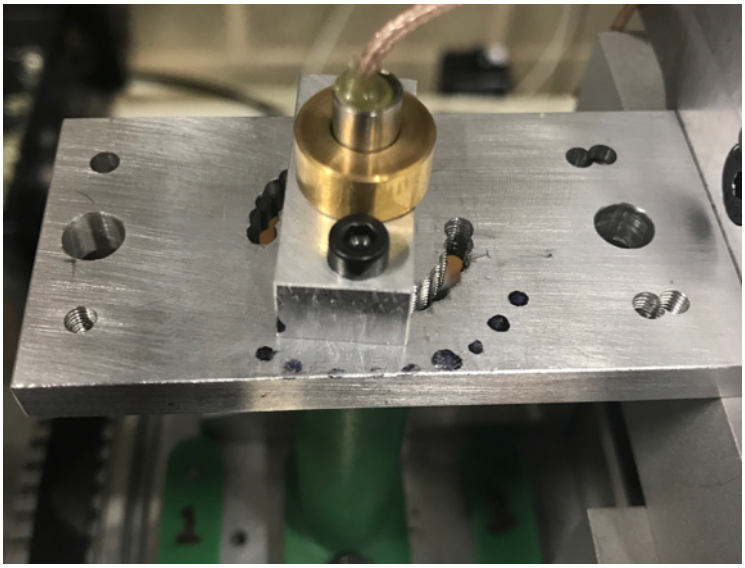

Figure 3.18: Hot-wire probe support with 9 yaw angle locations

3.2.3 Error analysis

This thesis involves measuring low flow velocities at the lower Re. The DSA3217 quoted accuracy, 0.20% on $2500Pa$, was not high enough to guaranty the accuracy of the measurements. The FCO332 pressure transducer, $150Pa$ range with an accuracy of 0.25% on the reading, was used to calibrate the DSA3217 at the low pressure range. Figure 3.19 show the experimental pressure along with the line of best fit. An error of 0.66% gain was calculated. The error was low enough to allow the DSA3217 to be used to measure at this low pressure region. In addition, an error analysis of the repeatability of the experiments was carried out giving a maximum of 4% difference between the expected and experimentally calculated value. For example, using figure 5.9 and equation 3.8 the trend line equivalent value does not differ by more than 4% from the experimental value.

$$\text{Percentage differernce} = \frac{Y_{P_{\text{EXP}}} - Y_{P_{\text{trend line}}}}{Y_{P_{\text{EXP}}}} \tag{3.8}$$

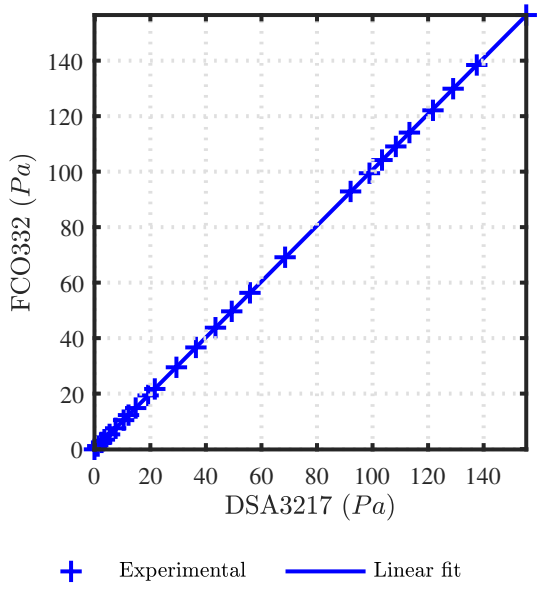

Figure 3.19: DSA3217 measured pressure versus FCO332 measured pressure

3.3 Computational methods

This section provides a description of the setup and techniques used for the numerical part of this thesis.

3.3.1 Computational solver set-up

The single stage compressor was modelled by meshing a single passage using Autogrid5, NUMECA [32]. There are 100 spanwise mesh points, of which 17 are in the tip gap. A minimum wall cell width was set at $5 \times 10^{-6}m$ to ensure $y^+ < 5$ for the use of the "Spalart-Allmaras" turbulence model, Spalart and Allmaras [43], along with "wall function" treatment at the surfaces. The total mesh comprises of 1.2 million cells.
The domain extends $1.5c_r$ upstream of the rotor leading edge to $3.5c_r$ downstream of the stator trailing edge, see figure 3.20. The rotor nose cone has not been simulated to simplify the geometry and decrease the mesh size to be simulated, because after the initial rotor inlet traverses it was found that the nose cone had no significant effect on the inlet flow field. From the experiments it was found that the effect of the nose cone is negligible. A spanwise uniform stagnation pressure of $101,875Pa$, a temperature of

$293.5K$ and $0°$ swirl were set as the inlet boundary conditions. A static pressure with simple radial equilibrium was set at exit to fix the operating point. The static pressure at the exit would then be increased in stages to reach the $Design$, $Near\ Stall$ and lowest fully converge flow coefficient. The blade-to-blade mesh at midspan is depicted in figure 3.21. The rotor blade surface and tip gap mesh is depicted in figure 3.22.

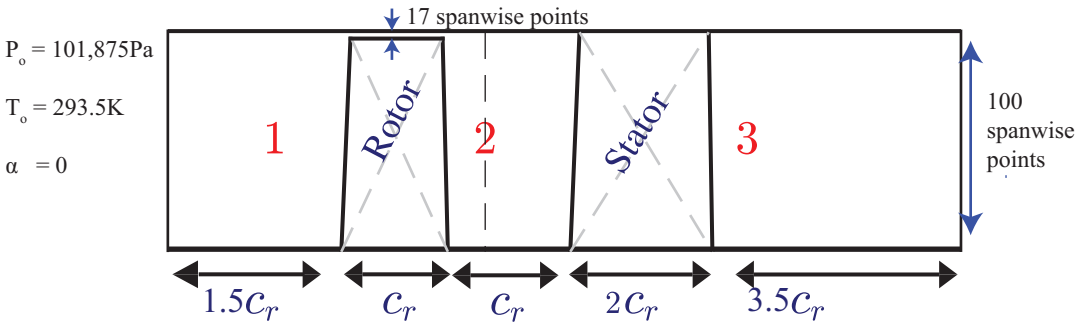

Figure 3.20: CFD domain

Fully turbulent 3D RANS simulations were conducted using Turbostream 3.14, Brandvik and Pullan [4]. The flow at the investigated Re is transitional, a flow characteristic that is not expected to be captured when run fully turbulent. Turbostream has been validated for various turbomachinery applications, with $Re > 10^5$, such as Pullan et al. [33], Taylor and Miller [47], Grimshaw et al. [24], Gunn and Hall [25].

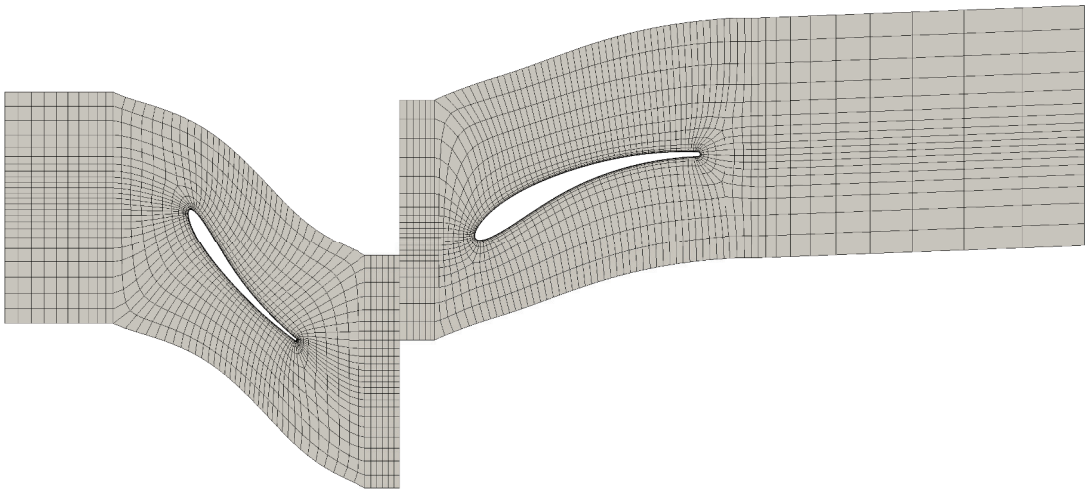

Figure 3.21: Blade-to-blade mesh at midspan

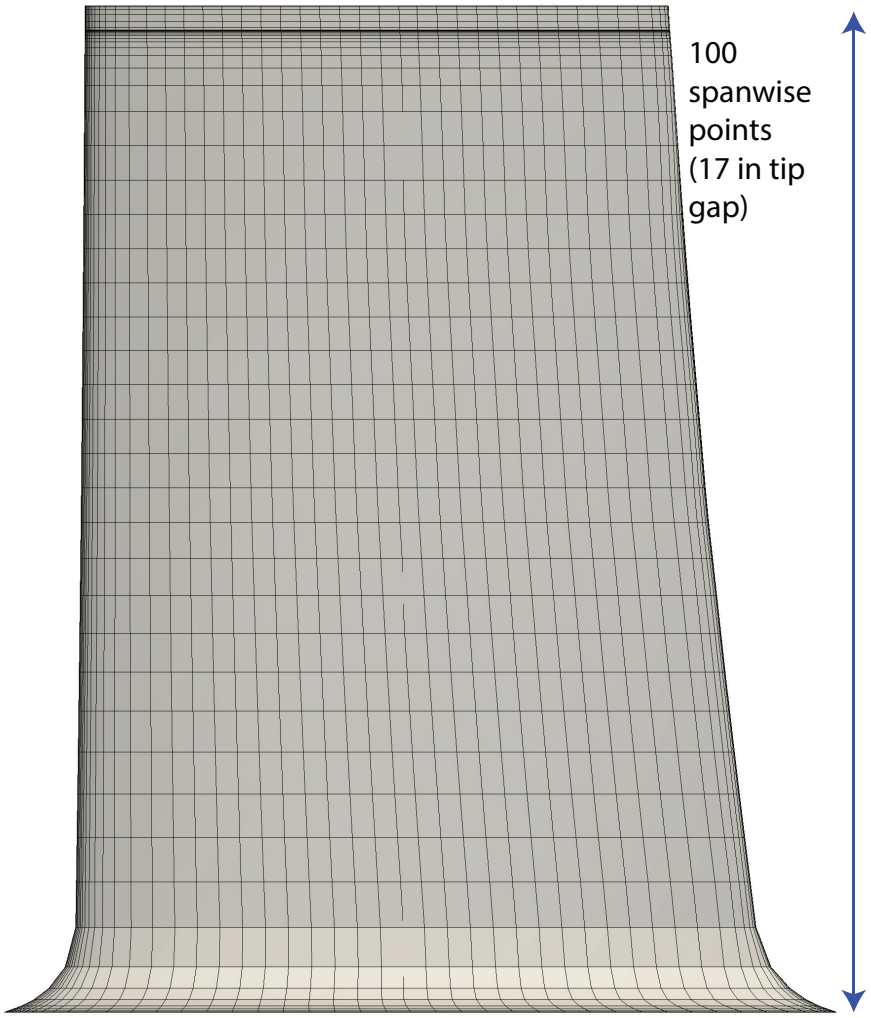

Figure 3.22: Rotor blade surface and tip gap mesh

3.3.2 Computational investigation parameters

Turbomachinery industry relies greatly on steady RANS simulations for their design process. Part of the reason is its time and cost effectiveness versus LES and DNS and partly the confidence after validation it provides makes it a valuable tool. Therefore steady RANS was chosen for the simulations in this research. However, the Re investigated in this research is outside the range of most common turbomachinery applications, thus there has been no validation. Also, at this low Re the flow is transitional.

The available options in current CFD solvers are: using transition models (not available in Turbostream), fully turbulent flow with partial laminar patches or running fully turbulent without using laminar patches.
Transition models are still not very reliable, hence it was decided to not use any. The location of transition in the flow at this unfamiliar Re is not well understood, therefore running fully turbulent steady RANS was chosen. Allowing in the future to introduce laminar patches once the flow field is better understood would be a way to improve the simulations. However, in this thesis emphasis was given to what aspect of the flow fully turbulent steady RANS could and could not calculate, giving designers a more informed view of the limitations of the CFD when designing at this low Re.
The parameters investigated in the CFD are listed below:

- **Rotor tip clearance:** The rotor tip clearance sizes that were investigated were, 0.10%, 0.50%, 0.75%, $0.1.25\%$, 1.5%, 1.50%, 2.00%, 3.00% and 5.00%, of span across the whole range of flow coefficient. The mesh distribution was kept the same with 17 radial points in the tip gap.

- **Reynolds number:** The Re was controlled with the rotational speed as in the experiments and the values investigated where, $20,000$, $30,000$, $40,000$, $60,000$, $80,000$, $100,000$ and $120,000$, across the whole range of flow coefficient. The Mach number was matched with the experiments.

- **Flow coefficient:** The ϕ was controlled by changing the stator exit static pressure to match a designated mass flow.

- **3D Geometry:** There were two stages of stator re-designs, stator endwall leading edge metal angle re-cambering and stator compound lean to decrease endwall losses. Across the whole range of flow coefficient.

3.3.3 Convergence

All simulations were run for $200,000$ iterations and are considered converged if both of the following have been achieved, as shown in figure 3.23:

- Residuals have decreased by at least 2 orders of magnitude (DAVG).

- For the last $20,000$ iterations the inlet and exit mass flows have not changed by more than 2%

Then, the parameters are averaged over the last $20,000$ time steps and used in the results chapter of this thesis.

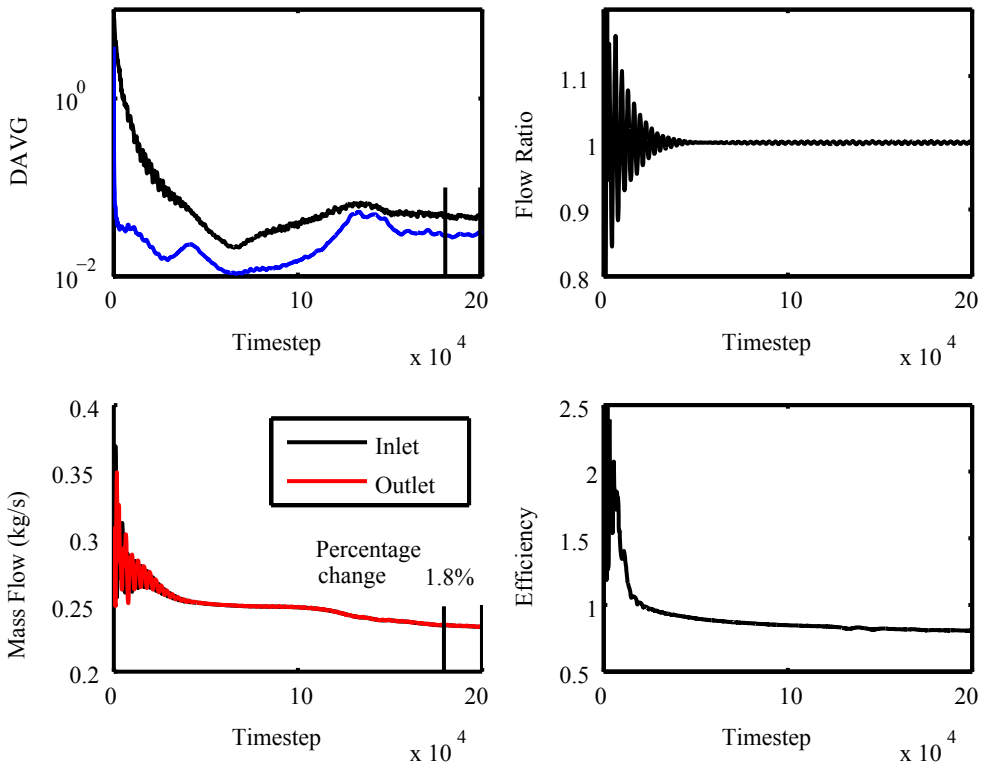

Figure 3.23: Convergence plots of a converged simulation

3.4 Post-processing

Paraview and MATLAB scripts where used to process the data from the experiments and the simulations. The $1D$ and 2D results plotted in the figures on the following chapters were calculated using incompressible mass weighted averaging, as in equation 3.9. All of the contour plots, figure 4.5 for example, used threshold values to remove

outliers and for better visibility of the flow features. The same averaging methods were used on the experimental traverse data as well. The stagnation pressure loss across the rotor was calculated using equation 3.11. Finally, the rotor and stator loss breakdown was calculated using equations , from Appendix B

$$\overline{\text{property}} = \frac{\sum_{i=1}^{n}(AV_{x_i})\ \text{property}_i}{\sum_{i=1}^{n}(AV_{x_i})} \tag{3.9}$$

$$Y_{p_{\text{rotor}}} = \left(\frac{\overline{P_{01}} - \overline{P_{02}}}{\overline{P_{01}} - \overline{P_1}}\right)_{\text{relative}} \tag{3.10}$$

$$Y_{p_{\text{stator}}} = \left(\frac{\overline{P_{02}} - \overline{P_{03}}}{\overline{P_{02}} - \overline{P_2}}\right)_{\text{absolute}} \tag{3.11}$$

$$\text{Rotor loss}_{\text{ casing, mid, hub}} \cong [w \times \frac{0.5(W_1^2 Y_{p,rotor})}{V_{t2}U_2}]_{\text{casing, mid, hub}} \tag{3.12}$$

$$\text{Stator loss}_{\text{ casing, mid, hub}} \cong [w \times \frac{0.5(V_2^2 Y_{p,stator})}{V_{t2}U_2}]_{\text{casing, mid, hub}} \tag{3.13}$$

3.5 Summary

This chapter has provided an experimental methodology for measuring the 3D flow field within a low Reynolds number axial compressor. The design of the test facility has been discussed and a summary of the key instrumentation, working sections and measurement locations have been provided. Additionally, the chapter provides details on the structural analysis of the spinning components of the rig in order to ensure the rig's safety.

Chapter 4

Low Reynolds Number Axial Compressor Flow Field

This chapter focuses on three areas. First, it looks at understanding the loss sources of a low Re axial compressor stage, both at $Design$ and $Near\ Stall$, using 5-hole probe and hot-wire traverses. Second, it quantifies the loss breakdown between the blade hub, mid and tip regions for both the rotor and stator at low Re, along with the loss breakdown as the operating point is changed from $Design$ to $Near\ Stall$. Third, this chapter focuses on recognising the capabilities and limitations of industry-standard fully turbulent RANS, at low Re.
The compressor aerodynamic performance and flow field at $Re_D = 6 \times 10^4$, at $Design$ flow coefficient, $\phi_D = 0.55$, and $Near\ Stall$ flow coefficient $\phi_{NS} = 0.50$ are presented.

4.1 Comparison to design intent

Pitchwise mass weighed averaged rotor and stator properties are presented here. The measured flow field is compared with the design intent. Figure 4.1(left) shows the spanwise axial velocity distribution at the rotor inlet, rotor and stator exit using 5-hole data. At rotor exit, there is both a hub and casing velocity deficit, approximately

20% of the span, characteristic of a corner separation and a tip clearance vortex core, respectively.

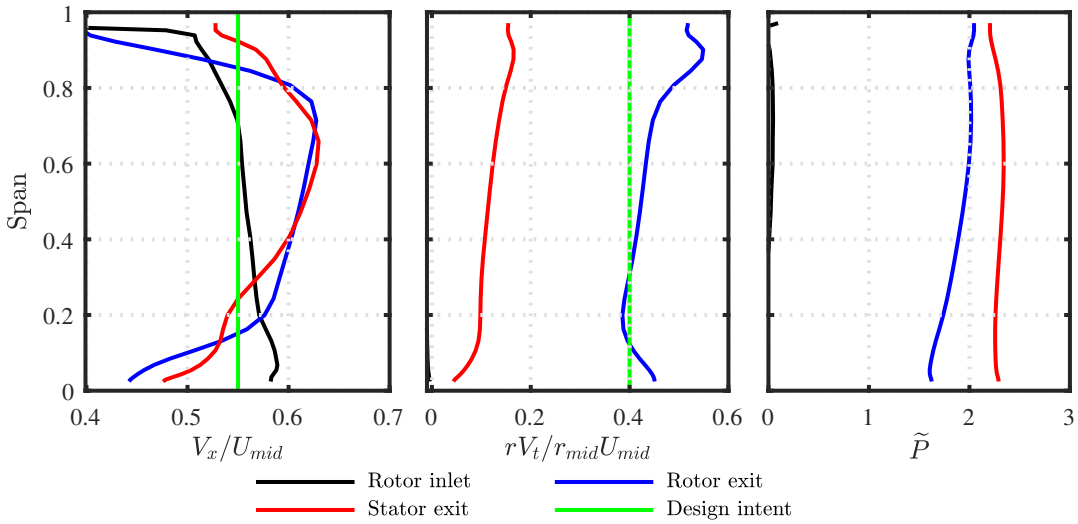

Figure 4.1: Spanwise, pitch-averaged, distribution of non-dimensional axial velocity, angular momentum and static pressure at Re_D and ϕ_D

The region of velocity deficit is classified as the region of the span where the velocity is lower than the average velocity at that station. The deceleration of the high entropy endwall boundary layer when it interacts with the rotor suction side causes a three-dimensional separation which increases the rotor loss, as discussed in Denton [9]. The difference in velocity of the spilling fluid from the pressure side to the suction side creates the swirling flow. The mixing of the two flows causes the tip clearance vortex loss which is classified as a 3D flow loss, as discussed in Denton [9].

At the stator exit, the endwall velocity deficit covers approximately 30% of the span, both at the hub and casing region. Even though the velocity deficit covers a larger proportion of the span, the deviation from the mean velocity is smaller. This is an indication of corner separations, larger than the rotor but of lower intensity. At this point it is not clear whether the 2D or 3D flow features are more dominant. In the angular momentum distribution at rotor exit, 4.1(mid), the midspan region follows the free vortex design, as designed. Whereas the tip and hub regions are more highly loaded, thus an indication of a high loss region.

The stator exit angular momentum shows that there is swirl at the exit of the stator. Any swirl must arise from a separated stator suction surface, which in turn incur pressure loss along the span. From the research conducted by Maffioli et al. [30] expected response of a low Re aerofoil design at these flow conditions there should be approximately 10° of flow deviation.

The 0.79 reaction designed for the stage, as in table 3.1, was achieved as the midspan static pressure rise in the stator is approximately 20% of the stage pressure rise. The swirling flow at the stator inlet causes a subsequent spanwise pressure gradient at the stator exit, which in turn causes a decrease in the stator tip loading and an increase in the hub loading.

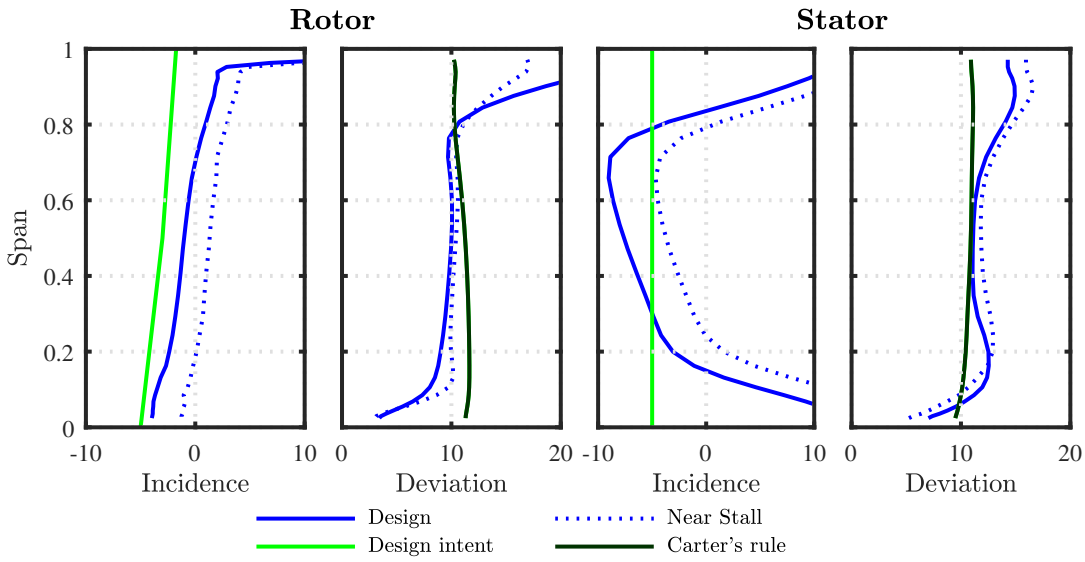

Figure 4.2: Measured spanwise incidence and deviation distributions for the rotor and stator at $Design$ (D) and $Near\ Stall$ (NS) for Re_D

Figure 4.2 shows the incidence and deviation angles at two flow coefficients, the intendant incidence angle form MISES and the expected deviation using Carter's rule. The rotor and stator were designed with negative incidence at design conditions. Due to the induced up-wash effect at the leading edge, the measured rotor incidence and "design intent" do not match-up. The deviation at the rotor exit is close to 10° for 70% of the span, with over turning at the hub due to the rotating end wall and under-turning at the tip region due to the tip vortex flow. Following Carter's rule, as in Corralejo

and Harley [6] using equation 4.1, the deviation "design intent" for both the rotor and stator is approximately $10°$, which matches the experimental results.

$$\delta_{CARTER} = \frac{(0.23 + 0,002\beta_2)\Delta\chi}{\sigma^{0.5}} \tag{4.1}$$

The highly positive incidence angles at the stator hub and casing are a result of the the axial velocity deficits in those regions, which lead to high tangential velocities. Similar to the rotor, the deviation in the stator is close to $10°$ across the midspan and higher at the endwalls due to the highly incident endwall flow at the inlet. The highly positive, greater than $5°$, incidence at the stator endwall regions are more prone to separate and not reattach, leading to high deviations and losses, as discussed in Maffioli et al. [30]. As expected the absolute flow angle distribution at stator inlet is not as designed due to the rotor 3D flow features. The effect of designing the stator inlet angles to better match the incident flow is discussed in chapter 6.

The stage and rotor total to total efficiency was calculated, from traverse data, using equations 4.2 and 4.3, respectively. The flow is assumed incompressible and that there is no inlet swirl. Figure 4.3 shows a decrease of both efficiencies as the flow coefficient is decreased from $Design$. The 2D blade efficiency expected of 93% is higher than the experiment's rotor efficiency. This difference is accounted for in the extra loss generated due to the 3D flow features discussed below.

$$\eta_{stage} = \frac{h_{03_s} - h_{01}}{h_{03} - h_{01}} = \frac{P_{03} - P_{01}}{\rho(V_{\theta 2}U_m)} \tag{4.2}$$

$$\eta_r = \frac{h_{02_s} - h_{01}}{h_{02} - h_{01}} = \frac{P_{02} - P_{01}}{\rho(V_{\theta 2}U_m)} \tag{4.3}$$

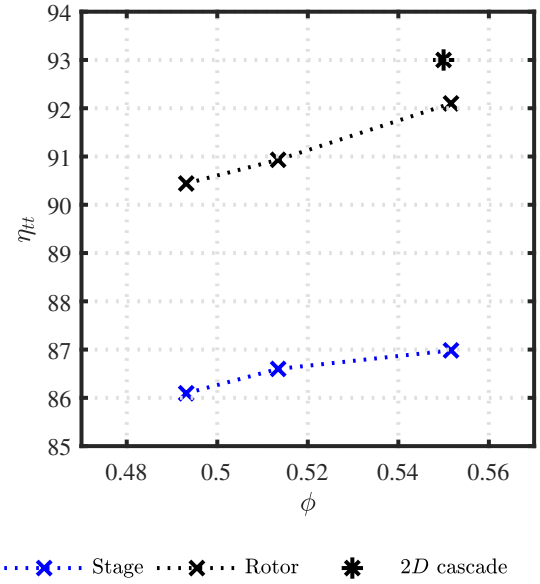

Figure 4.3: Measured total to total efficiency characteristic at Re_D

4.2 Rotor flow features

By using the CFD calculations and hot-wire traverses, the rotor exit flow field can be visualised.

With the aid of Paraview, a flow simulation post-processing tool, the rotor tip leakage flow can be visualised. Figure 4.4 depicts flow streamlines along an entropy iso-surface with non-dimensionalised velocity contours for $Design$ and $Near\ Stall$. The vortex folds over the tip close to the leading edge and that location moves upstream closer to the leading edge at the lower flow coefficient. Also off design the angle at which the vortex passes through the passage with respect to the blade stager increases. And finally, the vortex core increases in size off design.

The rotor exit flow angle and velocity contours were obtained, as described in subsection 3.2.2 and presented in figures 4.5 and 4.6. There are three distinct flow features that can be identified in the rotor flow field. The rotor tip leakage vortex, the rotor hub corner separation and the 2D profile loss due to separation near the trailing edge. The velocity deficit and high flow angle for all three features is a indication of the loss associated with them. At $Near\ Stall$ the features increase in both size and magnitude. The loss impact is further discussed in the next section.

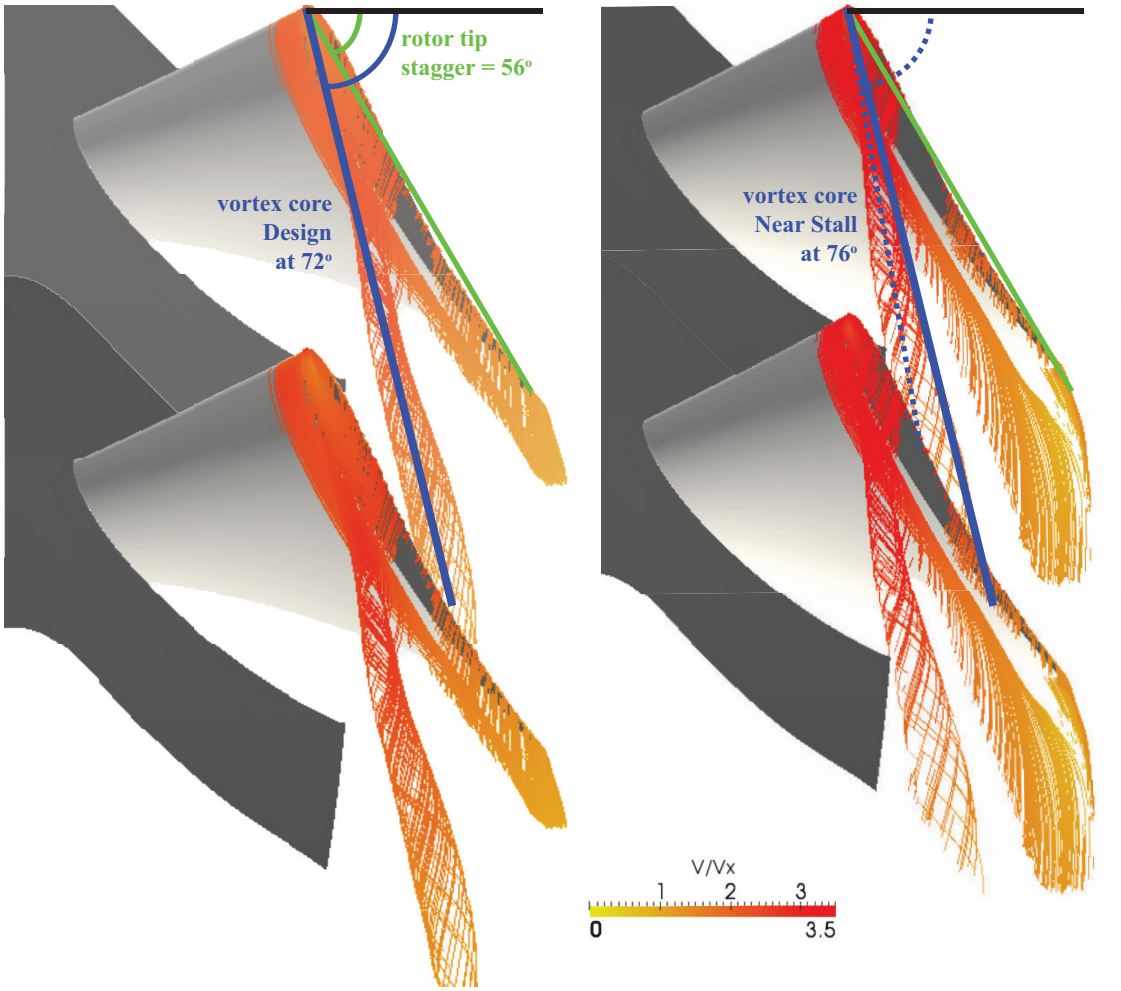

(a) Rotor tip vortex at Design

(b) Rotor tip vortex at Near Stall

Figure 4.4: Computed, steady RANS, $\frac{V}{V_x}$ streamlines for the rotor tip leakage vortex, Re_D

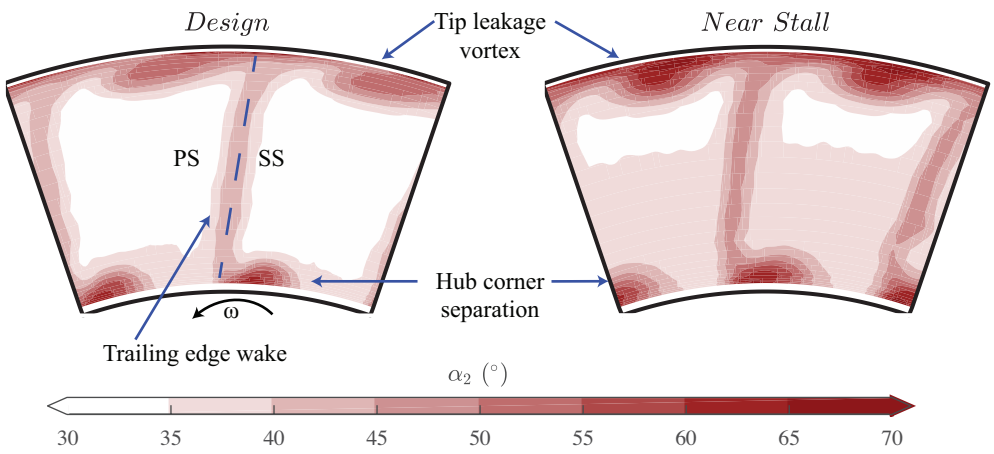

Figure 4.5: Absolute flow angle contours at the rotor exit at $Design$ and $Near\ Stall$ (hot-wire)

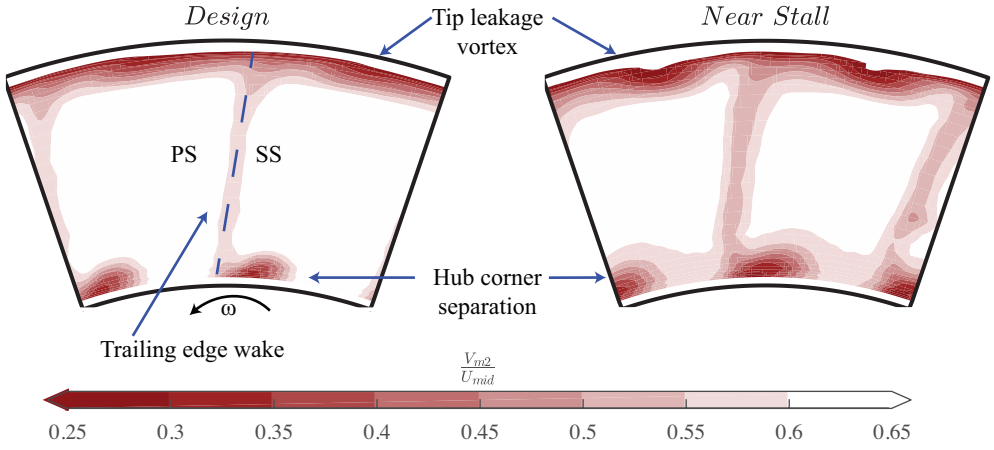

Figure 4.6: Non-dimensionalised meridional velocity contours at the rotor exit at $Design$ and $Near\ Stall$ (hot-wire)

4.3 Rotor and stator loss breakdown

Figure 4.7 shows a breakdown of the rotor and stator stagnation pressure loss at $Design$ and $Near\ Stall$, depicted as percentage of lost work. Equations 3.12 and 3.13 were used to calculate the loss breakdown. The blade rows were split into casing, mid and hub regions. The three regions were divided by a 1-2-1 mass flow ratio, respectively. The rotor casing loss is approximately 3 times larger than either of the two other regions, individually. The stator hub loss increases by 10% and the casing by 15%, whereas the rotor midspan increases by 50%. The spanwise variation of rotor loss in figure 4.8 shows that both the casing and hub loss regions occupy 20% of the span.

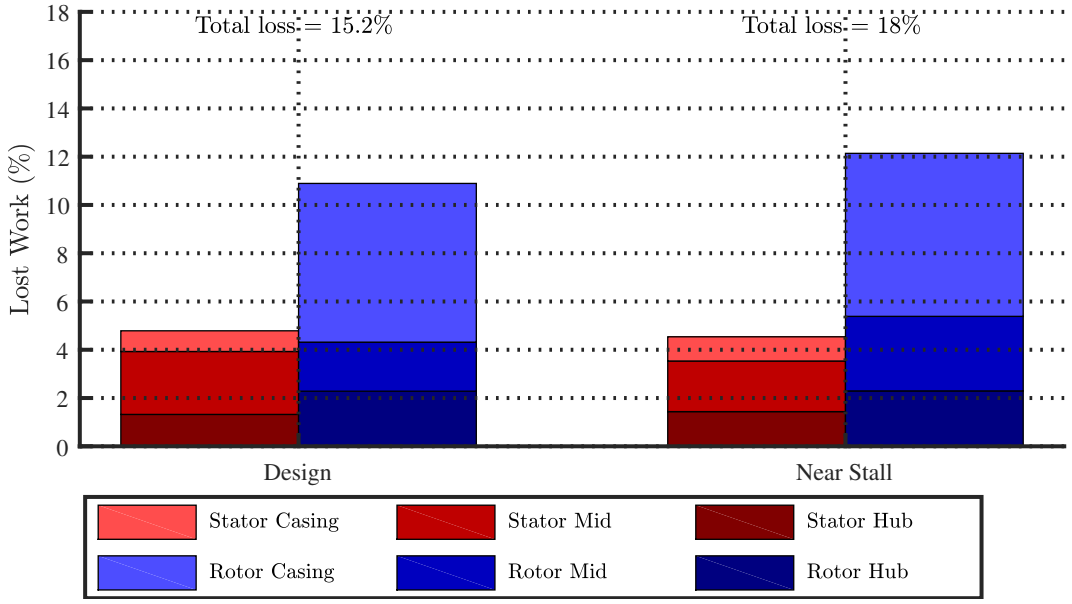

Figure 4.7: Design Re stage loss breakdown at $Design$ and $Near\ Stall$ flow coefficients

4.3.1 Rotor loss analysis

The tip loss is primarily a result of the flow mixing due to the tip vortex, as discussed in Denton [9]. High tip losses are typical in compact compressor stages due to the relatively large tip clearance effects. The midspan loss is comparable with the levels of 2D profile loss calculated by Maffioli et al. [30] for similar blade sections. Figure 4.8 also

shows that the rotor loss increases $Near\ Stall$. The midspan region increase is related to the increase rotor deviation from figure 4.2. The increased deviation increases the exit flow angle thus decreasing turning and pressure rise, as in figure 4.1. Also, the increased deviation indicates that the blade turbulent separation is larger, thus the entropy generation in the shear layer is higher. Both, contribute to an increased stagnation pressure loss.

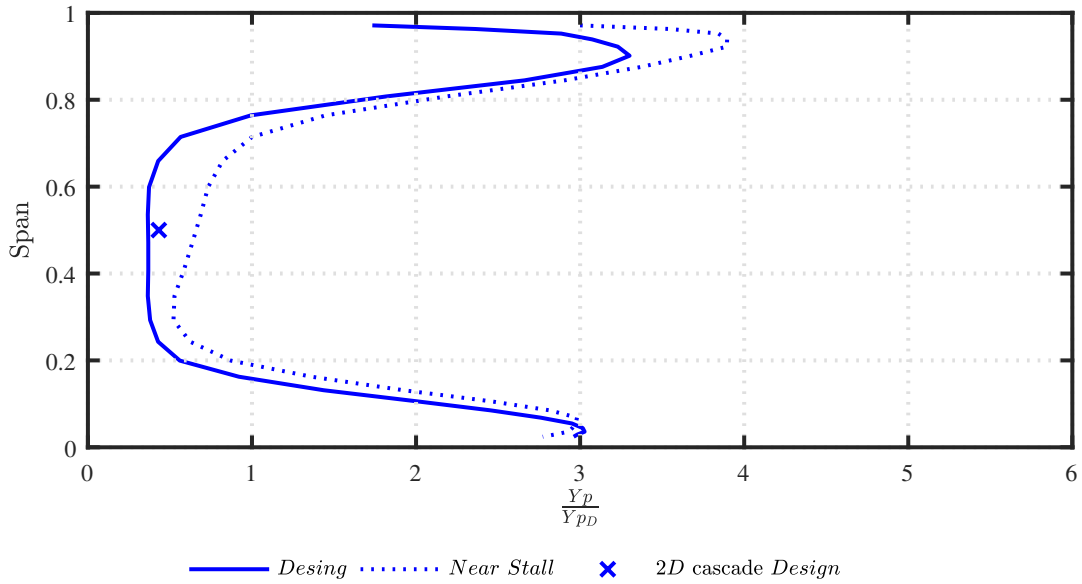

Figure 4.8: Rotor stagnation pressure loss distribution at Re_D for ϕ_D, ϕ_{NS} and from Maffioli et al. [30]

Since the tip gap is $4\%c_t$, which is large compared to traditional high Re axial compressors, the momentum leakage causes a large leakage jet, as discussed in Hewkin Smith et al. [26]. The tangentially flowing jet mixes with the suction side flow causing the flow both to have a low axial velocity and a high flow angle as depicted in figures 4.5 and 4.6.

The mixing of the tangential flow accounts for the high tip region loss, from figure 4.8. At a lower flow coefficient the passage velocity is lower and the boundary layer at the inlet of the rotor tip region is larger. Therefore the tip leakage vortex is stronger, since the flow angle is even higher and thus the mixing loss generated is higher, as discussed in Denton [9].

The 2D profile loss across the midspan is caused by the partly separated suction side. The decrease velocity in the wake of the rotor causes a larger flow angle which accounts for the higher deviation depicted in figure 4.2. At lower ϕ the incidence on the rotor is higher, figure 4.2, thus there is a larger separated region on the suction side. This in turn, increases the amount of low momentum flow, deviation and finally the midspan loss.
The rotor hub loss arises from the suction side corner separation. The boundary layer is separated and there is an open separation between the suction side and the endwall, as in Taylor and Miller [47]. This causes an axial velocity deficit and a high flow angle in the separated region. As the ϕ decreases and the incidence increases, the size of the separation increases, primarily in the spanwise direction.

4.3.2 Stator loss analysis

Looking at the stator stagnation pressure field at $Design$, figure 4.9 (left), the loss is split between the endwall 3D corner separation and the wake 2D profile loss. The midspan suction side turbulent separation is mostly responsible for the midspan loss. Whereas, at the endwalls, mainly the hub region, the incidence is highly positive thus the separation is more likely to be laminar. The laminar endwall separation is more lossy than a turbulent endwall separation as discussed in Maffioli et al. [30]. If a laminar boundary layer separates and does not reattach after transitioning to turbulent, the boundary layer and wake will be very large compared to a turbulent boundary later separating some time after it transitions. The flow would not have been turned to the required angle and the pressure rise would be less, thus the blade would under-perform. Off-design, the stator pressure deficit increases in the wake, but the loss core due to the stator corner separation increases even more. The casing separation becomes much more evident at the lower flow coefficients. This is a consequence of the large positive incidence on the stator endwall regions and the overturning of the low momentum fluid. The effect of suppressing the 3D flow features of the low Re stator is investigated in chapter 6. The stator was chosen instead of the rotor due to the fast prototyping facilities available for experimentally investigating new designs. Future work into the designs could use endwall velocity triangle design by Auchoybur and Miller [1] or compound lean to decrease end wall loading.

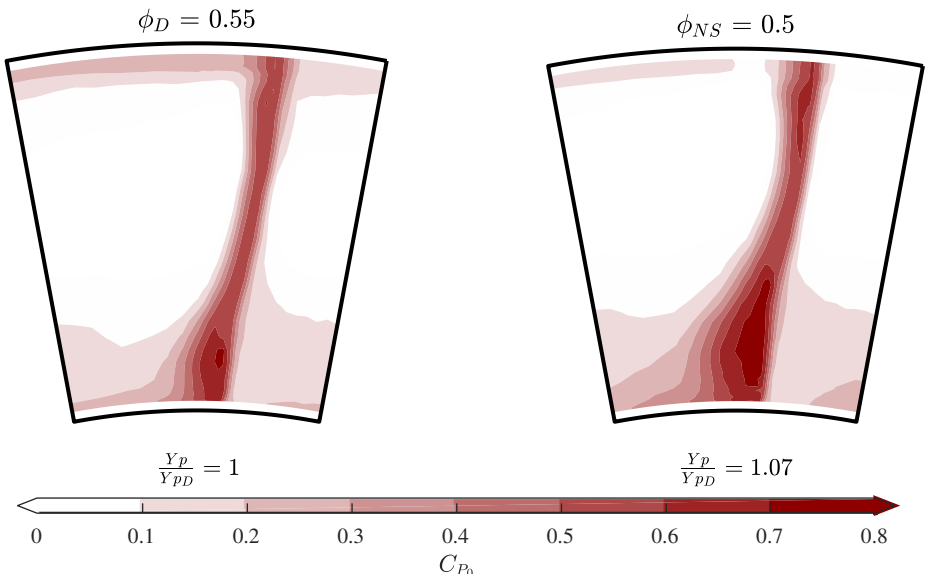

Figure 4.9: Measured stagnation pressure deficit across the stator at Re_D at $Design$ and $Near\ Stall$

4.4 Rotor post stall performance

Rotor exit hot-wire traverses were also conducted at a lower flow coefficient to evaluate the loss profile. The flow coefficient is referred to as $Post\ Stall$ and its value was $\phi_{PS} = 0.475$, see figures from 4.11 to 4.13. The increase of rotor tip region velocity deficit and flow angle at $Post\ Stall$ is higher than that at $Near\ Stall$.

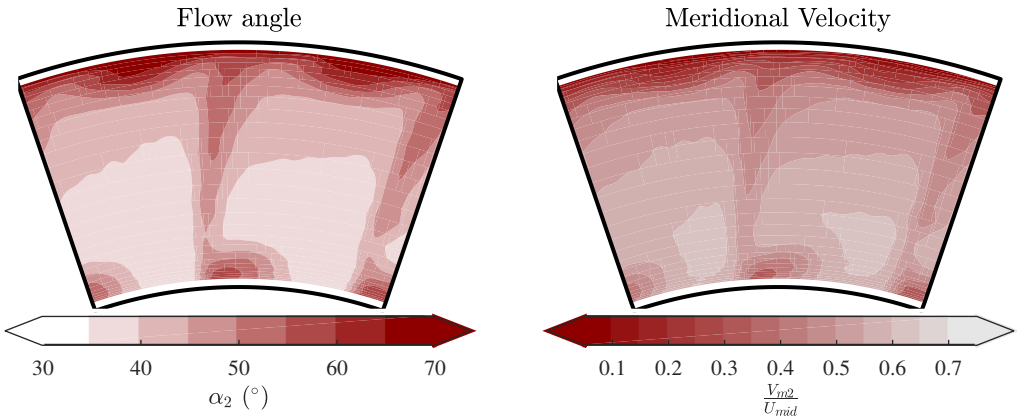

Figure 4.10: Flow angle and velocity contours at the rotor exit at $Post\ Stall$ (hot-wire)

Figure 4.11(left) indicates that the velocity deficit near the tip is 3 times larger at $Post\ Stall$. This deficit arises from the tip leakage core, the wake of the tip region of the blade and casing region of mid-passage, from figure 4.10(left).

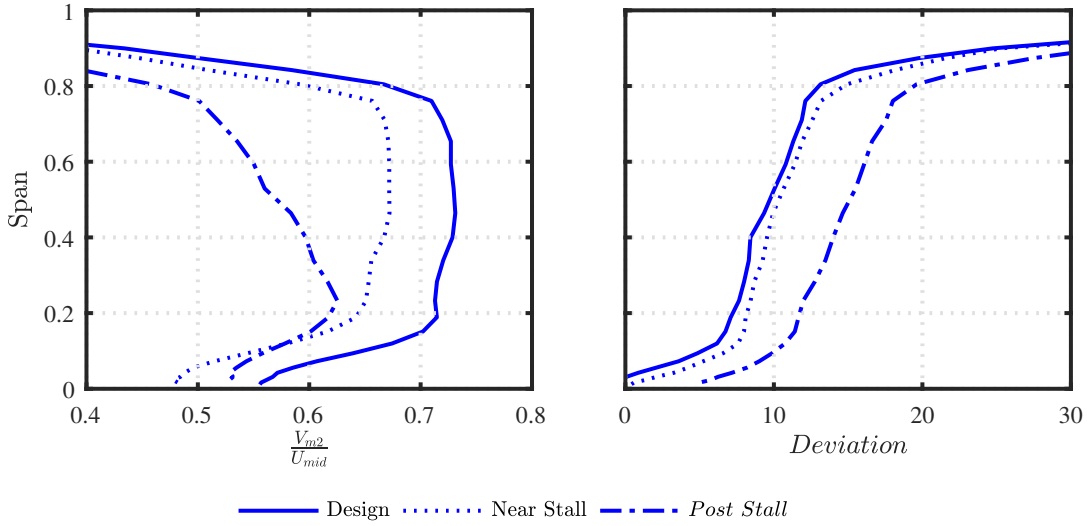

Figure 4.11: Spanwise distribution of non-dimensionalised meridional velocity and deviation at the rotor exit for $Design$, $Near\ Stall$ and $Post\ Stall$ (hot-wire)

The core starts to blend in with the rotor wake at 5% span and at 10% span the wake dis similar to NS, see figure 4.12. In the midspan and higher region the wake increases and starts to blend with the mid-passage flow showing a shift in the loss profile, see figure 4.13.

Also, comparing the distribution of the deficit along the span of the blade, see figure 4.11, the maximum deficit region switched from the hub region, at $Near\ Stall$, to the tip region, at $Post\ Stall$. This is an indication that the rotor tip region has at a part span stall cell causing the compressor to stall and loose performance, as discussed in Day [8].

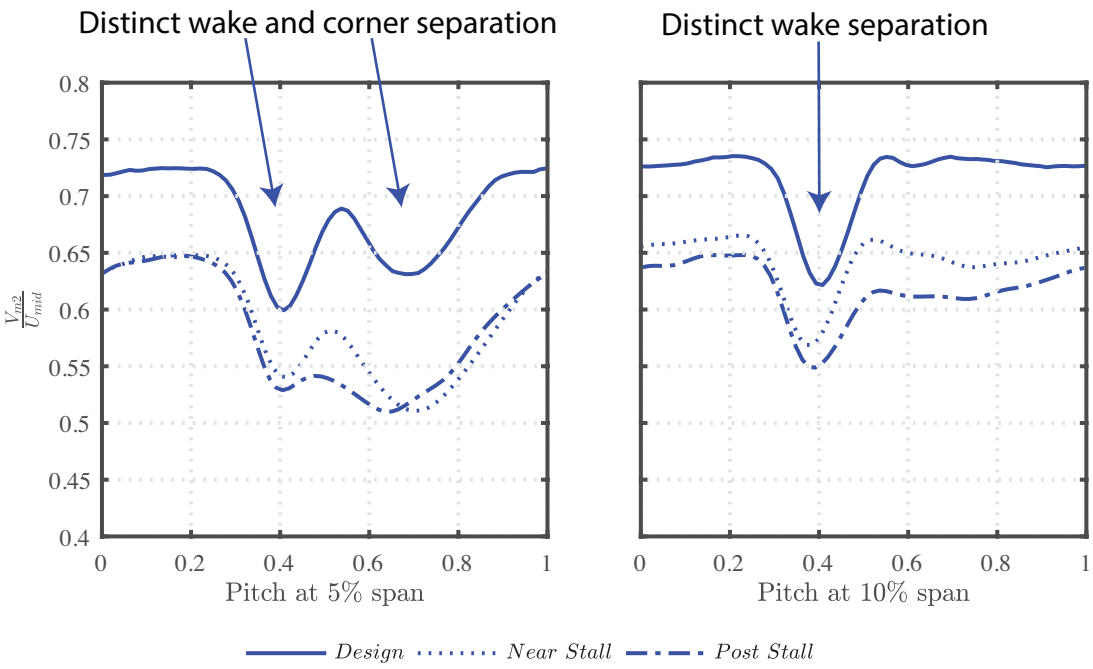

Figure 4.12: Pitchwise meridional velocity at rotor exit, hub region (hot-wire)

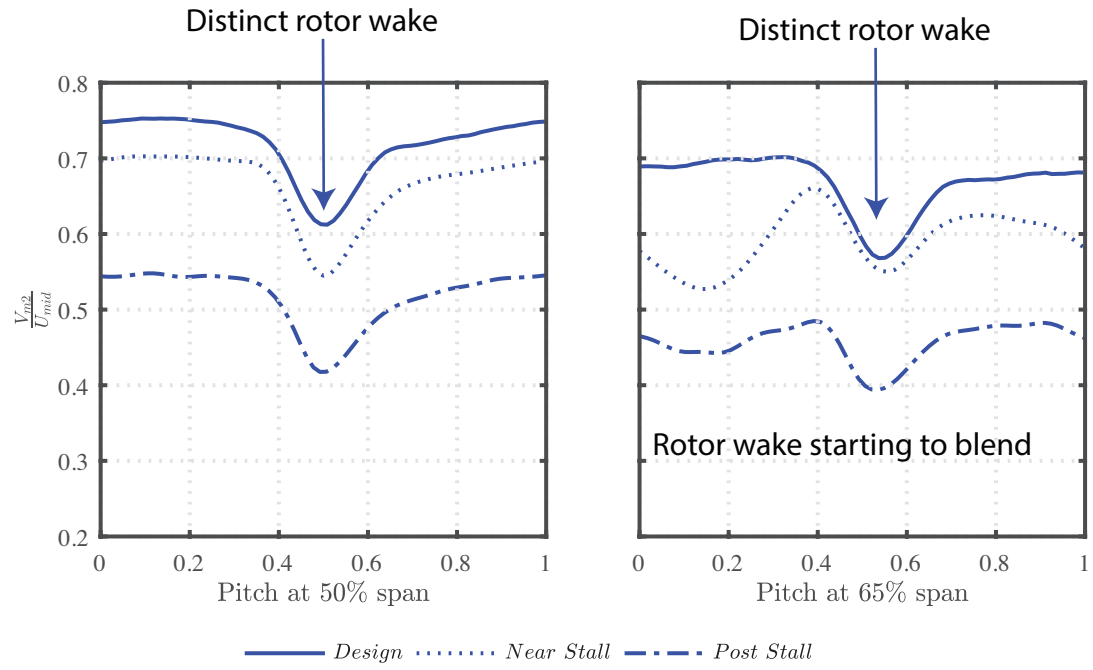

Figure 4.13: Pitchwise meridional velocity at rotor exit, midspan region (hot-wire)

4.5 CFD capabilities and limitations

In this section, the capabilities and limitations of using steady fully turbulent RANS CFD (with the Spalart Allmaras turbulence model) as a design tool for Low Re, with transition flow compressors are investigated.

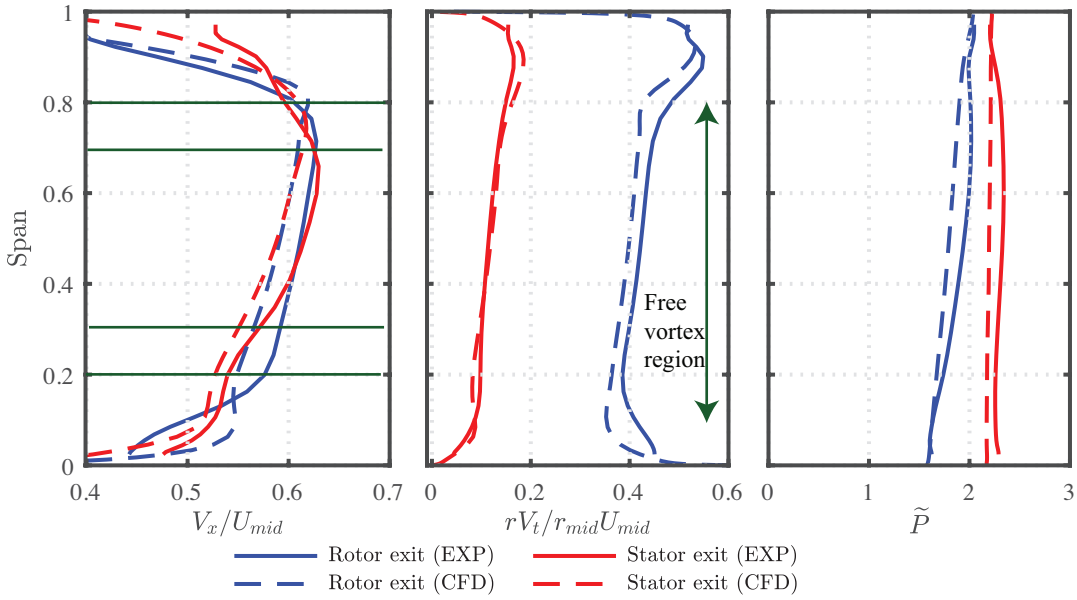

Figure 4.14: Spanwise, pitch-averaged, distribution of non-dimensional axial velocity, angular momentum and static pressure at Re_D and ϕ_D

As shown in figure 4.14, at Re_D and ϕ_D the angular momentum and static pressure distributions are captured well by CFD. However, in the axial velocity plots, the flow in the hub and tip regions lead to significant differences between the CFD and experiment. The CFD calculated boundary layer exiting the rotor is four times smaller than that of the experimental measurements. Whereas, at the stator exit it is 50% larger, indicating there is more transition flow in the rotor hub than the stator hub causing this mismatch. The reason CFD rotor exit hub region mismatches the experiments is because the CFD does not capture the rotor endwall corner separation present in figure 4.6 but not in figure 4.15. On the other hand the wake increase in width and depth is captured.
The stator loss distribution is poorly captured at off-design conditions, see figure 4.9 compared with figure 4.16. The stator corner separation is larger in CFD than the

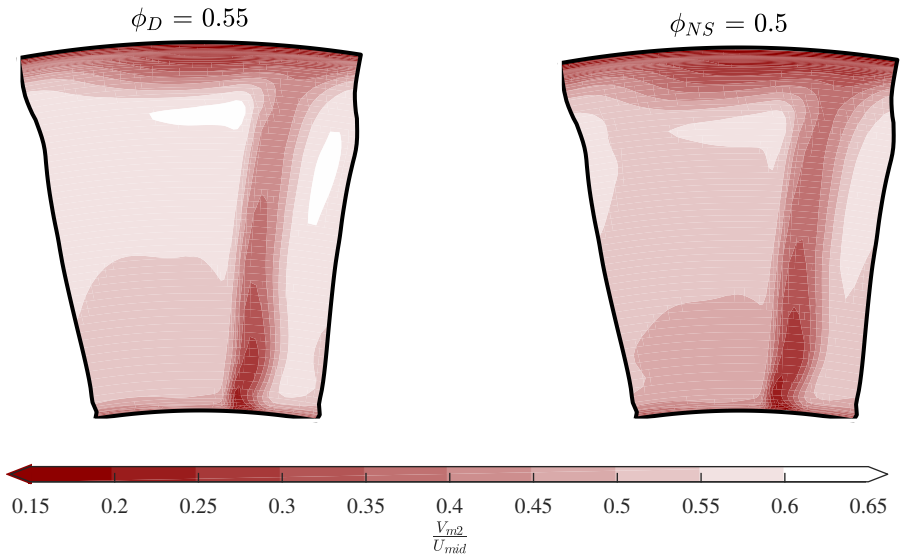

Figure 4.15: Computed rotor exit non-dimensional meridional velocity at Re_D

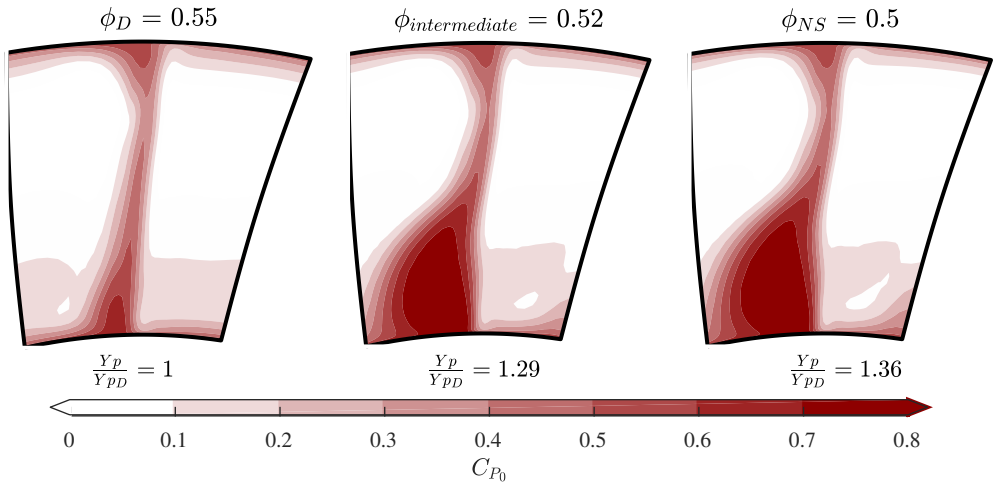

Figure 4.16: Computed stator exit stagnation pressure at Re_D

experiments towards stall, and the separation extends across most of the passage. Taylor and Miller [47] also came across this large corner separation at high Re. This is a consequence of the high sensitivity of the CFD on the stator inlet incidence angle. Therefore, this mismatch is not a consequence of the low Re.
Despite the endwall flow dissimilarity, the midspan performance at design Re and flow coefficient can be used by designers looking to make blade alterations.

4.6 Summary

For the first time, the flow of a low Re axial compressor has been experimentally investigated in detail. In this chapter, focusing on a $Re = 6 \times 10^4$, the rotor hot-wire and stator 5-hole probe traverses show that the flow field at low Re is similar to that would be expected at high Re. The compressor blades are not completely separated and behave close to design intent. For the rotor most of the loss is concentrated in the casing region, whereas for the stator the loss is split between the endwalls and the midspan. At lower flow coefficients the rotor midspan and casing loss increase more than the hub region. However, for the stator, the loss increases more in the hub region due to a 3D separation.
Steady fully turbulent RANS CFD can capture the overall spanwise variations in pressure and velocity, but not the endwall flow or the loss levels. The absence of transition modelling causes an under estimate of the rotor exit boundary layer displacement thickness by approximately 4 times.
The stator hub endwall flow is sensitive to the inlet incidence angle at low Re, similar to what was observed in the literature at high Re, making it hard to optimise the design in that region. At low Re, CFD should be used with caution for guiding the design, and for more accurate predictions, transition modelling and alternative turbulence models are needed.

Chapter 5

Reynolds Number Effects on Axial Compressor Flow Field

The previous chapter focused on the compressor stage flow features and their impact on performance at design Re. This chapter aims to explore the effect Re has on the flow features and quantify their impact for both $Design$ and $Near\ Stall$ flow coefficients. Higher and lower Re were investigated and the development of the loss breakdown was quantified for $Re = 10^4$ to $Re = 10^5$. Finally distinguishing the capabilities and limitations of industry standard fully turbulent RANS, were investigated for this range of low Re.

5.1 Rotor and stator flow features

The Re of the compressor was set by changing the rotational speed of the rig. Then, the ϕ at rotor inlet was set by moving the exit throttle position. The rotor inlet was then traversed to verify that the flow coefficient and incidence angle distribution along the span was the same at all Re, see figure 5.1(left).
A decrease in Re while keeping the rotor incidence angle, and flow coefficient, constant corresponds to a decrease in the speed of the flow over the blade surface, as discussed in Schlichting [40]. The boundary layer will remain laminar for a longer

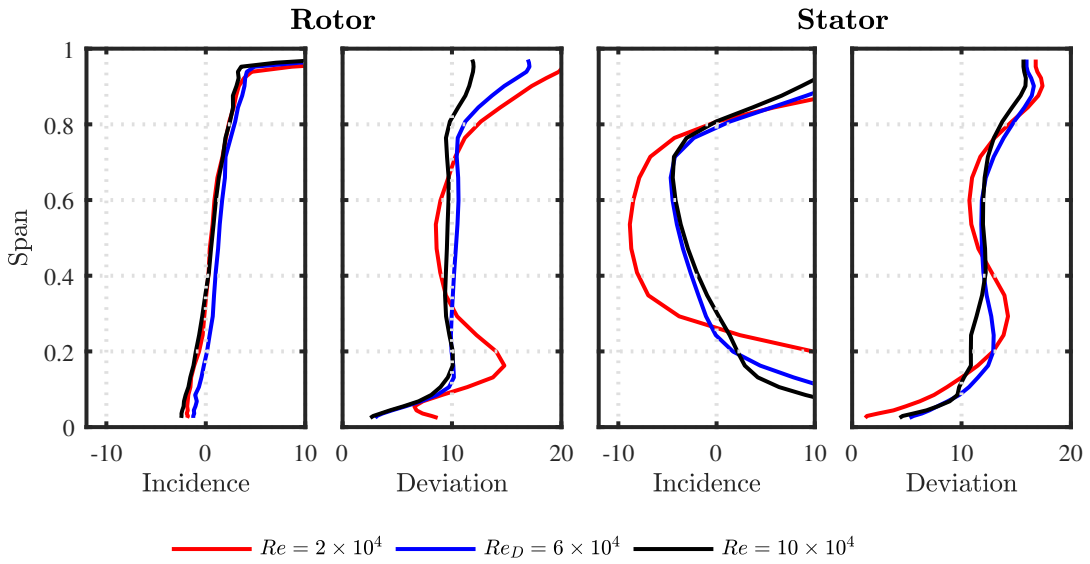

Figure 5.1: Measured spanwise distribution of incidence and deviation at ϕ_D

portion of the blade surface and thicken up. Hence, once the lower momentum boundary layer separates, due to the adverse pressure gradient on the blade suction side, it will either reattach further down the surface or not reattach at all. Therefore for the same flow coefficient a wider wake and higher deviation is expected. Even though the incidence at all Re is the same up the span, the velocity and chord is lower going up the span therefore the upper half of the span is more prone to separate and not reattach than the rest of the blade.

Increasing Re from 6×10^4 to 10×10^4 decreases the rotor midspan deviation angle by $2°$, as seen in figure 5.1. When the Re is decreased to 2×10^4, the midspan deviation decreases as well by $2°$, whereas the deviation at the hub region increases by about $4°$. At the higher Re the boundary layer has higher momentum and stays attached longer on the rotor suction side, hence decreasing the deviation. At the lower Re the deviation was expected to increase in the midspan, as discussed above. Therefore, there is a secondary flow feature at the endwalls causing this decrease in deviation.

As the rotor deviation increases the stator incidence increases, see figure 5.1. The stator incidence angle increase is higher at the endwalls. Despite the fact that the incidence at the endwalls is greater than $10°$ the stator manages to keep the deviation increase to approximately $4°$. Therefore the stator is not very sensitive to inlet changes.

Further investigation was carried on redesigning the stator to decrease its sensitivity and increasing its performance in chapter 6.
Since there is no major flow difference between Re_D and the higher Re, emphasis is given to the flow at Re lower than 6×10^4 and the following sections look into them in more depth.

5.1.1 Rotor flow features

Figures 5.2 and 5.3, show the absolute exit flow angle and meridional velocity at the exit of the rotor at two different Re and two different flow coefficients. Hot-wire traverses were used to calculate the data.
At $Design$, a decrease in Re, causes the hub endwall corner separation and tip vortex core to increase. The midspan wake no longer has a uniform width along the span. The width decreases at the lower midspan region and increases at the region close to the tip. The tip region wake and tip leakage vortex are distinguishable from one another. The shorter chord at the tip region makes the local Re to be smaller than the rest of the blade, making it prone to larger separations. It is possible that the laminar separation bubble has not reattached causing this large wake at the exit of the rotor.
At $Near\ Stall$ and at a decreased Re, the hub separation is larger than all other cases in figures 5.2 and 5.3. The tip leakage vortex and the tip region wake are no longer distinct features. The large regions of velocity deficit in the tip and hub region, see figure 5.3, cause a flow redistribution which increases the velocities in the midspan region.

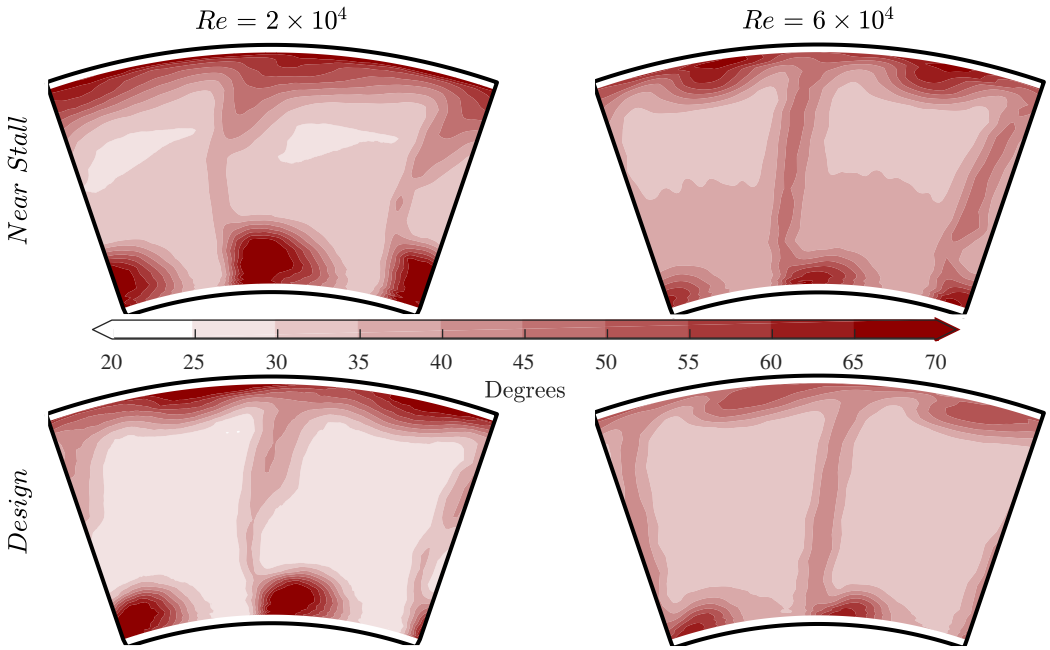

Figure 5.2: Hot-wire absolute flow angle measurements at rotor exit (hot-wire)

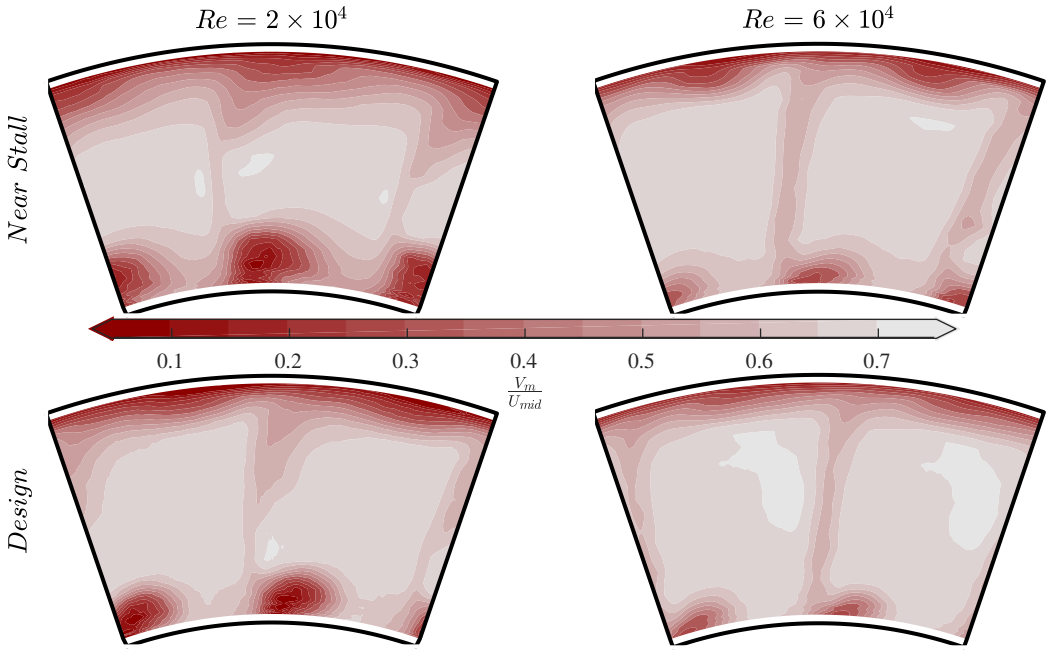

Figure 5.3: Hot-wire meridional velocity measurements at rotor exit (hot-wire)

5.2 Rotor and stator loss breakdown

The loss across the stage was divided into hub, midspan and casing regions at a mass flow ratio of $1:2:1$ for the range of Re investigated using equations 3.12 and 3.13. Figure 5.4 shows the loss breakdown for $Re = 2 \times 10^4$ and $Re = 6 \times 10^4$.
The stator and rotor loss increases by 20% and 50%, respectively, with a decrease in Re. The stator loss increase is shared between the casing, 65% increase, and midspan regions, 30% increase.
The rotor loss increase is across all three regions, with the largest increase in the rotor hub. The hub loss is 2.5 times larger at $Re = 2 \times 10^4$ compared to $Re = 6 \times 10^4$. Whereas the midspan loss increases by 50% and the casing loss by 20%.

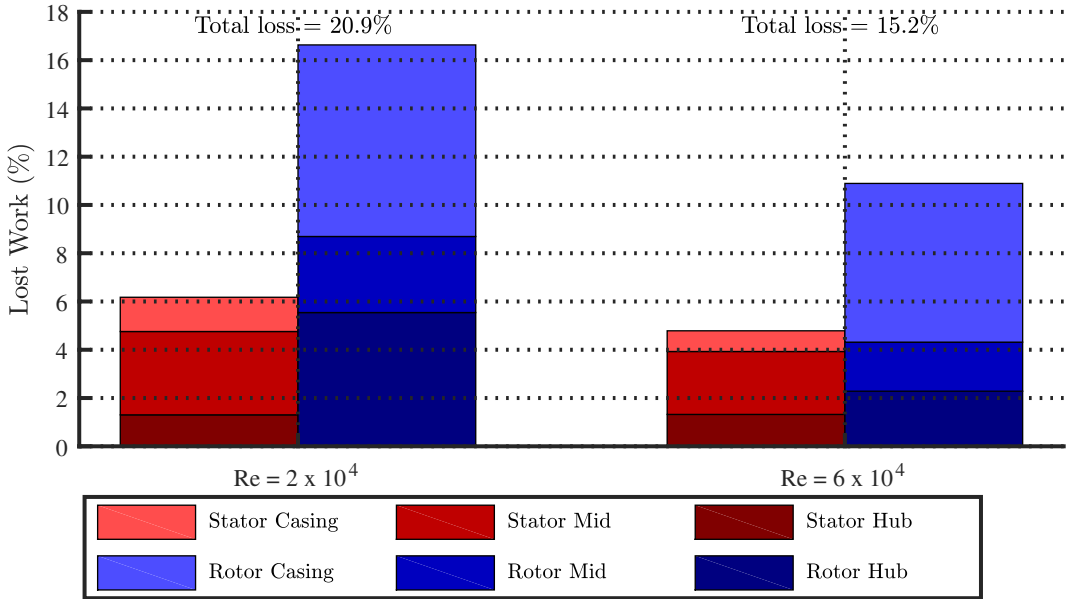

Figure 5.4: Stage loss breakdown across Re

5.2.1 Rotor loss analysis

The behaviour of the rotor spanwise velocity distribution, at $Re = 2 \times 10^4$, with respect to decreasing the flow coefficient is different than that of the design Re, see figure 5.5. At design flow coefficient the hub corner separation extends to twice the span, from 10% to 20%, with 10% higher velocity deficit.

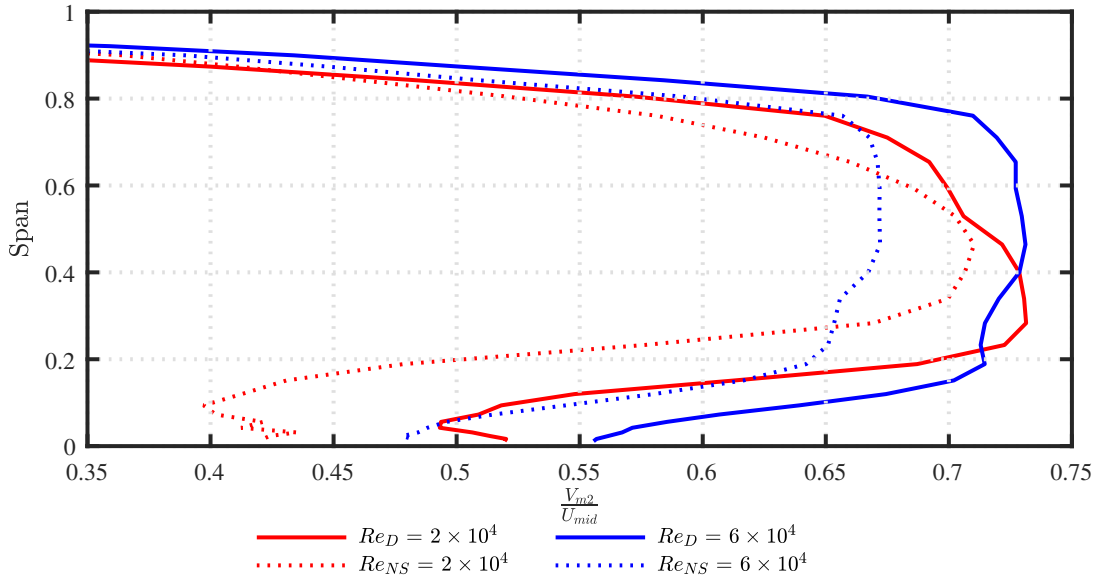

Figure 5.5: Spanwise meridional velocity at the rotor exit (hot-wire)

The midspan region has a reverse distribution between the two Re, the lower Re has higher velocity near the hub whereas the higher Re has lower velocity near the hub. The lower Re endwall flow features cause a large blockage and flow gets redistributed towards the lower part of the midspan, increasing the velocity and decreasing the deviation and loss in that region.

The blade wake and hub corner separation are two distinct features at $Design$, see figure 5.6. The size of the the corner separation at $Re = 2 \times 10^4$ is large both in the pitchwise direction and spanwise direction. At the 40% span region the wake is slightly wider and deeper at the lower Re, see figure 5.7 At 50% span the width and depth starts increasing, showing an increase in the separation.

At $Near\ Stall$ the velocity distribution at Re_D decreases uniformly by approximately 10%, whereas at the lower Re the endwall velocity decreases by 20% and the midspan by 5%. Both the rotor tip region separated flow and the hub corner separation increased in size pushing more flow towards the midspan. From the pitchwise distribution, figure 5.6, at Re_D the hub region wake and corner separation start blending with each-other and at the lower Re the corner increases to 50% of the span making the wake indistinguishable. Whereas at the 40% span there is almost no change and at the 50% span a small increase in the depth of the velocity deficit.

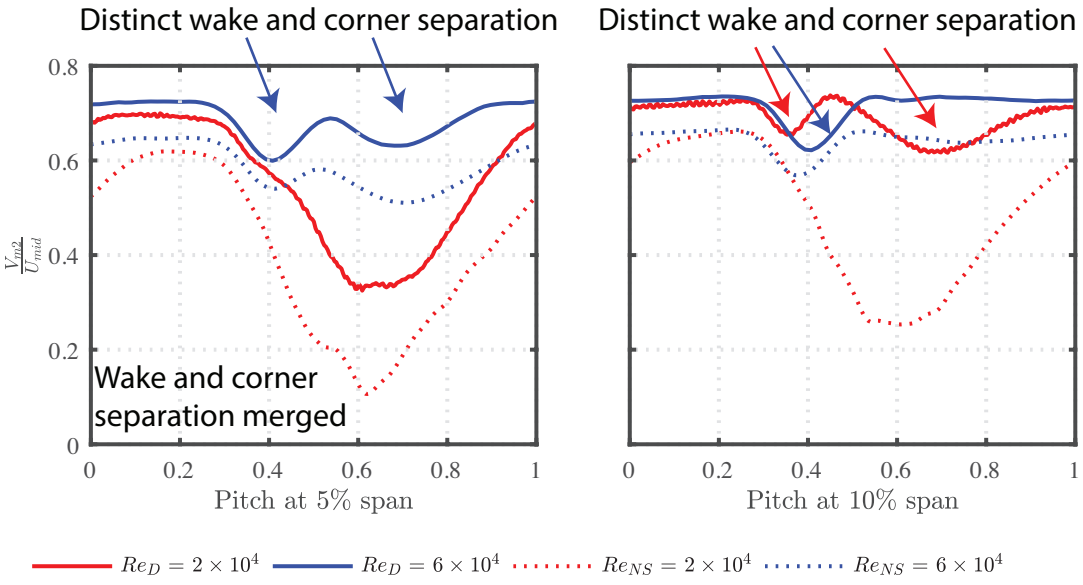

Figure 5.6: Pitchwise meridional velocity at the rotor exit (hot-wire)

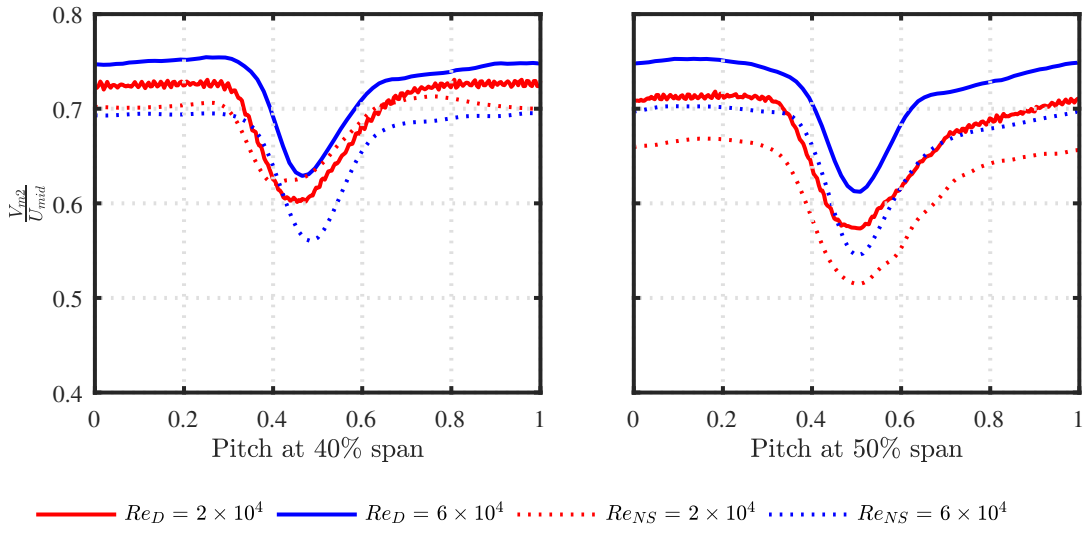

Figure 5.7: Pitchwise meridional velocity at the rotor exit (hot-wire)

The low Re velocity deficit distribution increases a small amount at the lower flow coefficient. On the other hand, the mid to tip region of Re_D decreases by 20% indicating a tip region stall. The low Re case could already be stalled, in the tip region, even at design and as the flow coefficient is decrease the stall cell increases to a bigger part of the span.

5.2.2 Stator loss analysis

The stator loss increases at lower Re. The increase is primarily concentrated at the endwalls, as in figure 5.8. The highly positive stator hub region incidence at the low Re, causes a higher stator corner separation and the core is further away from the hub. As seen from figure 5.4 the increase in the hub corner separation does not increase the hub region loss. It its likely that the loss associated with that region has translated in the midspan region.

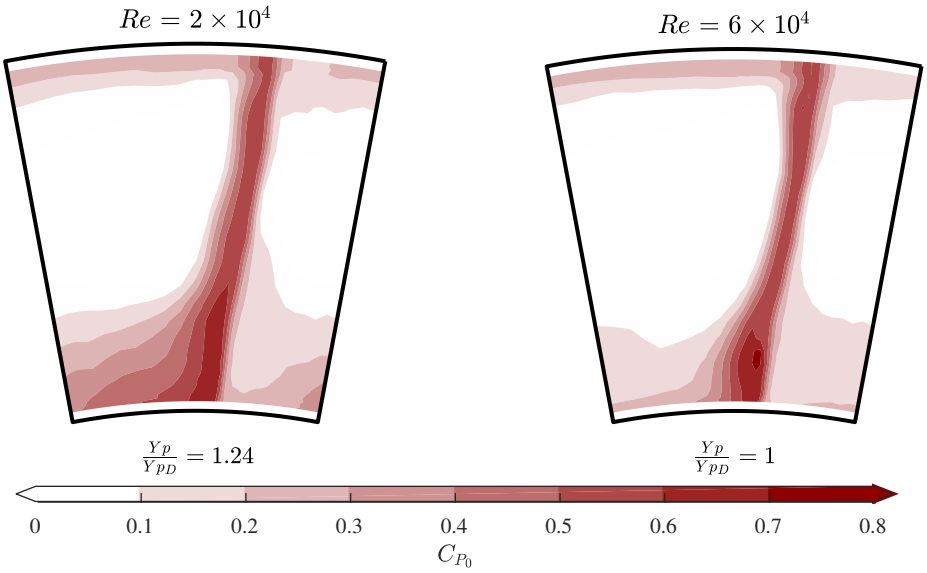

Figure 5.8: Measured stagnation pressure deficit across the stator at 2 different Re

5.3 Loss across Reynolds number

Decreasing the Reynolds number in experiments, increases the total loss in both the rotor and stator see figure 5.9. In general, the loss in the rotor is higher than the stator loss, see figure 5.10. The loss in the rotor increases at a greater rate at low Re than loss in the stator. This is due to the growth of the rotor hub and casing flow features. From figures 5.10 and 5.11 it is evident that the rotor 3D losses dominate the 2D losses. The "critical Re" at which the rotor loss starts to increase at an exponential rate is around $Re = 4 \times 10^4$.

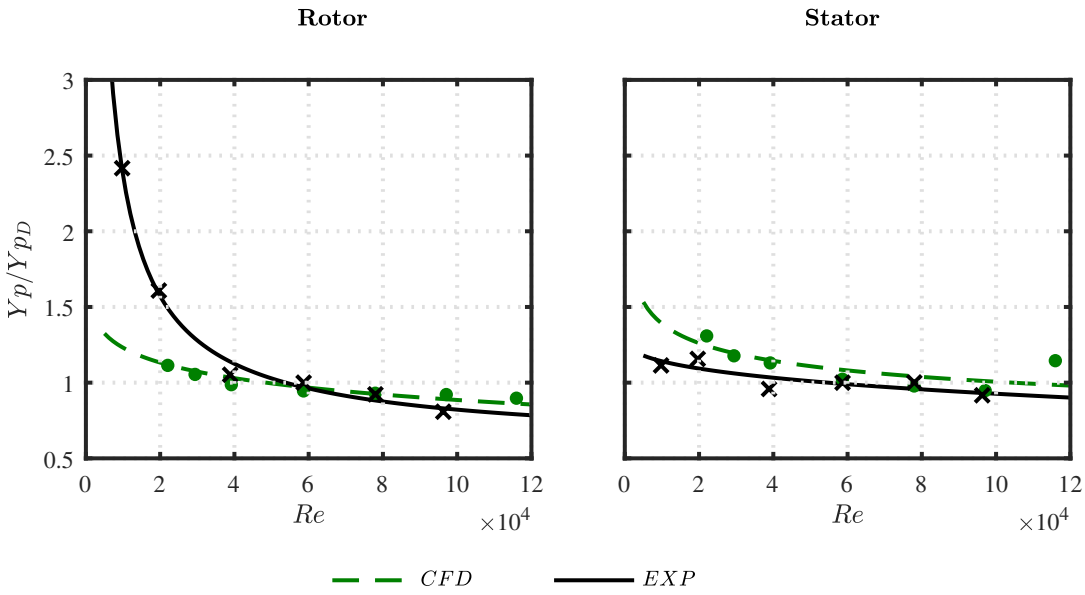

Figure 5.9: Measured and computed variation of blade row stagnation pressure loss with Re

The stagnation pressure loss along the span of the rotor for three different Re is plotted in figure 5.11. Increasing the Re from design, the midspan and hub region losses decrease, by approximately 30%, while the tip region loss stays unchanged. Decreasing the Re, increases the loss across the whole row apart from a small region near 45% span. The loss in the tip region increases by approximately 50%, whereas the hub loss increases by more than 100%.

This is caused by the mass flow redistribution due to the hub and tip region flow features visible in figure 5.3. The higher velocity near the 40% span region, having a

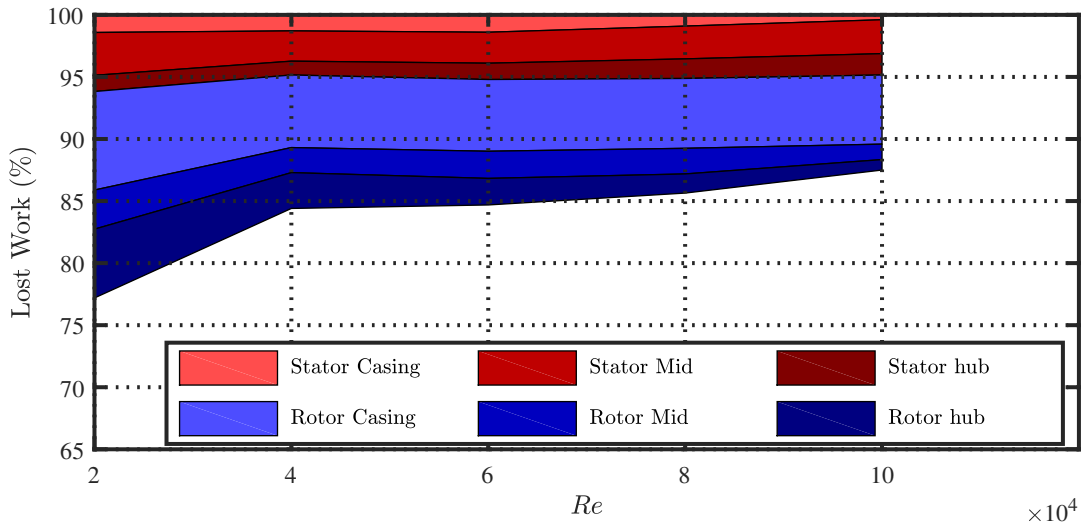

Figure 5.10: Stage loss breakdown across Re

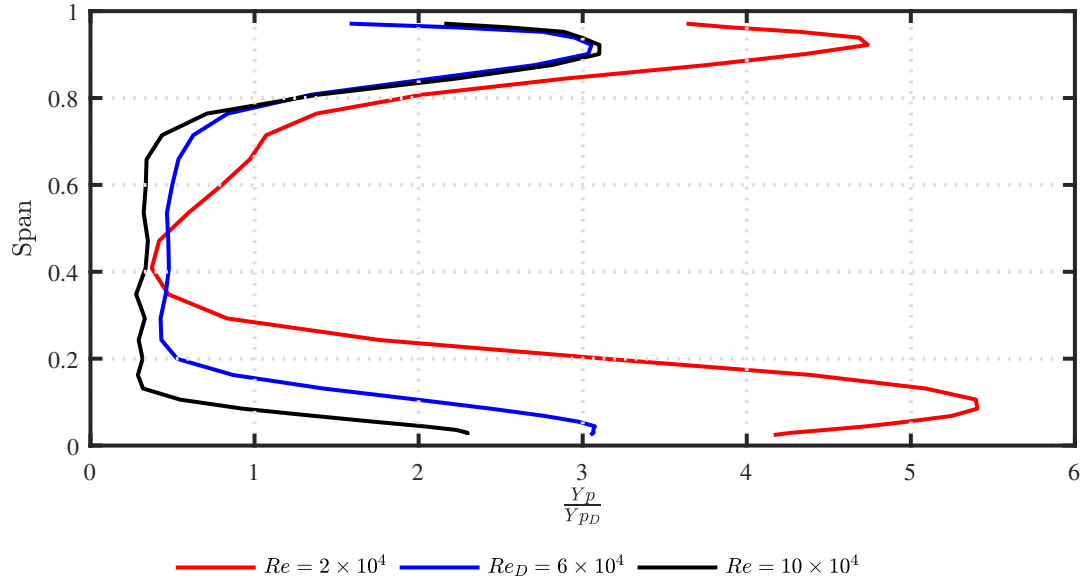

Figure 5.11: Y_p distribution at ϕ_D for 3 different Re

larger local Re, allows the flow to stay attached for longer and decrease the deviation, see figure 5.1,and thus the pressure loss in that region of the span.

5.4 Rotor post stall performance

Figures 5.12 to 5.14 show the effect on the rotor flow $Post\ Stall$ behaviour at two different Re.

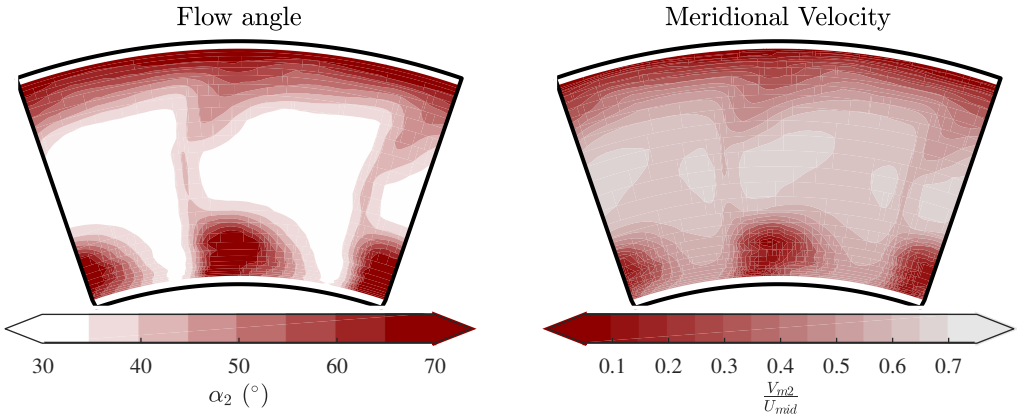

Figure 5.12: Contours at the rotor exit at $Re = 2 \times 10^4$ and $Post\ Stall$ (hot-wire)

In section 4.4, it was indicated that, at design Re, the rotor suction side tip region separation was the cause of the stage stall. Section 5.1.1 and figure 5.12 , show that the same tip region separation exists at all investigated flow coefficients at $Re = 2 \times 10^4$. The rotor is believed to be in a part span stall state, therefore the flow field does not change significantly with ϕ, at $Post\ Stall$.

At the lower Re the mass flow redistribution caused by the endwall flow causes the midspan velocity to decrease by only 5% compared to the design Re which decreased by 15%, see figure 5.13. The wake depth of the midspan region barely changes at the lower Re compared to the design Re, see figure 5.14. The depth at design Re increases by approximately 15%, whereas the wake at the lower Re it increases by less than 5%.

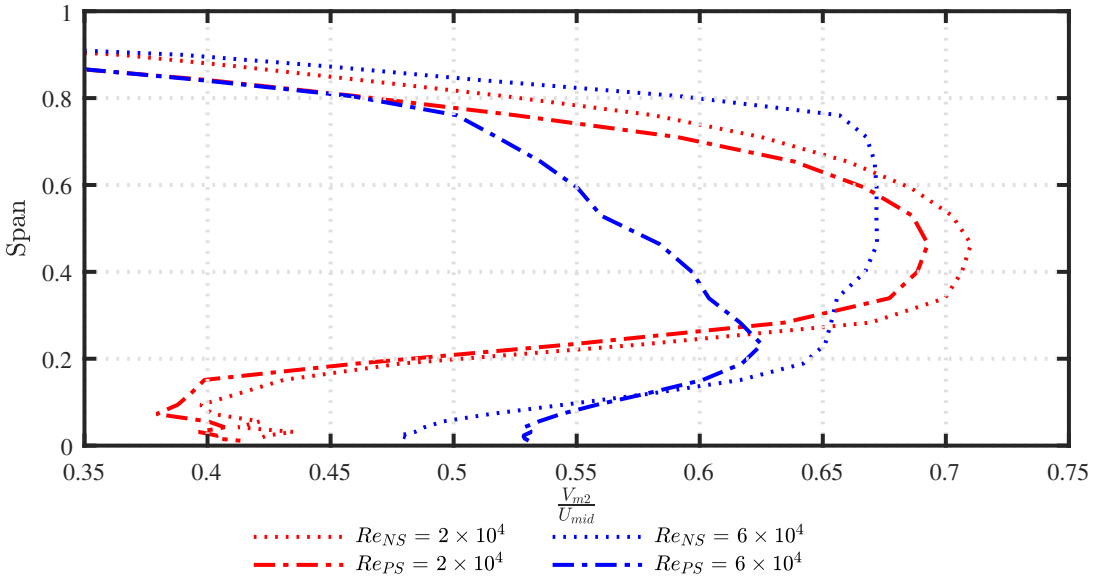

Figure 5.13: Spanwise meridional velocity at the rotor exit (hot-wire)

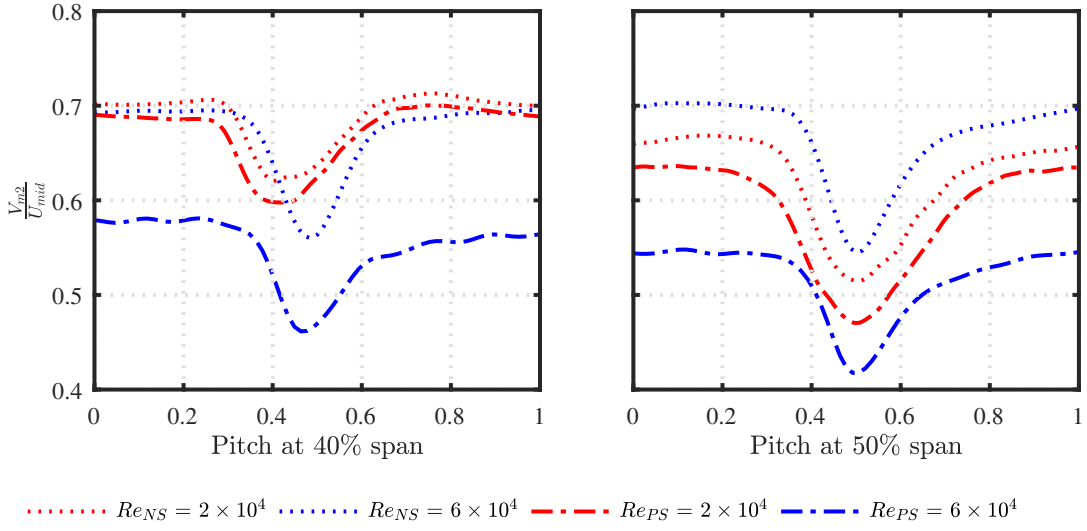

Figure 5.14: Pitchwise meridional velocity at the rotor exit (hot-wire)

5.5 CFD limitations

At $Re = 2 \times 10^4$, as shown in figure 5.15 the CFD cannot capture the rotor exit hub velocity deficit caused by the corner separation, present in figure 5.3 but not in figure 5.16. As discussed previously, the rotor hub flow is transitional as well as 3D, thus this CFD with fully turbulent flow cannot predict its effect. The mass flow redistribution present in the experiments is therefore not present in the CFD. Thus the stator incident flow is different.

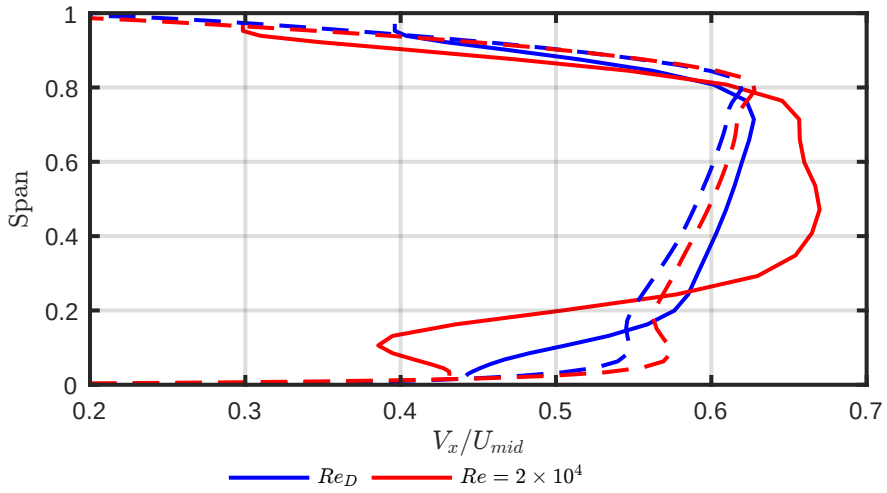

Figure 5.15: Measured (solid) and Computed (dashed) spanwise rotor exit axial velocity distribution at ϕ_D for Re_D and $Re = 2 \times 10^4$

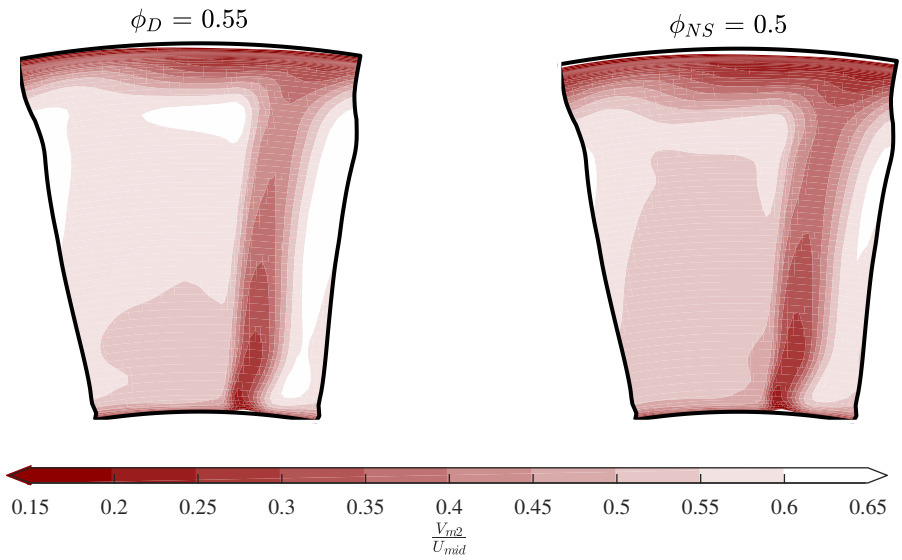

Figure 5.16: Computed rotor exit non-dimensional meridional velocity at $Re = 2 \times 10^4$

5.6 Summary

At $Re < 4 \times 10^4$, for the compressor stage investigated, there is a large corner separation in the hub region of the rotor. This is not predicted in the CFD. Measured loss coefficients in the rotor endwall regions were found to almost double from $Re = 6 \times 10^4$ to $Re = 2 \times 10^4$.

Over the range of Re investigated the 2D profile loss increases as discussed in chapter 2. The "Critical Re" at which the losses increase at a higher rate is closer to 4×10^4 rather than 10×10^4 which was expected from Rhoden [36]. This was because, once the stage cross-sections were tailored to suppress the suction side separation that occurs at low Re, the "Critical Re" was shifted to a lower number.

Surprisingly, the stator is far less sensitive to Re. The size of the stator hub loss core remains remarkably fixed.This presents an opportunity for the designer. Due to the stator loss insensitivity to Re there is the potential to use standard 3D design methods to reduce the hub endwall separation.

First, loss could be reduced by better matching of the spanwise distribution of the stator inlet angle to the measured absolute flow angle delivered by the rotor. In addition, compound lean could be applied to reduce loading at the hub and casing. The effect of compound lean and stator leading edge re-cambering is investigated in the next chapter.

Chapter 6

Effect of Design Changes on Stator Flow Field

As shown in Chapters 4 and 5, a loss concentration was found at the stator endwall region which increases at lower ϕ, see figure 4.9 and at lower Re, see figure 5.8. This loss is primarily influenced by the highly positive stator incidence angles, that increase at lower ϕ and Re, at the endwall regions causing the corner separation to increase, see figures 4.2 and 5.1.
Firstly, the stator endwall leading edge re-cambering was introduced to decrease the endwall incidence and subsequently the loss in the endwall regions. Secondly, compound lean was introduced on the stator stacking line, to investigate whether low Re flow can be redistributed in the same manner as in high Re compressors.

6.1 Leading edge re-cambering

Stator endwall leading edge re-cambering was introduced to decrease the rotor endwall incidence, as in Gallimore et al. [16], and suppress the stator endwall losses. Using the knowledge of the rotor exit flow angle, from experiments (see figure 6.1a), the stator inlet angle can be respecified to be better matched to the spanwise variation of rotor exit flow at design.

The computed flow angles near the endwalls are lower than the measured ones. The mismatch can be explained by the absence of any transition in the CFD calculated flow. In the experimental flow the endwall boundary layers would have transitioned to turbulent via a laminar separation bubble, where the reattached flow would have a thicker boundary layer compared to the CFD fully turbulent boundary layer. One way of tackling this difference would be the modification of the turbulence generation factor in the "Spalart-Allmaras" turbulence model. An increase in the turbulence generation factor would then cause the computed boundary layers to develop faster and thus making it possible to match their width to the experimentally measured boundary layers.
The experimental rotor exit flow angles were used as the basis for the redesigns in this section. The Matlab scripts generating the stator geometry used 5 inlet and exit flow angles equally spaced along the span and interpolated onto 21 cross-sections. The exit metal angles were kept at $0°$, and 4 different inlet angle distributions were implemented, see figure 6.1b. The 4 different stators were then simulated in Turbostream as described in section 3.3.

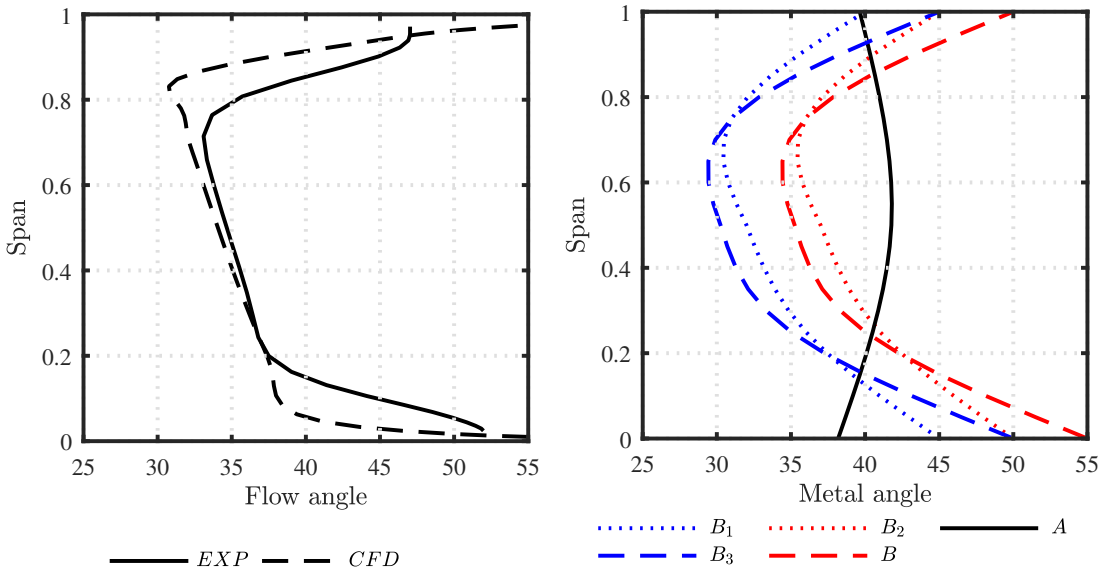

(a) Stator inlet flow angle at $Design$

(b) Stator inlet metal angle distributions

Figure 6.1: Stator leading edge re-cambering

Cases B_1 and B_3 aimed at a similar incidence angle, with each other, at the midspan region, with case B_3 attempting to decrease the endwall incidence by another $5°$. Cases

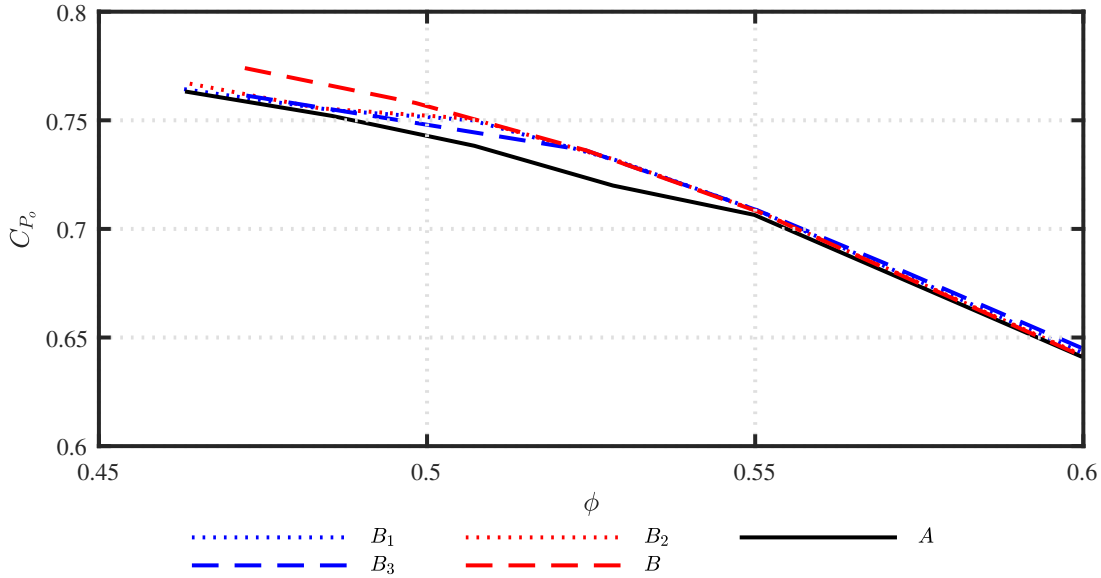

Figure 6.2: Effect of stator design on stage stagnation pressure rise

B_2 and B aimed to decrease the overall incidence angle distribution by $5°$ from cases B_1 and B_3 respectively, in an effort to increase range and performance at lower ϕ. All cases were simulated at a range of ϕ. The fully converged (see subsection 3.3.3) pressure rise characteristics are presented in figure 6.2.

6.1.1 CFD study of stator designs

The stage efficiency of all 4 cases has increased from that of the datum stator, stator A, as shown in figure 6.3(right). The stage efficiency increase is higher at $Near\ Stall$ than that at $Design$, with stator B near stall efficiency being the highest. This supports the intent of stator B which is to increase performance both at $Design$ and at $Near\ Stall$.

The rotor efficiency, figure 6.3(left), barely changed as expected. Looking at the individual blade row loss, see figure 6.4, it is clear that the rotor loss is not affected by the stator redesign, where as the stator loss is decreased. The loss decrease is higher near stall for stators B_2 and B.

The intended effect of the 4 designs on the incidence was achieved as described in section 6.1, and is visible in figure 6.5. Even though the incidence angle distribution

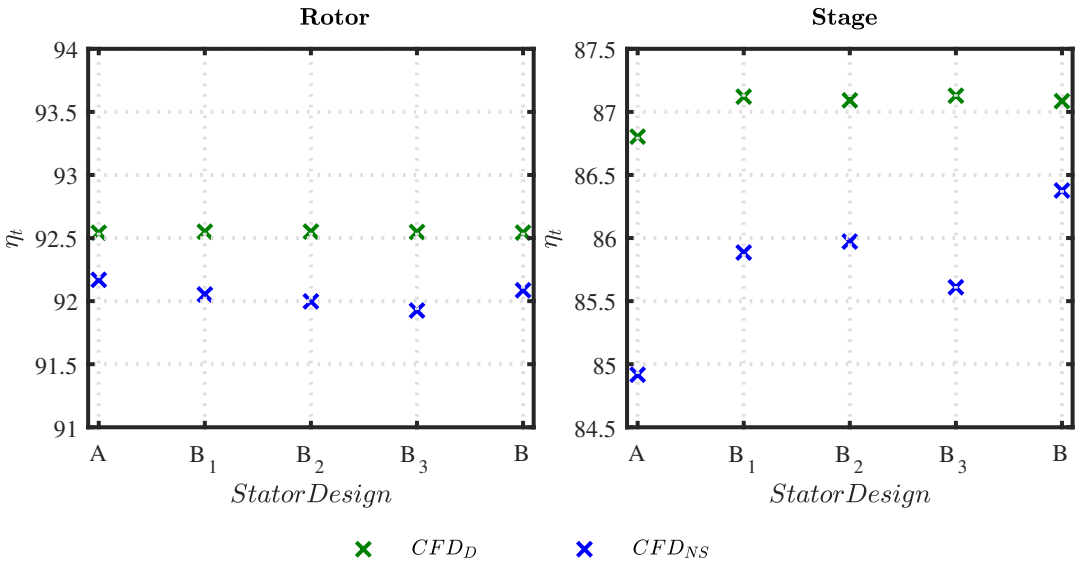

Figure 6.3: The effect of stator design on rotor and stage efficiency

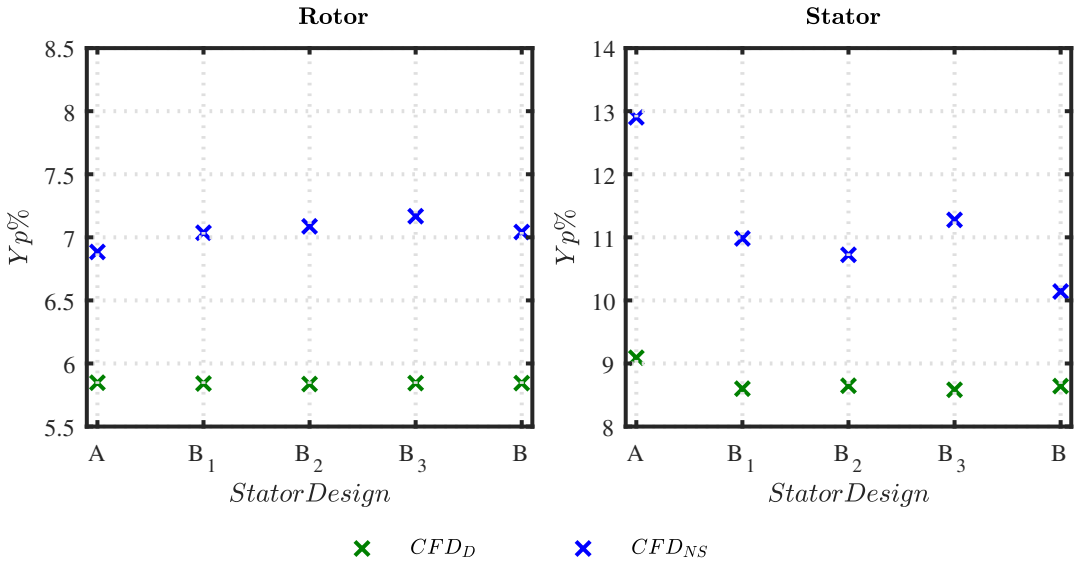

Figure 6.4: The effect of stator design on rotor and stator loss

of stators B_1 and B_3 is $5°$ higher than that of stators B_2 and B, the deviation angle is only $1°$ lower. The lower deviation is expected as per "Carter's rule", see equation 4.1, where the deviation is proportional to the blade angle change. At both $Design$ and $Near\ Stall$ the stator exit flow angle is less sensitive to the inlet flow angle for all stator B re-designs compared to stator A.

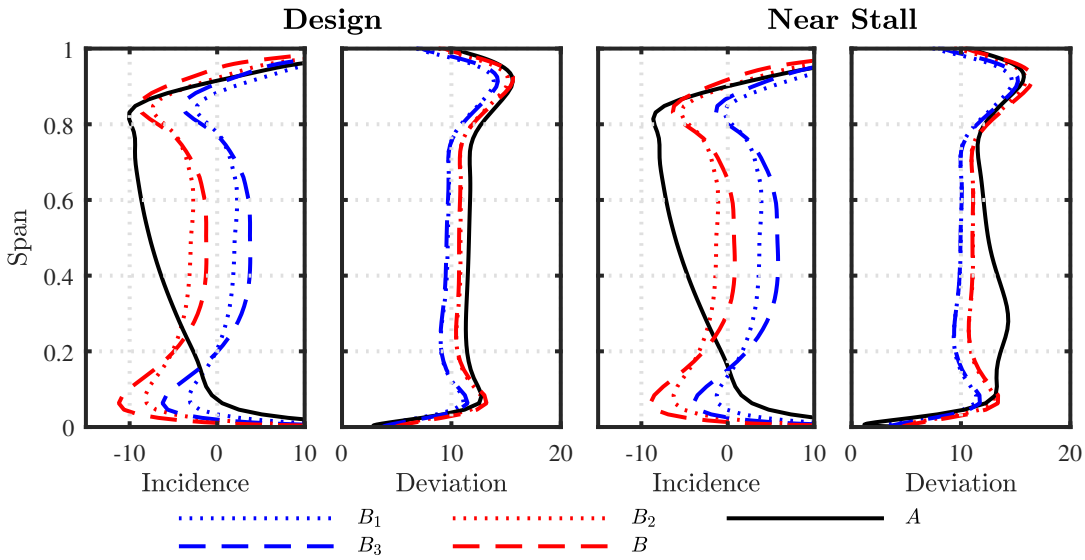

Figure 6.5: The effect of stator design on stator incidence and deviation angles at $Design$ and $Near\ Stall$

Also, as ϕ decreases towards stall, the incidence and deviation increase for all stator designs. For all stator B designs, the deviation increase is less than $1°$ for a $3°$ increase in incidence. Although the deviation of stators B_2 and B is higher than stators B_1 and B_3 from figure 6.5 the stator loss is lower, as seen in figure 6.4.

The CFD predicted stator stagnation pressure loss contours are plotted for the best performing stator, B, and the worst performing stator, B_3, at $Near\ Stall$ compared against stator A in figure 6.6. It can be seen that the stator corner separation is smaller in stator B designs than stator A, both at $Design$ and $Near\ Stall$. These results support the approach of decreasing the endwall incidence angles to decrease the stator loss. In particular the change of incidence has eliminated the hub corner separation at $Design$ and $Near\ Stall$. At $Design$, both stator B designs' wakes are very similar. Whereas, at $Near\ Stall$ the loss in stator B_3 hub region is higher than that of stator

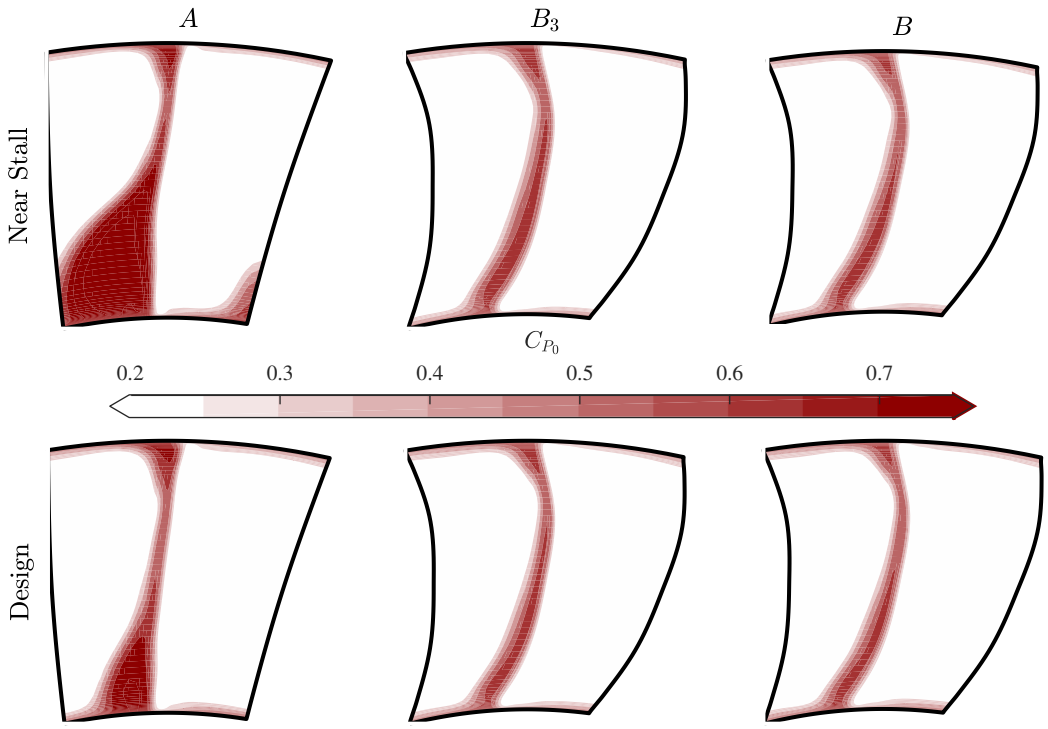

Figure 6.6: The predicted effect of stator leading edge re-cambering design on stator loss

B. This is to be expected as the hub incidence in B remains lower off-design. Figure 6.7 shows the pressure distribution at the midspan of the stator blades at two different flow coefficients. The increased inlet metal angle of stator B_3 shifts the loading of the blade forwards. Traditionally a rearward loaded blade has higher deviation.

On the other hand, the higher suction peak of stator B_3 with respect to stator B corresponds to a higher velocity on the blade surface. From Denton [9], entropy generation in boundary layers is proportional to V^3. Since stator B_3 surface velocity is higher than stator B, in the first 20% of the chord, the loss associated with the boundary layer entropy generation is higher. Therefore, stator B has higher deviation but lower loss.

Stator B was chosen as the best performing one with the highest efficiency increase, both at $Design$ and $Near\ Stall$. It was 3D printed and the same investigation procedure as that of stator A was conducted. The 3D design of stator B is shown in figure 6.8. Looking at the the trailing edge distribution, the blade seems to have some lean, even though the stacking line at the centroid of the stacking line is radial.

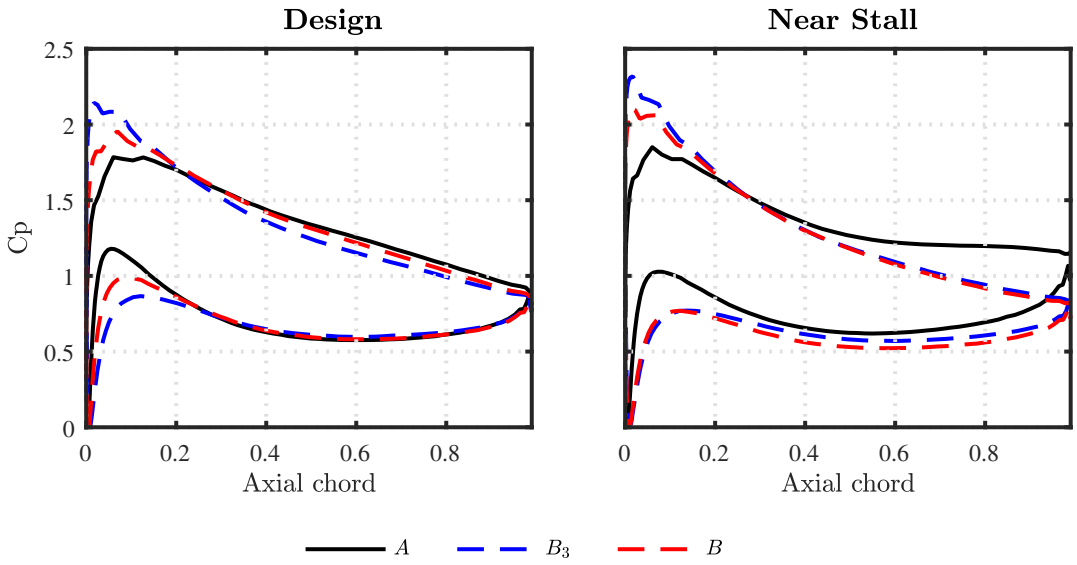

Figure 6.7: The effect of stator design on stator mid-span surface pressure distribution

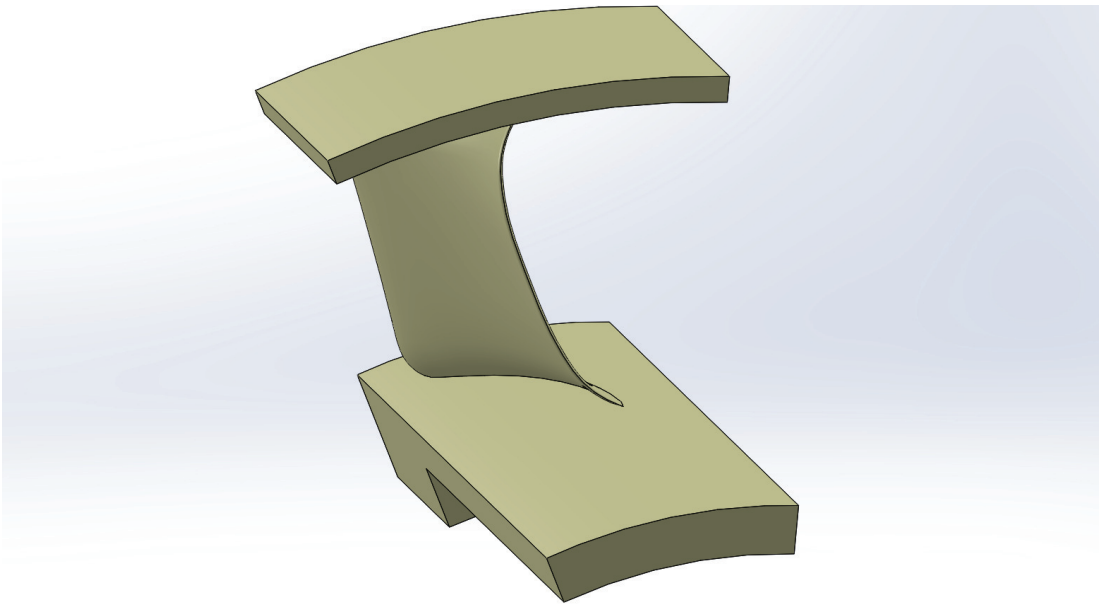

Figure 6.8: CAD section design of the 3D printed stator B

6.1.2 Experimental study of stator design

Stators A and B where tested with the same rotor at $Design$ and $Near\ Stall$ flow coefficient, for Re ranging from 2×10^4 to 12×10^4.

Effect of flow coefficient

The rotor incidence and deviation angles at $Design$ and $Near\ Stall$ flow coefficient have been matched between stator A and stator B, as seen on figure 6.9. Thus, the stage flow coefficient and stator inlet flow is the same for the tests with both stators. The stator B incidence angle, as intended, is more uniform and lower at the endwalls compared to that of stator A. At the outer 20% of the span, the measured experimental incidence does not match the designed CFD incidence. This is expected as the CFD does not capture the endwall flow field accurately. In addition, the endwall incidence remains below $10°$ at all measured flow coefficients. Also, the increase in deviation at $Near\ Stall$ is lower in stator B than stator A, especially in the endwall region.

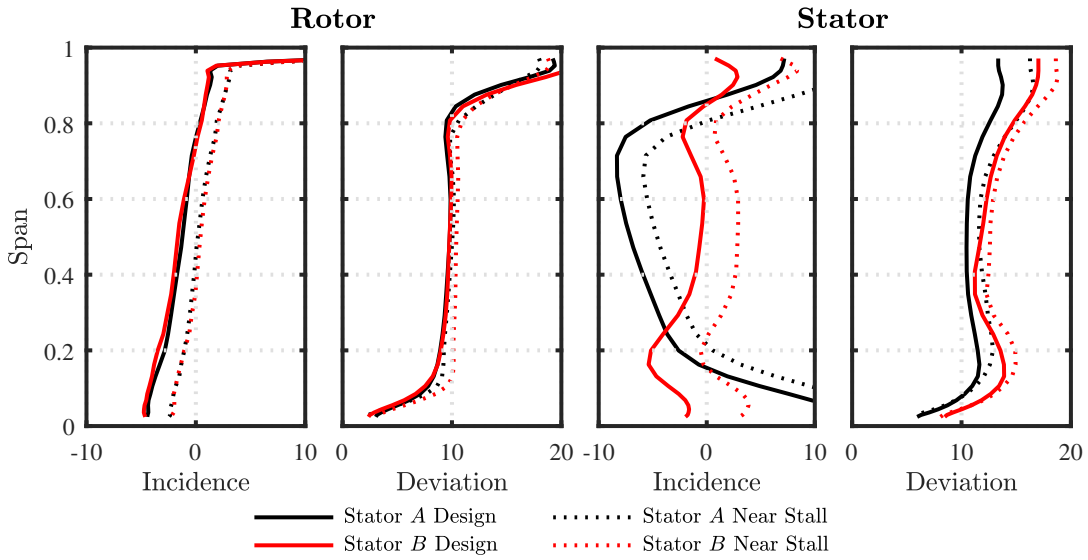

Figure 6.9: The effect of stator design on measured incidence and deviation

As discussed by Maffioli et al. [30], at incidence greater than $10°$, the laminar separation will not be able to transition and reattach, causing a large separated wake. Since

the endwall incidence on stator B was lower than 10° throughout the span. It was expected that the boundary layer separation would decrease along the suction side of the stator, mainly improving the stator hub endwall flow.

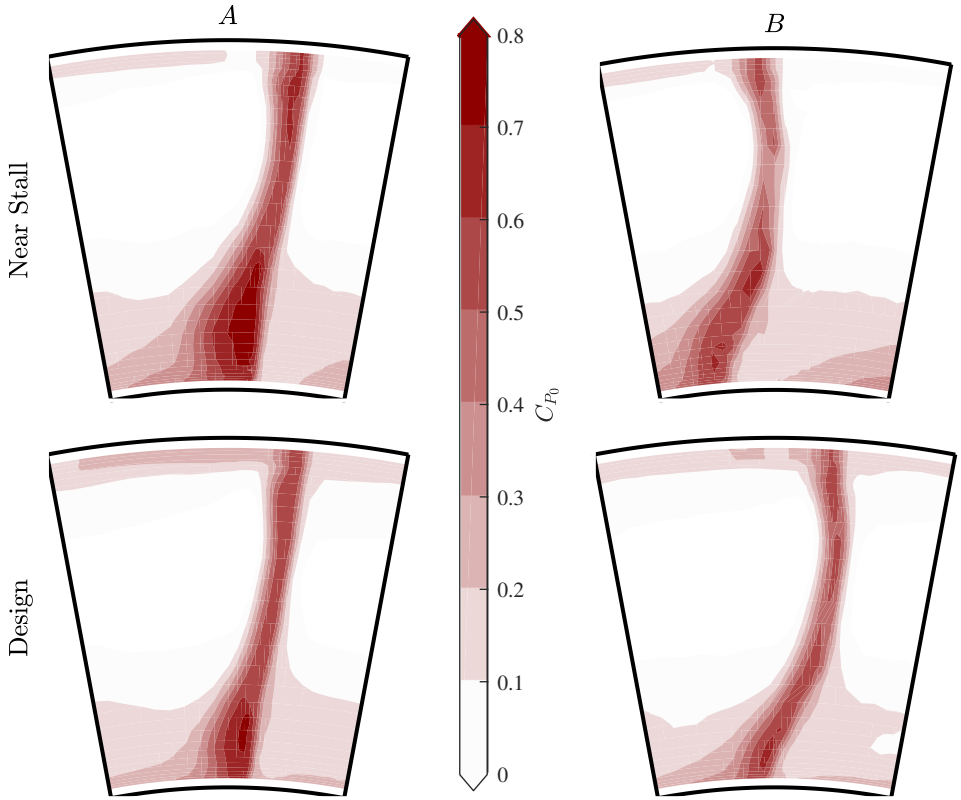

Figure 6.10: The effect of stator design on stator measured stagnation pressure deficit at $Design$ and $Near\ Stall$

It can be seen in figure 6.10, that both at $Design$ and $Near\ Stall$, the stator B wake in the endwall hub region is narrower and the core stagnation pressure loss is smaller. The hub endwall separation is almost gone at design and very small at near stall.
From figure 6.11 the loss breakdown of the the two stators at two flow coefficients is shown. It is clear that the stator B loss has decreased at both flow coefficients in comparison to stator A. This decrease was approximately 15% at $Design$ and 20% at $Near\ Stall$. The benefit arises primarily from the endwall regions as the separation cores decrease in size, visible in figure 6.10.
At $Near\ Stall$, more of stator's A span incidence is greater than 10°, therefore the

stator suction side separation would be greater. On the other hand, stator B incidence at the endwall region is below $10°$ for both, D and NS, therefore the separated region is lower and thus the endwall loss core is smaller. This is what leads to the larger loss decrease off-design in figure 6.11.

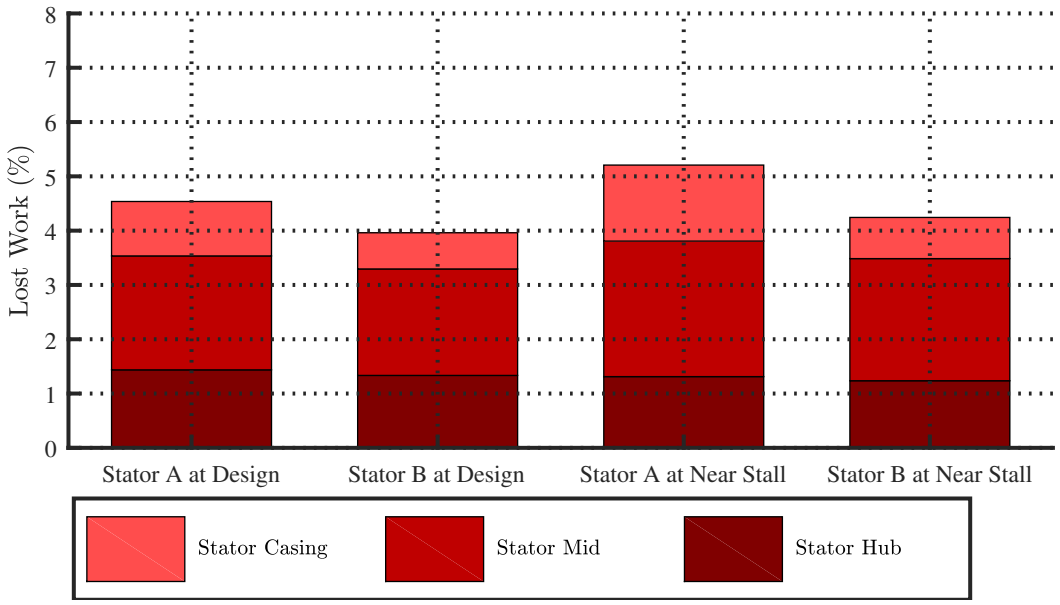

Figure 6.11: Stage loss breakdown for stator A and stator B at Re_D

Effect of Reynolds Number

When exploring the effect of stator B at a range of Re the endwall loss benefit is carried forward. From figure 6.12, it is clear that the hub endwall separation region has decreased in stator B for both Re.

At the lower Re the stator loss benefit is around 25% from stator A, see figure 6.13. The decrease in endwall loss is similar to that of the design Reynolds number , therefore the loss mechanism is the same for both Re.

Further more, the effect of loss across Re for both stators, as shown in figures 5.10, 6.13 and 6.14, indicates that the rotor loss remains mostly unaffected by the stator design change, and stator B has lower losses than stator A for the range of Re tested. The stator casing loss increases as the Reynold number is decreased, this is subsequent of the casing boundary layer thickening, increasing the loss associated with it.

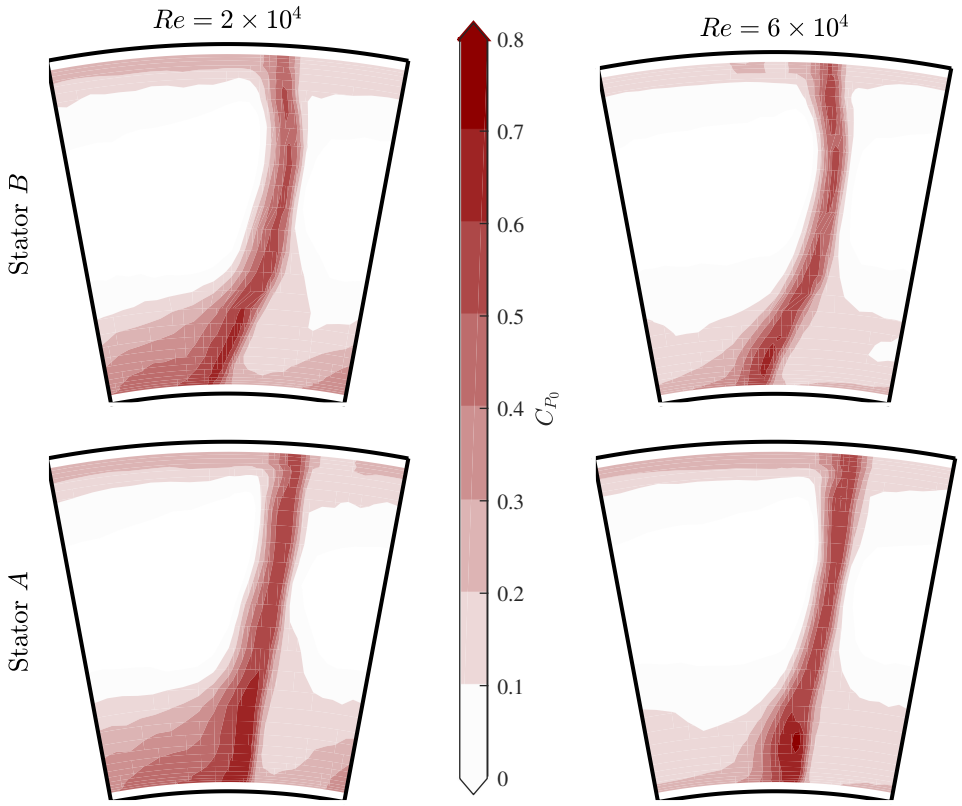

Figure 6.12: The effect of stator design on stator measured stagnation pressure deficit across a range of Re

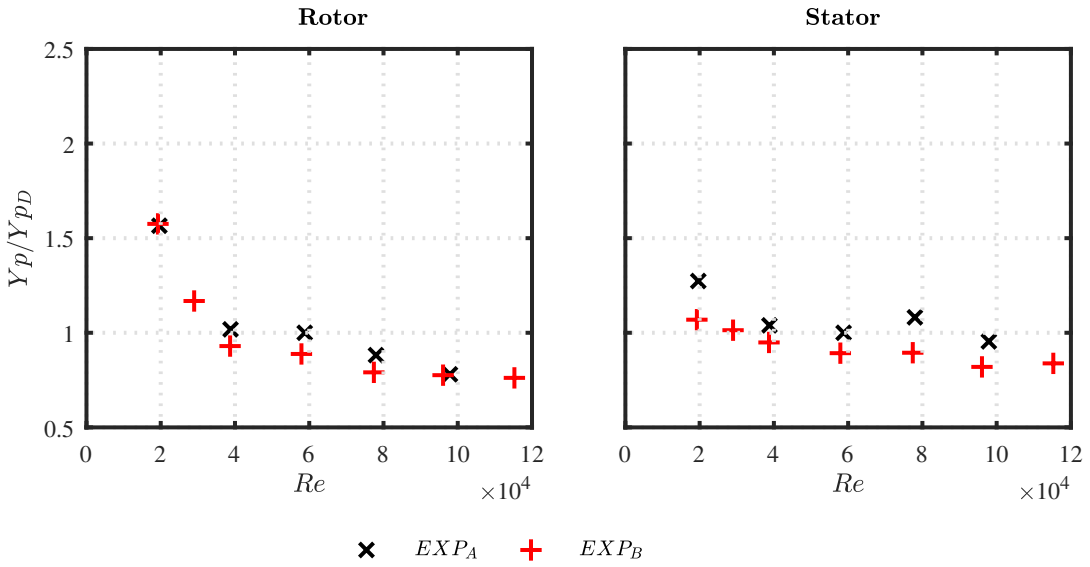

Figure 6.13: The effect of stator design on rotor and stator measured loss across a range of Re

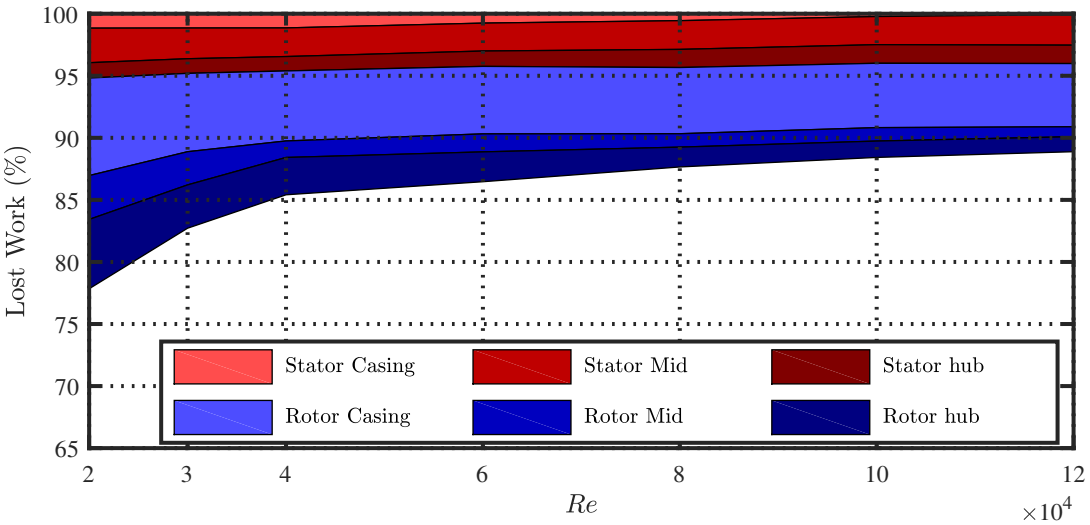

Figure 6.14: Stage loss breakdown across Re, using stator B

6.2 The effect of compound lean

Lean can be used to change a blade row loss by redistributing the spanwise loading. Compound lean, pressure surface down when looking at the hub, can increase the loading at the midspan and decrease the endwall loading in an attempt to decrease the endwall losses.

From the literature for high Re axial compressors, as discussed in subsection 2.2.3, the incorporation of 3D design features such as compound lean can decrease endwall losses as in figure 2.20 by Gallimore et al. [16]. Whether compound lean in low Re compressors can control the flow in a similar manner as in higher Re is investigated. An array of symmetric, about the midspan, compound lean distributions was superimposed on the radial stacking line of stator B. These designs were run in Turbostream to explore the effect of lean on the flow-field within stator B.

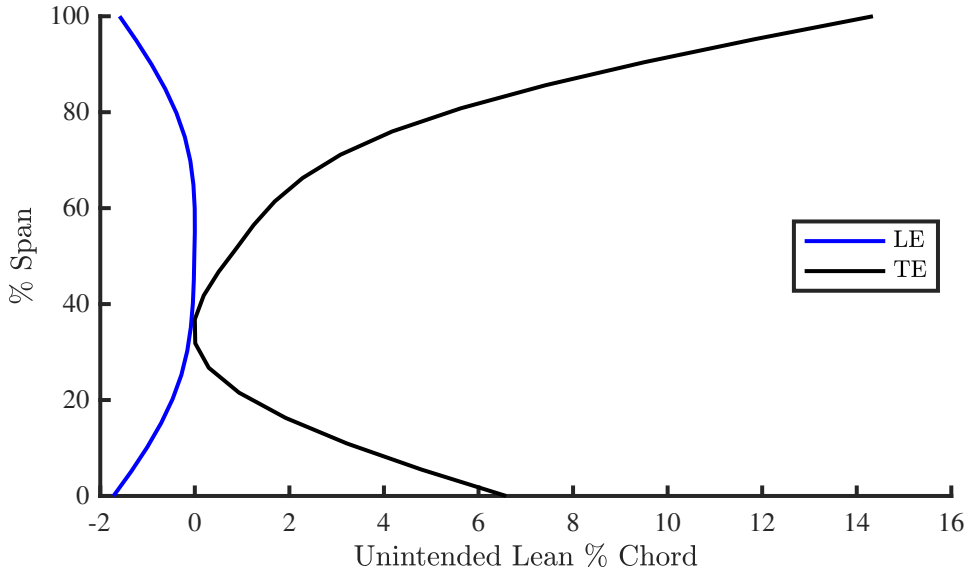

Figure 6.15: Unintended LE and TE compound lean caused by LER

In addition, LER can cause unintended lean or sweep Depending on the stacking line chosen. Figure 6.15 shows the extent of lean, as defined in figure 6.17 caused at the LE and TE of the stator after LER was introduced in section 6.1. Since LER And compound lean cannot be easily decoupled the lean distribution introduced in this section will be added on top of the lean caused by LER.

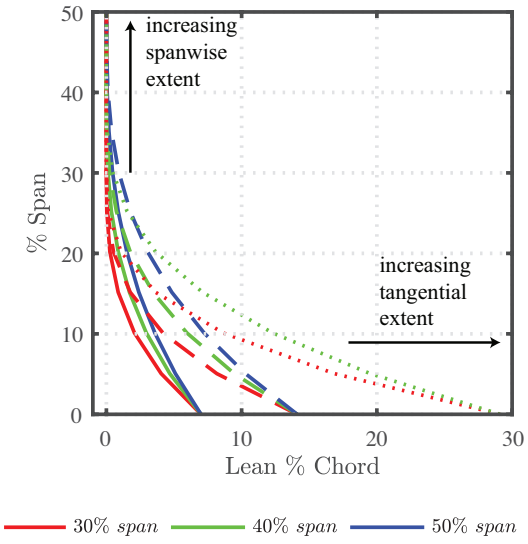

Figure 6.16: Stator lean distributions

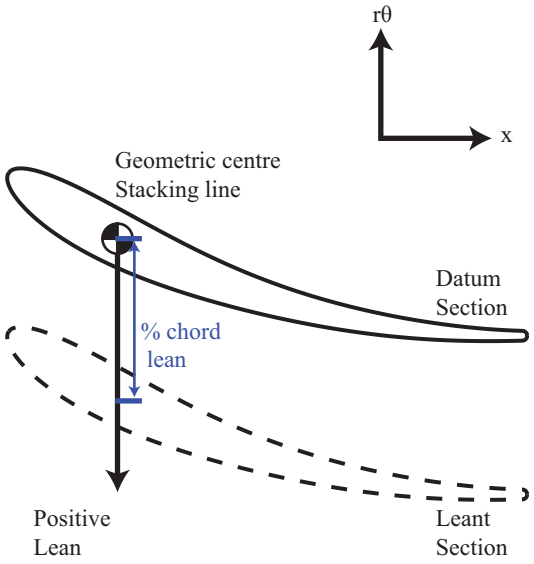

Figure 6.17: Lean extent definition

Two parametric studies were carried out, one on the spanwise extent of lean and one on the tangential extent of lean on the stator. The lossy region of the stator hub endwall extents into approximately 30% of the span, the minimum spanwise extent of the lean was set to be at 30% and was then increased at 10% intervals upto the midspan, see figure 6.16. Following Taylor and Miller [47] recommendation, for high Re 3D stator design, a $20°$ lean angle was considered as an optimal which, corresponded to 28% of the rotor chord tangential deviation of the stack-line, see figure 6.17, where positive lean was in the negative $r\theta$ direction. A parabolic distribution was implemented along the stack-line. A $7\%c$, $14\%c$ and $28\%c$ of lean extent were considered for the tangential extent study.

The lean distributions considered are shown in figure 6.16. 3D designs with each of the distributions shown here were generated and meshed. These were then computed on 3D CFD for the range of ϕ from 0.60, following the methodology described in section 3.3.

Two of the stator designs with lean were chosen to be 3D printed and experimentally tested at $Design$ and $Near\ Stall$ flow coefficients to compare with the numerical results. Firstly, the stator with the highest efficiency increase was chosen, stator C. Secondly, the stator with the highest stator loading redistribution, from endwall to

midspan, was chosen, stator D. This stator was chosen to inspect whether experimentally a low Re compressor would experience the same effect as the fully turbulent CFD and high Re literature predict. The results are presented in the following subsections.

6.2.1 Compound lean parametric studies using CFD

In this section the effect of the stator compound lean magnitude and spanwise extent are investigated computationally and the stators to be manufactured are chosen.

Effect of stator compound lean magnitude

Cases with 40% and 50% span extent demonstrated a similar trend to the cases with 30% span extent. Therefore, only cases with 30% span extent are included to demonstrate the effect of increasing the amount of lean in the tangential direction. Results in this section are taken at two flow coefficients, at $Design\ \phi = 0.55$ and at $Near\ Stall$ $\phi = 0.50$.

The stage efficiency at $Design$ and $Near\ Stall$ decreases with an increase in lean, depicted in figure 6.18(right). The decrease is higher at $Near\ Stall$. Since the rotor efficiency, figure 6.18(left), is unchanged, as expected, the stage efficiency change is caused by the introduction of compound lean in the stator.

The stator endwall loss, see figure 6.19, decreases while the midspan loss increases. Offloading the endwalls with lean has decreased the size of the endwall loss cores. By doing so, the midspan region is sacrificially loaded more, increasing the wake and loss concentration. The increase in the midspan loss is greater than the endwall loss decrease, therefore the overall stator loss increases. In the highly leaned stators the increase in the midspan region increases more while the decrease at the endwalls increases at a lower rate.

At $Near\ Stall$ the same trend is present but at a higher extent. The incidence and deviation of the stator is higher at $Near\ Stall$, see figure 6.9, thus the separated region of the highly loaded midspan region increases. That is why the efficiency decreases more in figure 6.18(right).

From the investigation of the effect of lean extent, a highly leaned stator of 28% chord was proven to have the highest load redistribution. Whereas the less leaned stators,

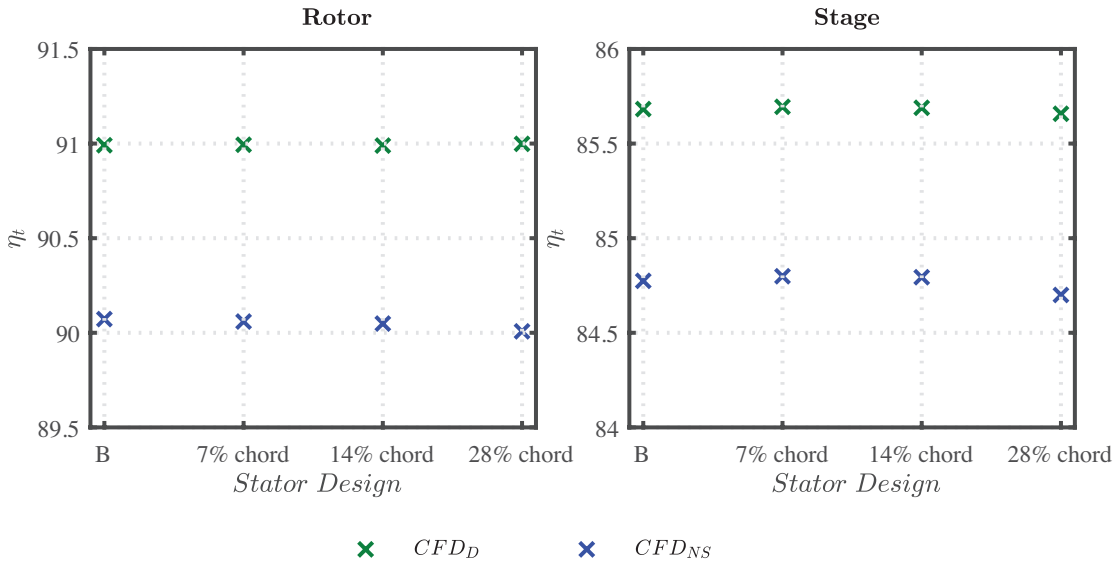

Figure 6.18: Stator compound lean magnitude effect on rotor and stage efficiency

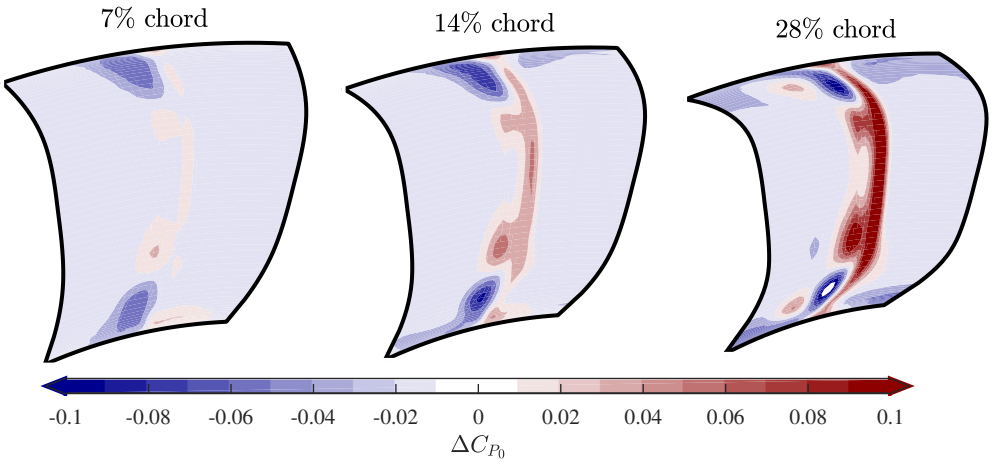

Figure 6.19: Stator compound lean magnitude effect on stator stagnation pressure loss, change from stator B at $Design$

7% and 14% chord, were considered for the high efficiency low loss stator. Below the effect of stator compound lean spanwise extent is considered to choose the amount of spanwise lean for the previously stated stators.

Effect of stator compound lean spanwise extent

The effect of stator compound lean spanwise extent for the moderately leaned stator of 14% chord is investigated in this section. Figure 6.20 shows that the performance of the case with 30% span extent does not differ, as much as the other cases, from case B. That is because the leaned part of the stator does not cover a large enough part of the span to offload the endwalls substantially and load the midspan region as the cases with higher span coverage. For the three different magnitudes of stator compound lean, the efficiency trend with respect to compound lean spanwise extent is shown in figure 6.20.

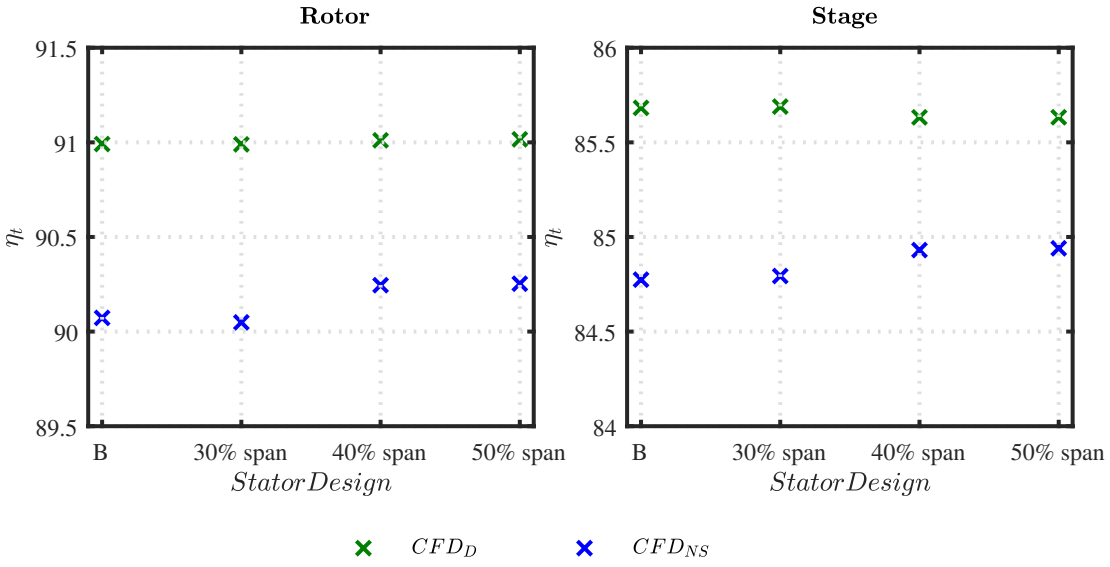

Figure 6.20: Stator compound lean spanwise extent effect on rotor and stage efficiency

From figure 6.20, both 40% and 50% span cases have a decrease in stage efficiency at $Design$ and an increase in stage efficiency $Near\ Stall$. From figure 6.21, it can be seen that the stator with the largest loss decrease in the endwall region was that of 40% span lean. Therefore, 40% span lean was chosen as the best performing one.

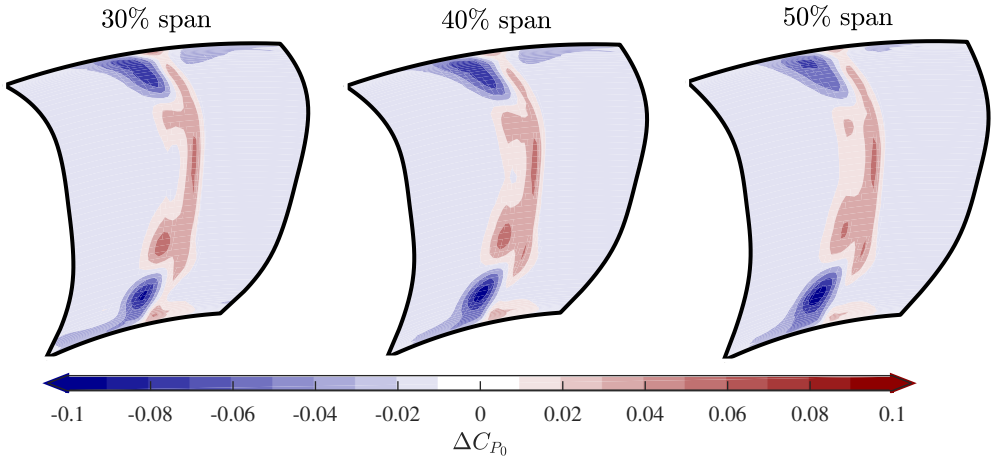

Figure 6.21: Stator compound lean spanwise extent effect on stator stagnation pressure loss change from case B at $Design$

From the analysis conducted above stator C, best performing, was chosen to have 40% spanwise lean and 14% chord lean extent. Stator D, with the largest load redistribution and the least increase in performance, was chosen to have 30% spanwise lean and 28% chord lean extent. The design of stators C(left) and D(right), that was used to 3D print and test, are shown in figure 6.22.

The incidence and deviation angles for the stage with stators B, C and D were plotted in figure 6.23. As expected there is no effect on the rotor angles stator incidence angle for all three stator cases. The stator deviation angle has increased in the leaned cases both at $Design$ and $Near\ Stall$ by less than $0.5°$.

Looking closer to the flow distribution of the $Near\ Stall$, larger deviation increase, in figure 6.24 it can be seen that there is a small flow redistribution with a decrease of axial velocity in the midspan region causing the increased deviation. Nevertheless the changes associated with all leaned cases are small.

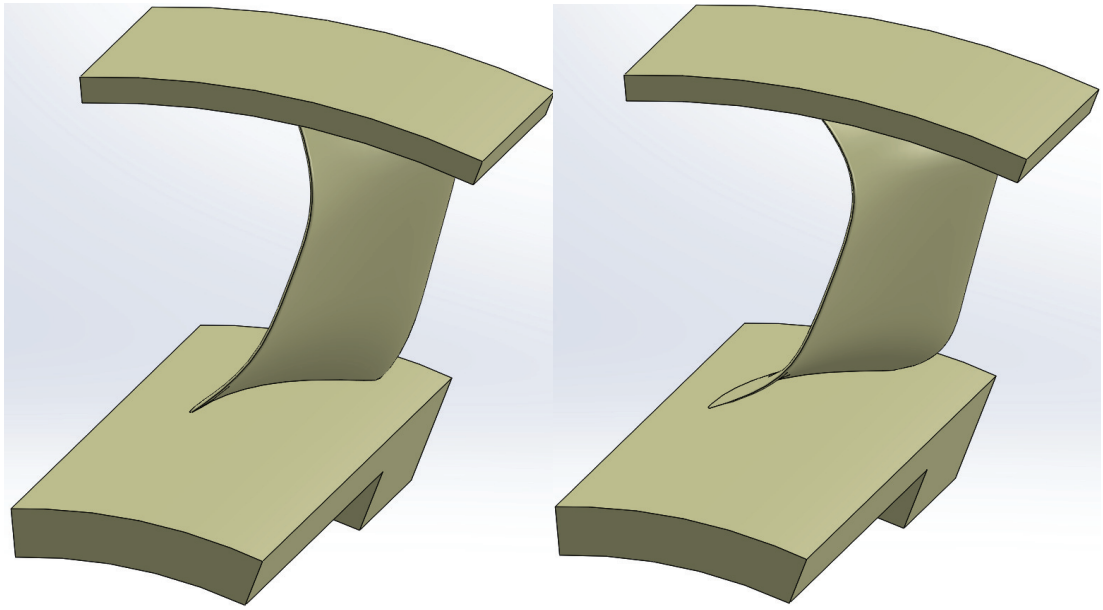

Figure 6.22: CAD section design of the 3D printed stators, C(left) and D(right)

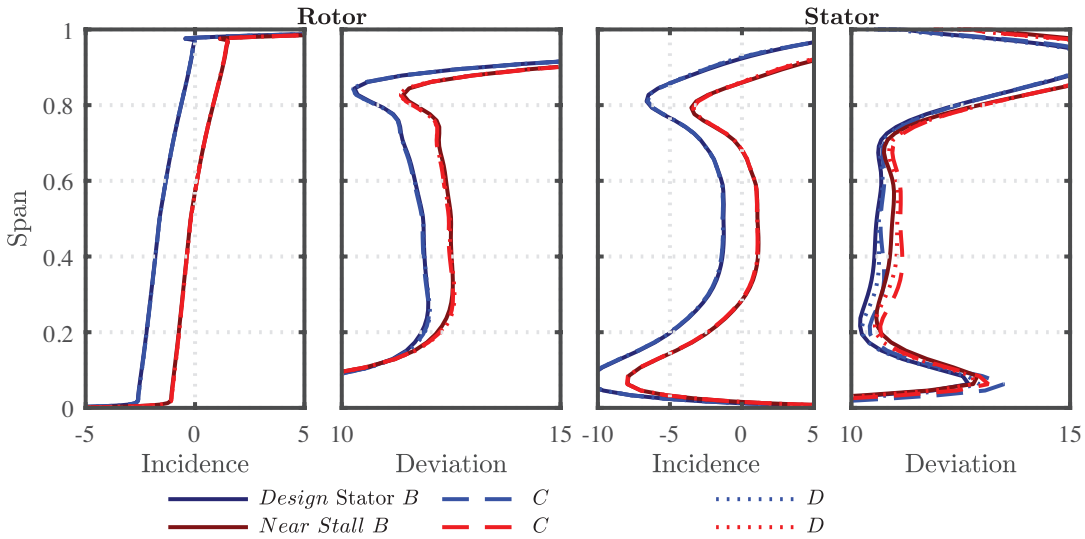

Figure 6.23: Computed spanwise incidence and deviation distributions for the rotor and stator at Re_D

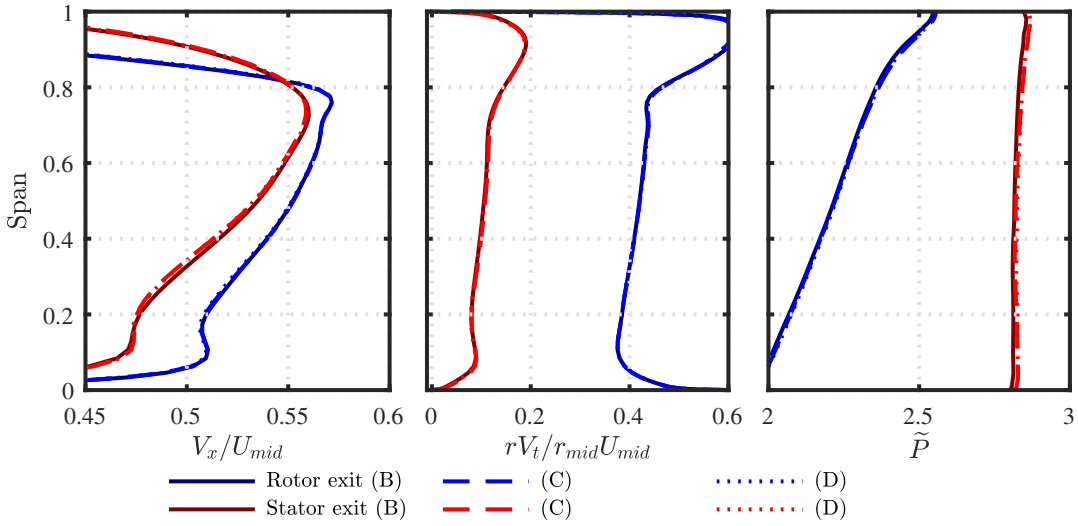

Figure 6.24: Computed spanwise, pitch-averaged, distribution of non-dimensional axial velocity, angular momentum and static pressure at $Near\ Stall$ for Re_D

6.2.2 Stator compound lean effect on experimental performance

Stators C and D, from figure 6.22, were investigated at $Design$ and $Near\ Stall$ flow coefficients for two Reynold numbers, $Re = 2 \times 10^4$, and $Re_D = 6 \times 10^4$.

The stagnation pressure loss contours for stators B, C and D were plotted in figure 6.25 at two different flow coefficients. The hub endwall corner separation from stator B has decreased in both stators C and D. On the other hand, the midspan loss associated with the wake increased in width and intensity. The casing region seems unchanged. The trend is similar for both flow coefficients. Figure 6.26 shows that at $Near\ Stall$ Stator C and D have a stator midspan and casing loss increase. The casing loss for both stator is approximately two times bigger. The midspan increase is approximately 50% higher in stator C and 70% in stator D.

There are two main differences between the two flow coefficients. Firstly, the hub endwall separation decrease is higher at $Near\ Stall$ than at $Design$. Secondly, the midspan loss increase is larger $Near\ Stall$. The main difference between stator C and D is that the loss increase is higher in the upper midspan region of stator D. Since the $Near\ Stall$ changes are similar to the ones on $Design$ but larger, the $Near\ Stall$ flow is investigated in more detail.

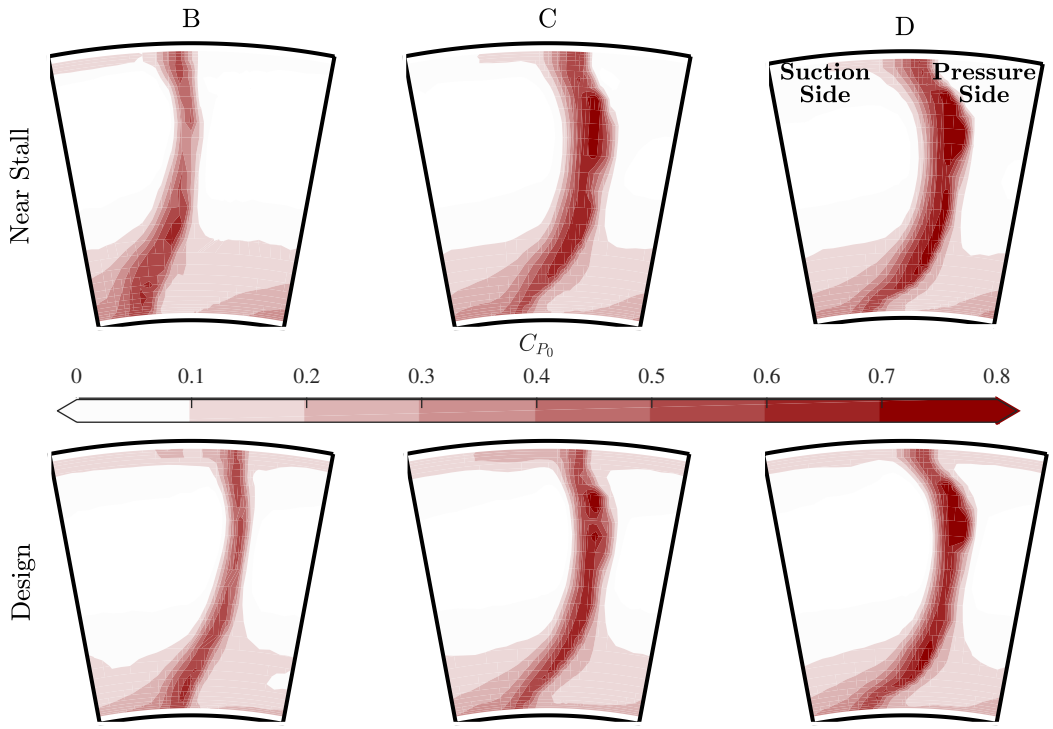

Figure 6.25: Stagnation pressure loss contours at $Re = 6 \times 10^4$

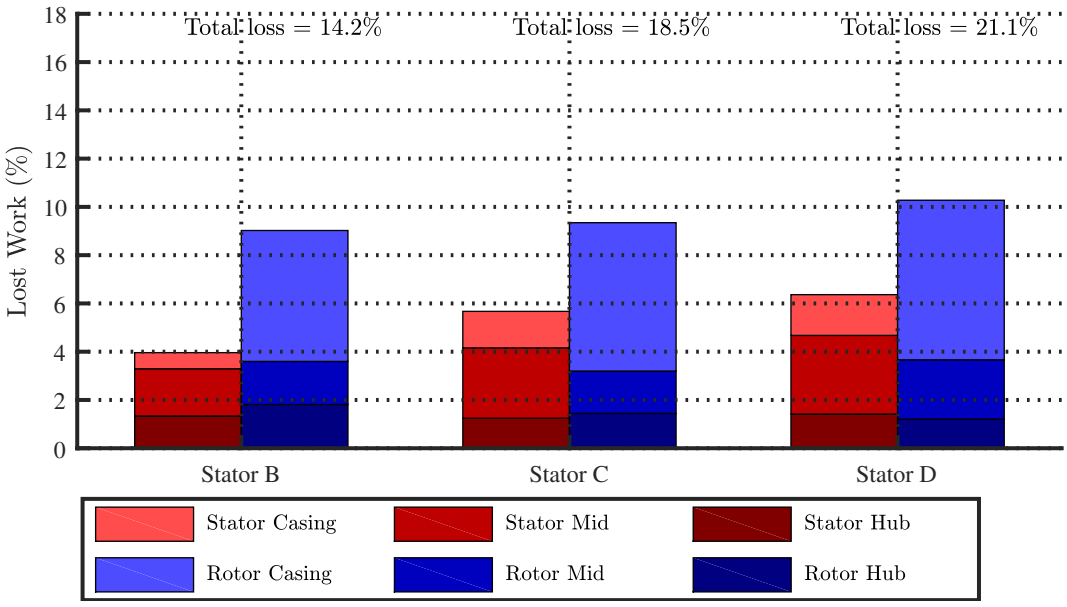

Figure 6.26: Stator loss breakdown for stators B, C and D at $Near\ Stall$

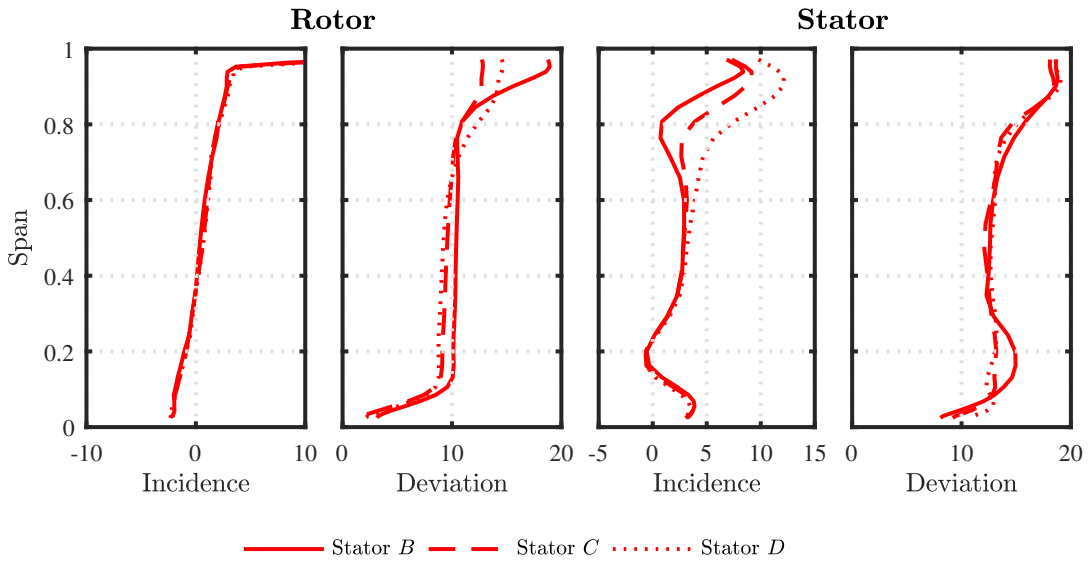

Figure 6.27: Measured spanwise incidence and deviation distributions for the rotor and stator at $Near\ Stall$ for Re_D

The rotor and stator incidence and deviation were plotted for stators B, C and D at $Near\ Stall$ on figure 6.27. The same rotor was used for all experiments and the rotor incidence was matched at each flow coefficient, therefore the subsequent changes downstream of the rotor inlet are an effect of the different stators.

Even though the rotor has not been changed, the rotor exit flow has been affected by the change in stator geometry. The deviation angle at the casing region has decreased, which is a consequence of the increase in tangential velocity and decrease in the axial velocity in that region, see figure 6.28. This in turn caused the increased incidence angle at the stator inlet casing region. The increased incidence angle, closer to $10°$, increases the stator separation and loss in the upper midspan to casing region.

Compound lean has caused a mass flow redistribution from the casing region to the midspan region. The rotor exit casing pressure has increased pushing the flow radially inwards, see figure 6.28. The effect is higher in stator D than in stator C as expected, due to the increased compound lean.

On the other hand the stator hub deviation has decreased, see figure 6.27. This was achieved because of the increased axial hub velocity at the rotor and stator exit, see figure 6.28. Even-though the hub region loss has decreases due to the introduction of

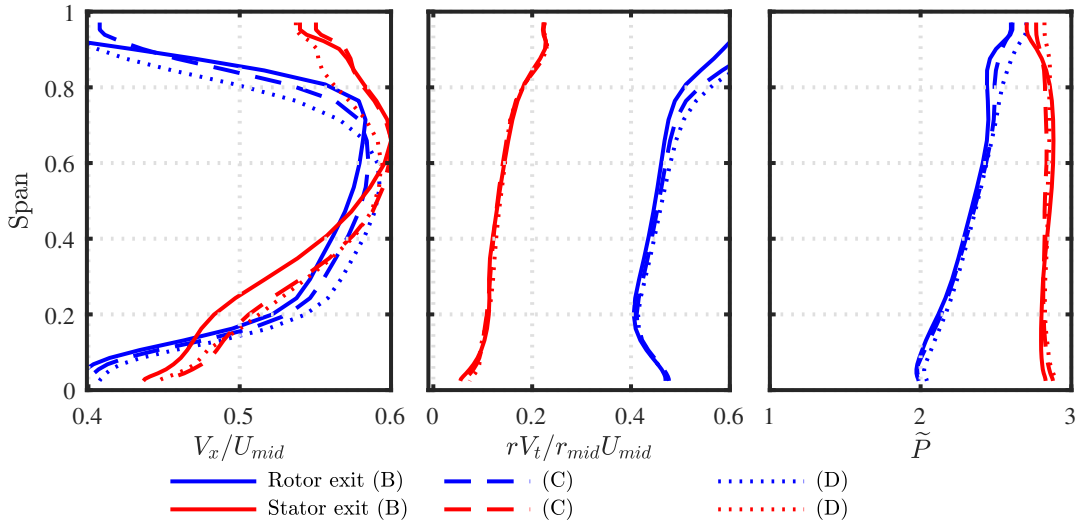

Figure 6.28: Spanwise, pitch-averaged, distribution of non-dimensional axial velocity, angular momentum and static pressure at $Near\ Stall$ for Re_D

lean, the increase on the midspan and casing region losses is much higher. Therefore the overall stator loss increases, see figure 6.26. There is also rotor loss increase due to the mass flow redistribution but less than that in the stator.
Comparing figures 6.27 and 6.28 with figures 6.23 and 6.24, it is clear that the effect of stator compound lean is different in CFD and experiments. CFD had calculated a much smaller effect on the spanwise flow. This can be subsequent to the mismatch between the endwall flow field.

Effect of Reynolds number

A similar pattern in the stator loss change is present at lower Re, see figure 6.29 versus figure 6.25. The stator hub loss decreases by a small amount while the midspan and casing loss increases, see figure 6.30. The increase is lower, from the design Reynolds number, since the stator loss is already high due to the low Re, as discussed in section 5.2.2.
The incidence in stators C and D midspan region increases, see figure 6.31, as the axial velocity decreases and the tangential velocity increases at the rotor exit, see figure 6.32. Which, increases the stator separation and loss in the midspan wake.

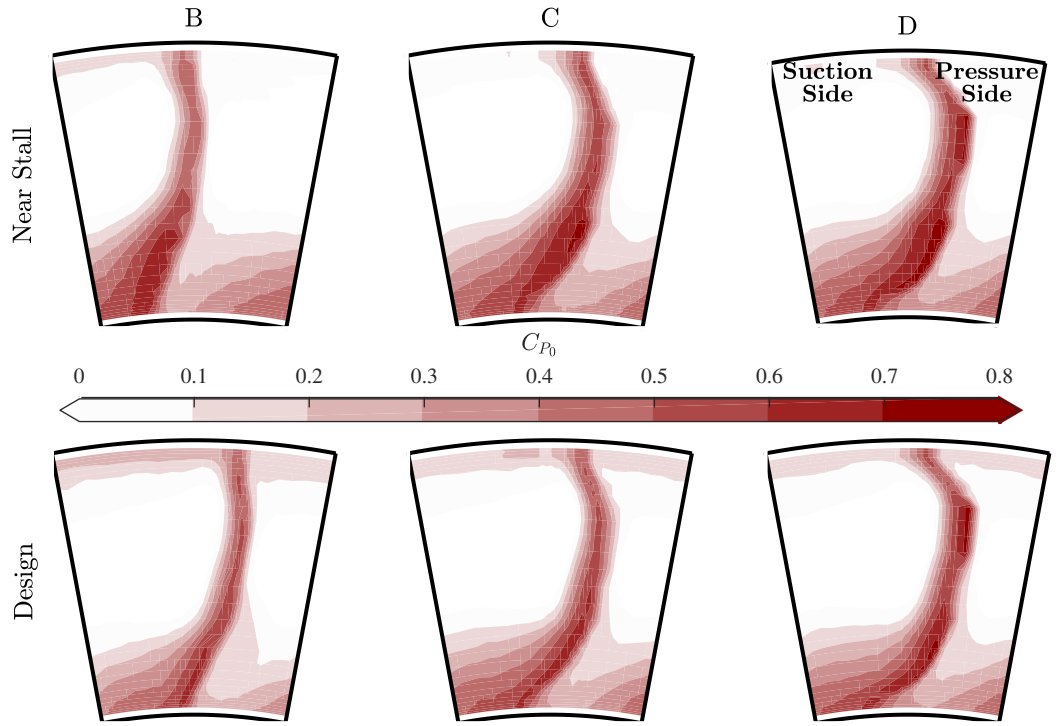

Figure 6.29: Stagnation pressure loss contours at $Re = 2 \times 10^4$

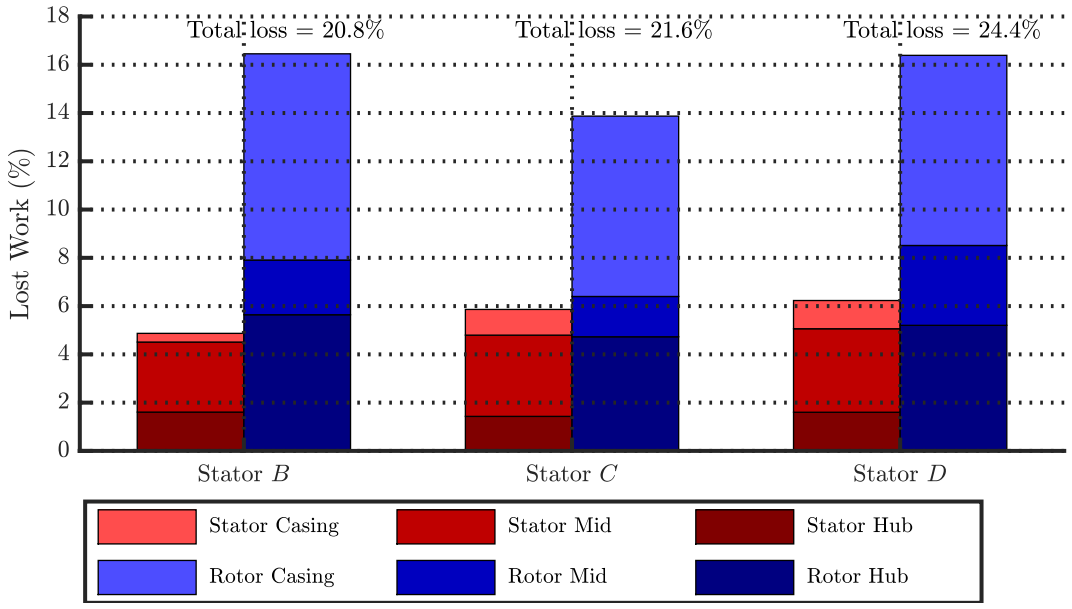

Figure 6.30: Stator loss breakdown for three stators at $Near\ Stall$ for $Re = 2 \times 10^4$

The decrease in the rotor tip deviation angle, see figure 6.31, and the mass flow redistribution, see figure 6.32, is lower thus the effect on the already lossy rotor is smaller compared to that of the higher Re, see figures 6.25 and 6.26.

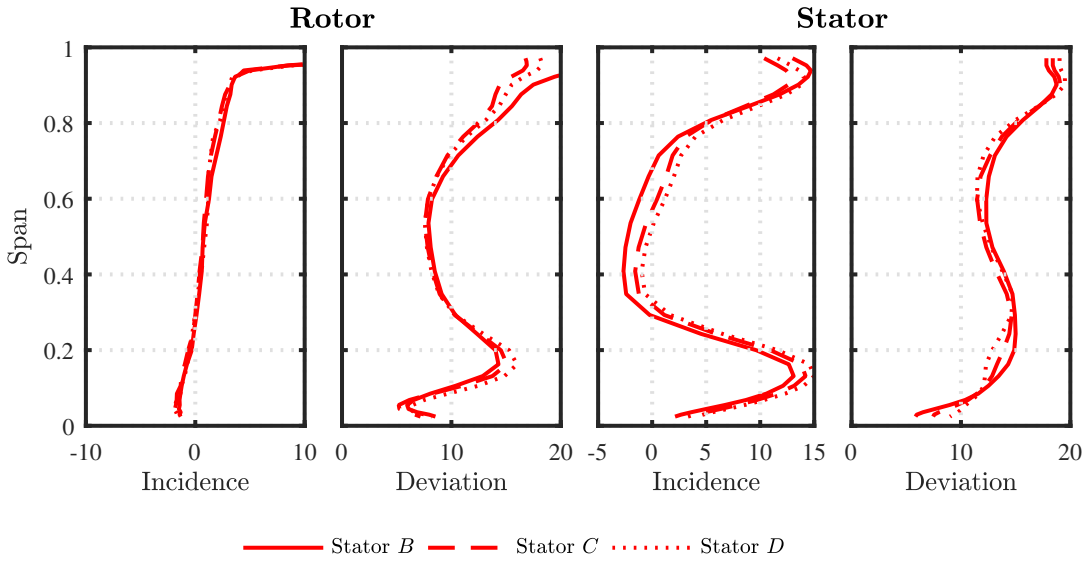

Figure 6.31: Measured spanwise incidence and deviation distributions for the rotor and stator at $Near\ Stall$ for $Re = 2 \times 10^4$

Stator compound lean has managed to redistribute flow towards the hub and decrease the hub stator corner separation and the loss associated with it. This was achieved while sacrificing the casing and midspan region. The loss in those regions increased at a higher rate, thus the overall stage performance has deteriorated. This is for both flow coefficients and Re discussed in this section.

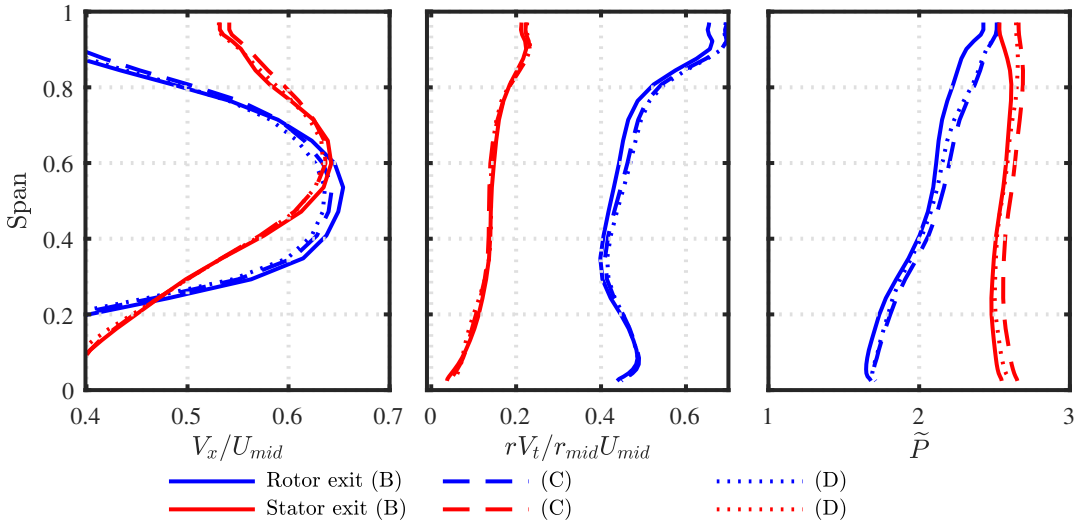

Figure 6.32: Spanwise, pitch-averaged, distribution of non-dimensional Axial velocity, angular momentum and static pressure at $Re = 2 \times 10^4$ and $Near\ Stall$

6.3 Summary

The effects of stator leading edge re-cambering and stator compound lean on stage performance have been investigated.

From the experiments, the rotor exit flow angle variation at the design Re of 6×10^4 changes from the design intent due to increased endwall secondary flows. Therefore, and as shown in this chapter, if the stator incidence can be matched to the actual rotor exit flow variation then the stator loss can be decreased. At even lower Re, 2×10^4, the increased secondary flow leads to a larger spanwise variation in exit flow angle at rotor exit than at the design Re. Therefore, a further decrease in endwall loss can be achieved, which can have upto 2.5% gain in efficiency. This is of great importance, as the flow at low Re is very sensitive to positive incidence flow separation.

At low Re applying compound lean redistributes loading in a similar way to that observed in turbomachinery operating at high Re. However, applying lean can have unexpected consequences at low Re, because the precise balance of loss between the endwall and mid span is difficult to predict computationally. In the case examined, which started with relatively low levels of endwall loss, adding compound lean overloaded the stator region away from the endwalls leading to increased loss levels overall

and spanwise flow redistribution. The midspan loading and incidence increase puts the blade in a flow that it is not capable to handle as in higher Re. The blade separates further upstream causing the wake width to increase and subsequently increase loss. This can be troublesome for designers using computational tools during 3D design processes. Designers of low Re axial compressors should try and use experimental data early in the process, especially in the endwall region.

Chapter 7

Conclusions

This thesis presents an experimental and computational study into the flow field of a low Reynolds number axial compressor stage, the Re dependent flow features and the effect different designs have on these. For this purpose a 5 times low Re test rig was designed and instrumented. The major findings along with recommendations for future work are summarised in this chapter.

7.1 Major findings

The key findings from the results (chapters 4, 5 and 6) are presented in the following three sections, respectively.

7.1.1 Low Reynolds number axial compressor flow field

As shown experimentally, the major contributors to loss in a low Re compressor stage are the 3D endwall flow features of both the rotor and stator. The loss increases with a decrease in flow coefficient. The midspan region is less sensitive and the 2D profile loss does not increase at the same rate. The stage loading is higher than designed due to the highly loaded rotor endwalls.

The steady fully turbulent RANS used can calculate the rotor midspan flow field along the range of flow coefficients investigated. However, the rotor endwall flow is not

correctly captured, therefore, the stator inlet flow is not captured. The corner separation increases at a higher rate than in experiments. This is because the simulations are sensitive to the stator hub region incidence. Therefore,and as a result the stator loss is over estimated.
The flow in the endwalls is transitional due to the low velocities, thus being more prone to fully turbulent CFD not calculating it correctly. Overall, the computational studies performed suggest that at low Re, designers need to be cautious when using fully turbulent RANS solvers, especially when designing the endwall regions.

7.1.2 Reynolds number effects

At Re greater than the design value of 6×10^4, both midspan and endwall losses decrease. While at Re lower than design, the losses increase. For Re lower than 4×10^4, the rotor loss increases at a higher rate than the stator loss. The major contributor to this increase is the rotor hub flow corner separation, compared to the low increase due to the midspan and tip flow. The corner separation increases, both in spanwise extent and its core strength. Also, the tip region wake width increases and the tip vortex core is not distinctly separated form the blade wake, as at the higher Re. This is an indication of a stalled tip with separated flow.
The Re (4×10^4) below which there is a high rate of loss increase is lower than that discussed in chapter 2 (10×10^4). Using a compressor stage designed for low Re transition and the turbulent separation point is closer to the location of the maximum pressure drop on the suction side. Therefore,the 2D profile losses stay low.
The endwall flow mismatch on the rotor hub between the experiments and the simulations increases at the lower Re, (2×10^4) . The mass flow deficit and loss increases with decreasing Re in the experiments but not in the simulations. This further emphasizes the effect of the transitional flow in the rotor hub region and its effect in the loss.

7.1.3 Effect of design changes on performance

The effect of stator leading edge re-cambering and compound lean on the performance of the compressor stage were investigated with the aim of increasing the efficiency and range of the compressor stage.

Leading edge re-cambering

Four different stator leading edge distributions were simulated using fully turbulent steady RANS CFD. The case that provided the highest stage efficiency increase and stage loss decrease both at $Design$ and $Near\ Stall$ was chosen to be 3D printed and investigated experimentally. It was shown that a decrease in endwall incidence decreases the stator corner separations, primarily on the hub. While, leaving the rotor performance mostly unaffected. This was observed both in the simulations and the experiments.
Additionally, the performance increase was shown to carry over across the whole range of Re investigated. Also, the loss breakdown across the stator has shifted to most of it being in the midspan region.

The effect of compound lean

By using compound lean on the stator stacking line in addition to the leading edge re-cambering, the flow was redistributed and the hub endwall loss was reduced. This was done with the sacrifice of increasing the midspan and casing region loss at a higher rate, thus increasing the stator overall loss.

7.1.4 CFD capabilities and limitations

The fully turbulent RANS used in this thesis has captured the midspan flow field of the compressor stage at design flow coefficient and Re. CFD did not capture the endwall flow accurately at design. The mismatch increased at off-design flow coefficient and lower Re.

7.2 Recommendations for future work

The work performed in this thesis demonstrates that a compressor stage designed for low Re, with a forward loaded cross-section, can reach Re of less than 4×10^4 before the losses start increasing exponentially. These losses are primarily concentrated in the rotor hub corner separation at Re less than 4×10^4. Also, the range of the stage is

limited to a 10% decrease from the design flow coefficient of 0.55. Finally, after stator redesigns, the loss dominant stator flow features switched from the endwall corner separations to the midspan 2D profile loss.
Throughout the course of the work carried out for this dissertation, a number of areas of future work have been identified to complement the existing studied data.

7.2.1 Rotor pitch to chord ratio

Increasing the pitch to chord ratio of the rotor hub can decrease the diffusion factor and suppress separation at low Re. This can be achieved by either increasing the chord of the rotor hub region or by increasing the number of blades, thus decreasing the pitch. Increasing the chord will also increase the local Re. Any, decrease in separation and any performance increase could be a consequence of that.
Increasing the blade number will increase the wetted surfaces and in turn increase the stage 2D profile loss. Since the rotor losses at low Re are dominated by the 3D endwall losses, then a small compromise of increased profile loss for a large decrease in endwall loss could be achieved. An experimental investigation of the effect on pitch to chord ratio, could provide an inside. Industry standard CFD cannot calculate the endwall flow field as it is missing the effect of transition in the flow.

7.2.2 Rotor compound lean

The rotor loading factor is highest at the endwalls, therefore future studies could use compound lean to redistribute the loading towards the midspan. This could be used to decrease endwall loss and increase the rotor performance.

7.2.3 Rotor exit endwall velocity triangle design

Another suggestion for future work involves the introduction of rotor exit endwall velocity triangle design to this compressor stage as described by Auchoybur and Miller [1]. The rotor exit endwall velocity triangles were not designed using 3D flow features in mind or the stator endwall performance. By designing the rotor endwall exit angle,

the incidence on the stator endwalls could be reduced, decreasing the 3D losses on the stator. Therefore, the stage efficiency would also increase.

7.2.4 Blade suction side surface treatment

The increase of the surface roughness or the introduction of flow trips on the suction side of both the rotor and stator could be investigated in future studies. This can further shift the transition upstream on the blade suction sides and decrease the turbulent separation. Therefore, the profile loss along the span of the blades would also decrease.

7.2.5 Tip gap investigation

A preliminary investigation into the effect of rotor tip clearance on the performance of the compressor stage was carried out using CFD and stator A was used. A range or tip gap sizes was tested from 0.1% to 5% chord, at the $Design$ flow coefficient all the way to the lowest converging flow coefficient.
The case with 5% did not converge at flow coefficients lower than $Design$, therefore in the following figures there are no $Near\ Stall$ data at 5% tip gap. The results of this investigation are discussed in this subsection and recommendations for future work are made.

Effect on efficiency

The main contributor to the increase of the loss associated with the rotor over the range of tip gap sizes investigated is the loss due to the tip vortex. Figure 7.2 shows that the loss due to the core of the vortex increases in size and magnitude as the gap increases. Since the gap increases, there is more spillage from the pressure side to the suction side, which in turn mixes with the oncoming flow and the spillage rolls into a bigger vortex. It is also possible to say that at lower flow coefficients the core travels closer to the suction side of the next blade. The bigger vortex core present at the largest tip gaps is more prone to impinge onto the subsequent blade at a higher flow coefficient, thus inducing stall at a higher flow coefficient and decreasing the operating range.

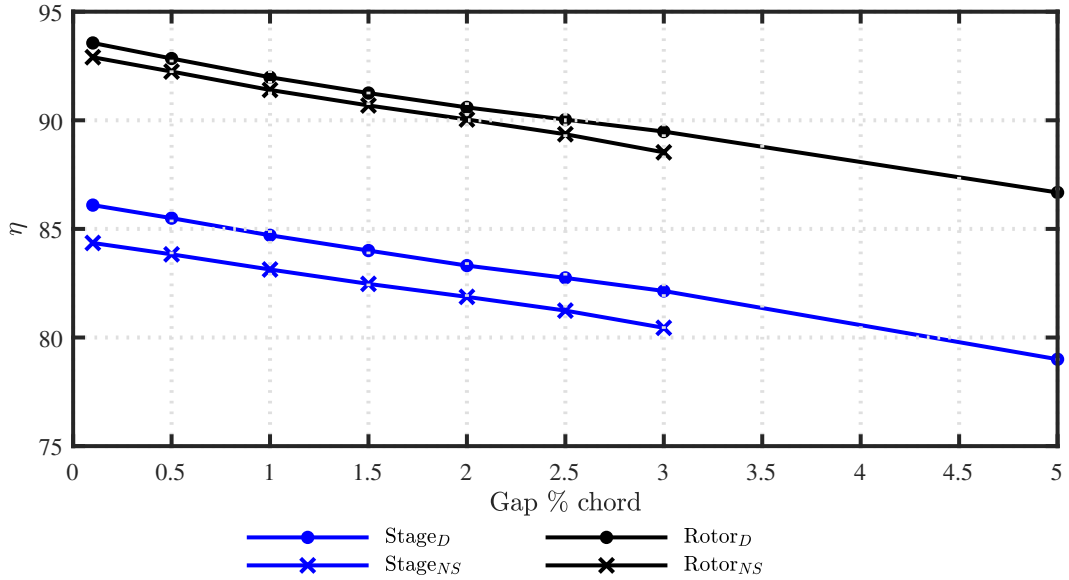

Figure 7.1: Tip clearance effect on rotor and stator efficiency at $Design$ and $Near\ Stall$

The stator loss is decreased at bigger gap sizes. This arises from a decreased hub endwall loss. The increased passage blockage caused by the larger vortex core at bigger tip gaps, shifts more mass flow through the hub region increasing the incidence on stator, as shown in figure 7.3. Thus, the amount of separated flow on the suction side decreases and so does the loss.

Effect on range

$$Range = \frac{\phi_D - \phi_{min}}{\phi_D} \tag{7.1}$$

The effect tip gap size has on the operating range (see equation 7.1) of the stage was also considered, since a higher range leads to different applications where low Re axial compressors can be used. Even though, there is an increase in efficiency and decrease in loss as the size of the rotor tip gap is decreased, the stage flow coefficient range follows a different trend. From figure 7.4, it is clear that there is an optimum tip gap size, for maximum range, of 1% span (1.6% chord). No experiments where conducted as part of this thesis to validate this argument. However, Hewkin Smith et al. [26] found an optimum tip gap of 0.5% chord. Further work can be carried out in the future, to

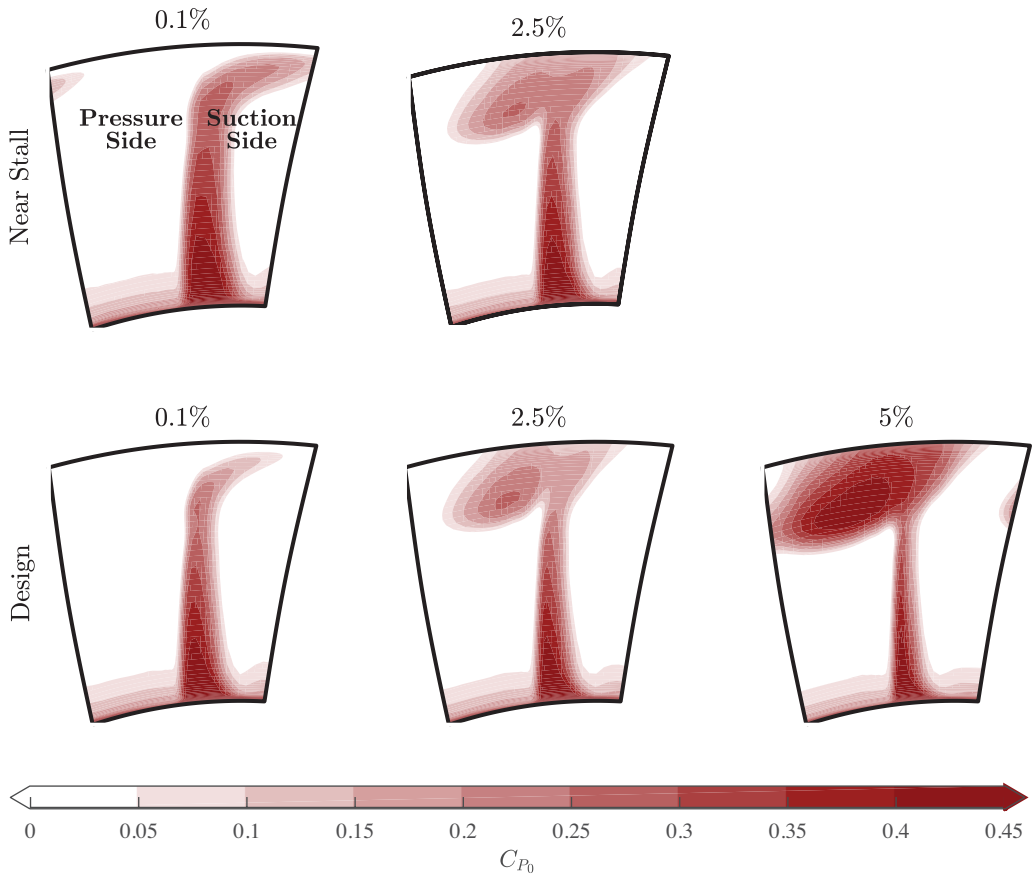

Figure 7.2: Tip clearance effect on rotor pressure loss at $Design$ and $Near\ Stall$

investigate the range performance of rotor with smaller tip gap.

Further, it would benefit low Re rotor flow to validate the findings with an experimental investigation of the effect changing the tip gap size on efficiency and range. This would be supplemented by finding the optimal tip gap decrease before the range stops increasing. Also, with the aid of high pressure transducers embedded in the casing around the tip region, a better understanding can be built around the tip flow development and the stalling mechanism.

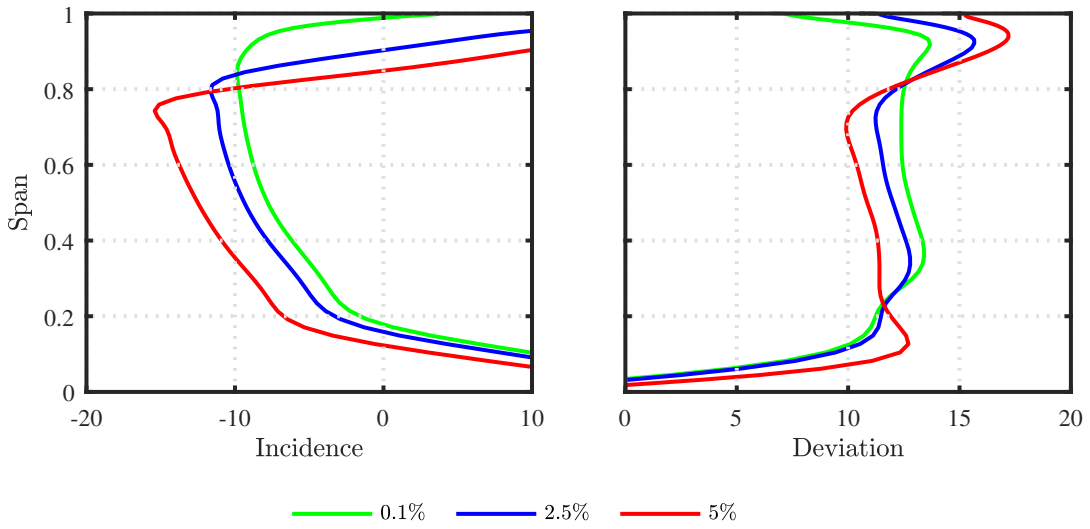

Figure 7.3: Tip clearance effect on stator incidence and deviation at $Design$

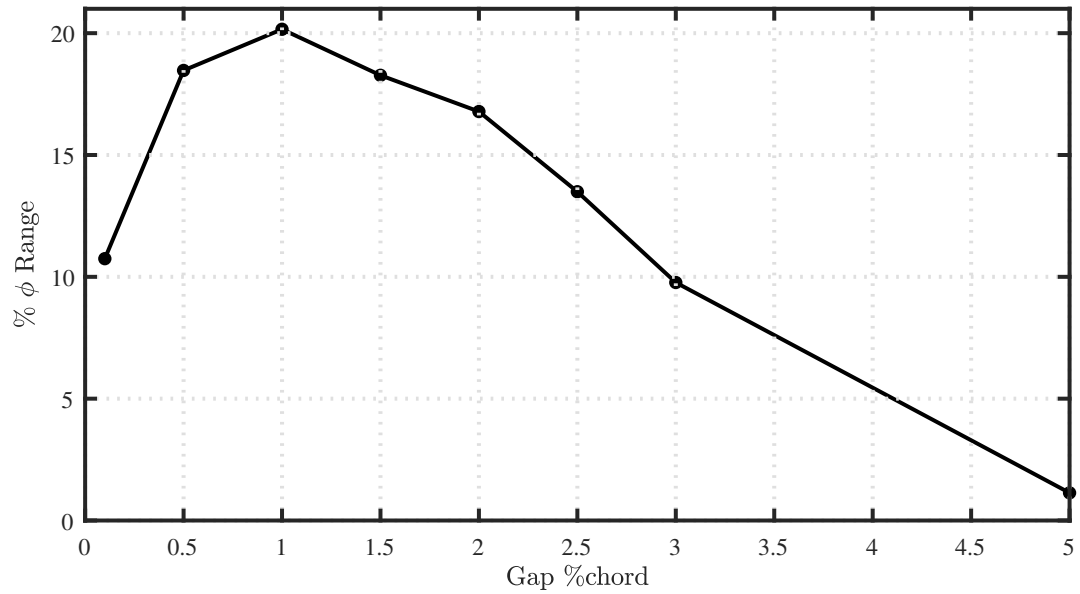

Figure 7.4: Tip clearance effect on ϕ range

Bibliography

[1] Auchoybur, K. and Miller, R. J. (2016). Design of compressor endwall velocity triangles. In *ASME Turbo Expo 2015: Turbine Technical Conference and Exposition*.

[2] Bindon, J. P. (1989). The Measurement and Formation of Tip Clearance Loss. *Journal of Turbomachinery*, 111(3):257–263.

[3] Bolger, J. (1998). *Three Dimensional Design of Compressor Blades*. PhD thesis.

[4] Brandvik, T. and Pullan, G. (2011). An accelerated 3d Navier-Stokes solver for flows in turbomachines. *Journal of Turbomachinery*.

[5] Choi, M., Baek, J. H., Chung, H. T., Oh, S. H., and Ko, H. Y. (2008). Effects of the low Reynolds number on the loss characteristics in an axial compressor. *Proceedings of the Institution of Mechanical Engineers Part a-Journal of Power and Energy*, 222(A2):209–218. WOS:000255045200008.

[6] Corralejo, R. and Harley, P. (2017). Smith diagram for low reynolds number axial fan rotors. In *Proceedings of 12th European Conference on Turbomachinery Fluid dynamics & Thermodynamics*, Stockholm Sweden.

[7] Dantec-Dynamics (2013). Hot-wire Anemometry.

[8] Day, I. J. (2015). Stall, Surge, and 75 Years of Research. *Journal of Turbomachinery*.

[9] Denton, J. D. (1993). Loss mechanisms in turbomachines. *Journal of Turbomachinery*, 115(4):621–656.

[10] Denton, J. D. and Xu, L. (1998). The exploitation of three-dimensional flow in turbomachinery design. *Proceedings of the Institution of Mechanical Engineers, Part C: Journal of Mechanical Engineering Science*, 213(2):125–137.

[11] Dickens, T. and Day, I. (2009). The Design of Highly Loaded Axial Compressors. pages 57–67.

[12] Dixon, S. L. and Hall, C. A. (2014). Fluid mechanics and thermodynamics of turbomachinery. pages 77–79.

[13] Dominy, R. G. and Hodson, H. P. (1992). An Investigation of Factors Influencing the Calibration of 5-Hole Probes for 3-D Flow Measurements.

[14] Dyson Ltd (2013). Centrifugal compressor.

[15] Furukawa, M., Inoue, M., Saiki, K., and Yamada, K. (1999). The role of tip leakage vortex breakdown in compressor rotor aerodynamics. *Journal of Turbomachinery*, 121(3):469–480.

[16] Gallimore, S. J., Bolger, J. J., Cumpsty, N. A., Taylor, M. J., Wright, P. I., and Place, J. M. M. (2002). The Use of Sweep and Dihedral in Multistage Axial Flow Compressor BladingPart I: University Research and Methods Development. *Journal of Turbomachinery*, 124(4):521.

[17] Gaster, M. (1969). *The structure and behaviour of laminar separation bubbles*. Citeseer.

[18] Gbadebo, S. A., Cumpsty, N. A., and Hynes, T. P. (2005). Three-Dimensional Separations in Axial Compressors. *Journal of Turbomachinery*, 127(2):331.

[19] Gbadebo, S. A., Cumpsty, N. A., and Hynes, T. P. (2007). Interaction of Tip Clearance Flow and Three-Dimensional Separations in Axial Compressors. *Journal of Turbomachinery*, 129(4):679.

[20] Gbadebo, S. A., Cumpsty, N. A., and Hynes, T. P. (2008). Control of Three-Dimensional Separations in Axial Compressors by Tailored Boundary Layer Suction. *Journal of Turbomachinery*, 130(1):011004.

[21] Goodhand, M. N. and Miller, R. J. (2011). Compressor Leading Edge Spikes: A New Performance Criterion. *Journal of Turbomachinery*.

[22] Goodhand, M. N. and Miller, R. J. (2012). The Impact of Real Geometries on Three-Dimensional Separations in Compressors. *Journal of Turbomachinery*, 134(2).

[23] Grimshaw, S. and Taylor, J. (2016). Fast Settling Milimetre-Scale Five-Hole Probes. In *ASME Turbo Expo 2016: Turbomachinery Technical Conference and Exposition*, Seoul.

[24] Grimshaw, S. D., Pullan, G., and Hynes, T. P. (2015). Modelling Non-Uniform Bleed in Axial Compressors. page V02BT39A038.

[25] Gunn, E. J. and Hall, C. A. (2014). Aerodynamics of Boundary Layer Ingesting Fans. page V01AT01A024.

[26] Hewkin Smith, M., Pullan, G., Grimshaw, S. D., Greitzer, E. M., and Spakovszky, Z. S. (2017). The role of tip leakage flow in spike-type rotating stall inception.

[27] Hoenen, H. T., Kunte, R., Waniczek, P., and Jeschke, P. (2012). Measuring Failures and Correction Methods for Pneumatic Multi-Hole Probes. pages 721–729.

[28] Lewis, R. I. (1996). Turbomachinery performance analysis. pages xv, 328 p.

[29] Lian, Y. and Shyy, W. (2007). Laminar-Turbulent Transition of a Low Reynolds Number Rigid or Flexible Airfoil. *AIAA Journal*, 45(7):1501–1513.

[30] Maffioli, A., Hall, C., and Melvin, S. (2015). Aerodynamics of Low Reynolds Number Axial Compressor Sections. In *53rd AIAA Aerospace Sciences Meeting*, AIAA SciTech Forum. American Institute of Aeronautics and Astronautics. DOI: 10.2514/6.2015-1934 DOI: 10.2514/6.2015-1934.

[31] Mailach, R., Lehmann, I., and Vogeler, K. (2001). Rotating Instabilities in an Axial Compressor Originating From the Fluctuating Blade Tip Vortex. *Journal of Turbomachinery*, 123(3):453.

[32] NUMECA (2013). IGG, Autogrid5.

[33] Pullan, G., Young, A. M., Day, I. J., Greitzer, E. M., and Spakovszky, Z. S. (2015). Origins and Structure of Spike-Type Rotating Stall. *Journal of Turbomachinery*, 137(5):051007–051007–11.

[34] Ramakrishna, P. V. and Govardhan, M. (2009). Study of Sweep and Induced Dihedral Effects in Subsonic Axial Flow Compressor PassagesPart I: Design ConsiderationsChanges in Incidence, Deflection, and Streamline Curvature. *International Journal of Rotating Machinery*, 2009:1–11.

[35] Reutter, O., Hemmert-Pottmann, S., Hergt, A., and Nicke, E. (2014). Endwall Contouring And Fillet Design For Reducing Losses And Homogenizing The Outflow Of A Compressor Cascade. *Proceedings of ASME Turbo Expo 2014*.

[36] Rhoden, H. G. (1952). Effects of Reynolds Number on the flow of air through a cascade of compressor blades. *ARC, R&M*.

[37] Roberts, W. B. (1979). Axial Compressor Blade Optimization in the Low Reynolds Number Regime. *AIAA Journal*, 17(12):1361–1367.

[38] Roberts, W. B. (1980). Calculation of Laminar Separation Bubbles and Their Effect on Airfoil Performance. *AIAA Journal*, 18(1):25–31.

[39] Sasaki, T. and Breugelmans, F. (1998). Comparison of sweep and dihedral effects on compressor cascade performance. *Journal of Turbomachinery*, 120(3):454–463.

[40] Schlichting, H. (1960). *Boundary Layer Theory*. McGraw-Hill book Company.

[41] Shyy, W., Lian, Y., Tang, J., Viieru, D., and Liu, H. (2008). *Aerodynamics of low Reynolds number flyers*. Cambridge University Press New York.

[42] Smith, L. H., J. (1966). Wake Dispersion in Turbomachines. *Journal of Basic Engineering*, 88(3):688–690.

[43] Spalart, P. R. and Allmaras, S. R. (1994). A One - Equation Turbulence Model for Aerodynamic Flows. No. 1:pp. 5–21.

[44] Storer, J. A. and Cumpsty, N. A. (1991). Tip Leakage Flow in Axial Compressors. *Journal of Turbomachinery*, 113(2):252–259.

[45] Taghavi-Zenou, R., Abbasi, S., and Eslami, S. (2014). Stall Inception and Development Process Due to Tip Leakage Flow in Axial Compressor Rotor Blades Row. *Journal of Mechanics*, 30(03):307–313.

[46] Tani, I. (1964). Low-speed flows involving bubble separations. *Progress in Aerospace Sciences*, 5:70–103.

[47] Taylor, J. V. and Miller, R. J. (2015). Competing 3d Mechanisms in Compressor Flows. In *ASME Turbo Expo 2015: Turbine Technical Conference and Exposition*.

[48] To, H. O. and Miller, R. J. (2015). The Effect of Aspect Ratio on Compressor Performance. In *ASME Turbo Expo 2015: Turbine Technical Conference and Exposition*.

[49] Van Zante, D. E., Adamczyk, J. J., Strazisar, A. J., and Okiishi, T. H. (2002). Wake Recovery Performance Benefit in a High-Speed Axial Compressor. *Journal of Turbomachinery*, 124(2):275.

[50] Varpe, M. K. and Pradeep, A. M. (2014). Non-Axisymmetric Endwall Contouring In A Compressor Cascade With Tip Gap. *Proceedings of ASME Turbo Expo 2014*.

[51] Vinnemeier, F., Simon, L., and Koschel, W. (1990). Correction method for the head geometry influence of a five-hole pressure probe on the measurement results, Korrek- tur des Kopfgeometrieeinflusses einer Fnfloch- Drucksonde auf die Messergebnisse. pages 297–303. Oldenbourg Verlag.

[52] Weinberg, M. and Wyzykowski, J. (2001). Powering unmanned aircraft. *Aerospace engineering*, 21:p. 23–26.

[53] Xu, K. (2001). A gas-kinetic BGK scheme for the NavierStokes equations and its connection with artificial dissipation and Godunov method. *Journal of Computational Physics*, 171(1):289–335.

[54] Yu, X., Zhang, Z., and Liu, B. (2013). The evolution of the flow topologies of {3D} separations in the stator passage of an axial compressor stage. *Experimental Thermal and Fluid Science*, 44:301–311.

[55] Zhang, Z., Yu, X., and Liu, B. (2012). Characteristics of the tip leakage vortex in a low-speed axial compressor with different rotor tip gaps. In *Proceeding of the ASME TURBO EXPO*, pages 11–15.

Appendix A

Simplified factor of safety calculation

$$
\begin{aligned}
\text{Root cross sectional area } (A) &= 1.34 \times 10^{-5}\text{m} \\
\text{Rotor blade mass } (m) &= 7.5 \times 10^{-4}\text{kg} \\
\text{Rotor blade centroid radius } (r_{centroid}) &= 0.0543\text{m} \\
\text{Rotor maximum rotational } \textit{speed } (\omega) &= 24000rpm \times \frac{2\pi}{60} \\
\omega &= 2.51 \times 10^{3}\text{rad}\,\text{s}^{-1} \\
\text{Blade centroid centrifugal force } (F) &= mr_{centroid}\omega^2 \\
F &= 257\text{N} \\
\\
\text{Stress } (\frac{F}{A}) &= \frac{257\text{N}}{1.34 \times 10^{7}\text{Pa}} = 1.9 \times 10^{7}\text{Pa} \\
\\
\text{Factor of safety } (\frac{Yield\ strength}{Stress}) &= \frac{5.05 \times 10^{8}\text{Pa}}{1.9 \times 10^{7}\text{Pa}} = 26 \\
\\
\text{Factor of safety} &= 26 \qquad \text{(A.1)}
\end{aligned}
$$

Appendix B

Loss breakdown calculation

The loss breakdown for the rotor and stator was calculated using equations 3.12 and 3.13 as derived in Dixon and Hall [12]. The stagnation pressure loss was calculated separately for each of the three regions for both the rotor and stator. Then equations B.1 and B.2 were used along with the mass flow weight of each region to calculate the loss associated with each region. The Y_p for each section of the blade rows was calculated using the inlet and exit mass averaged stagnation pressures. The mass average was carried over the equivalent mass flow section.

$$\eta_{tt} \cong 1 - \frac{T_{03}\Delta s_{stage}}{h_{03} - h_{01}}$$

$$T\Delta s_{rotor} \cong \frac{\Delta p_{0,rotor}}{\rho} = \frac{1}{2} w_1^2 Y_{p,rotor}$$

$$T\Delta s_{stator} \cong \frac{\Delta p_{0,stator}}{\rho} = \frac{1}{2} c_2^2 Y_{p,stator}$$

$$\eta_{tt} \cong 1 - \frac{0.5(w_1^2 Y_{p,rotor} + c_2^2 Y_{p,stator})}{h_{03} - h_{01}}$$

$$h_{03} - h_{01} \cong [\Delta(V_t U)]_{\text{rotor}}$$

$$\text{Rotor loss}_{\text{ casing, mid, hub}} \cong [w \times \frac{0.5(W_1^2 Y_{p,rotor})}{V_{t2} U_2}]_{\text{casing, mid, hub}} \quad \text{(B.1)}$$

$$\text{Stator loss}_{\text{ casing, mid, hub}} \cong [w \times \frac{0.5(V_2^2 Y_{p,stator})}{V_{t2} U_2}]_{\text{casing, mid, hub}} \quad \text{(B.2)}$$

$$w_{\text{hub}} = 0.25 \quad w_{\text{mid}} = 0.5 \quad w_{\text{casing}} = 0.25$$